Doctoral Thesis

Field: Information and Communication Sciences and Technologies
Specialization: Signal and Image Processing

submitted to the *Doctoral School of Science, Technology and Health (ED 585)*

of the Université du Littoral Côte d'Opale

by

Ali CHAMSEDDINE

in order to obtain the degree of Doctor of the Université du Littoral Côte d'Opale

Change Point Detection in the Phase of a Signal: Application to Remote Sensing by GNSS-Reflectometry

Defended on January 29, 2026, following the reviewers' reports and the approval of the examination jury:

President:	**Prof. Oussama BAZZI, Lebanese University**
Reviewer:	**Prof. Alexandre BAUSSARD, Université de Technologie de Troyes**
Reviewer:	**Prof. Karim ELMOKHTARI, Toronto Metropolitan University**
Examiner:	**Dr. Hamza ISSA, NovAtel Inc**
Advisor:	**Prof. Serge REBOUL, ULCO**
Co-advisor:	**Prof. Ghaleb FAOUR, CNRS-Lebanon**
Co-advisor:	**Prof. Georges STIENNE, ULCO**

LISIC Laboratoire d'Informatique Signal & Image de la Côte d'Opale

CNRS National Council for Scientific Research

Thèse de Doctorat

Mention Sciences et Technologies de l'Information et de la Communication
Spécialité Traitement du Signal et des Images

présentée à *l'École Doctorale en Sciences Technologie et Santé (ED 585)*

de l'Université du Littoral Côte d'Opale

par

Ali CHAMSEDDINE

pour obtenir le grade de Docteur de l'Université du Littoral Côte d'Opale

Detection de rupture dans la phase d'un signal: application à la télédétection par reflectometrie GNSS

Soutenue le 29 janvier 2026, après prise en compte des rapports des rapporteurs et approbation du jury d'examen :

President:	**Prof. Oussama BAZZI, Lebanese University**
Reviewer:	**Prof. Alexandre BAUSSARD, Université de Technologie de Troyes**
Reviewer:	**Prof. Karim ELMOKHTARI, Toronto Metropolitan University**
Examiner:	**Dr. Hamza ISSA, NovAtel Inc**
Advisor:	**Prof. Serge REBOUL, ULCO**
Co-advisor:	**Prof. Ghaleb FAOUR, CNRS-Lebanon**
Co-advisor:	**Prof. Georges STIENNE, ULCO**

Acknowledgements

First and foremost, I cannot begin without expressing my deepest gratitude to the person who guided me throughout my PhD journey, the one who never said "it's difficult," even when things seemed impossible. A true expert in almost everything, he made research feel like a fascinating world one can't help but love. He is the person who taught me what science truly means, and why we pursue it with passion and integrity. His love for mathematics recalls that of the great French scientists, working with him often felt like traveling back to the 16th century, solving timeless mathematical problems with elegance and depth. Thank you, Professor Serge Reboul. Anyone who knows him will understand exactly what I mean. Secondly, I would like to express my heartfelt thanks to Professor Georges Stienne, whose spirit and intellect mirror those of Serge. Georges has an extraordinary ability to uncover problems hidden in the dark and to bring forth clear, brilliant solutions from that very darkness. He taught me to see the ideas behind mathematical equations, not just their symbols, and together we spent countless hours at the whiteboard, immersed in mathematics, signals, and the art of thinking correctly. Thank you so much, Georges, for your patience, wisdom, and guidance. My sincere thanks also go to all my friends and colleagues at the LISIC Laboratory and ULCO Calais. Remembering our meetings, discussions about the future, and shared challenges always fills me with joy and gratitude. Thank you all for making this chapter of my life so meaningful. I would like to express my particular gratitude to Madame Carole Lagatie and Madame Gaëlle Compiègne for their invaluable help and continuous support throughout all the administrative aspects of my PhD. And a special thanks for my thesis co-supervisor at CNRS-L Prof Ghaleb Faour and for all CNRS-L organization, this institue is giving quality research across Lebanon and the world. A very special thanks goes to my parents, the two people to whom I owe everything. Their unwavering support has been my anchor. Thank you, my mother. Thank you, my father. I owe every achievement to you. To my beloved family, my brothers and sisters, thank you for being beside me in every step, holding my hand toward success. And to all my dear friends, in Lebanon, in France, in the UK and in everyplace, you make my

life far more valuable than I sometimes realize, thank you. To my beautiful daughter, Fatima: Your birth opened my eyes to a new and more beautiful life. Since the day you came into this world, my goals have felt closer and my purpose clearer. Thank you, my little one, you have been, and will always remain, one of the most beautiful blessings in my life. Thank you, Fatima.

To my beloved wife, my lifelong companion: Thank you, though no words of gratitude could ever capture the depth of what you deserve. Every "thank you" is but a small star in the vast sky of your sacrifices, your patience, your unwavering support, and the light of your face that has illuminated my path and will continue to do so forever. Thank you a lot, my love.

Ali Chamseddine

Contents

Acknowledgements i

List of Figures vii

List of Tables xi

List of Abbreviations xiii

List of Symbols xv

General Introduction 1

1 Utilization of Carrier Phase in GNSS-Reflectometry Signal Processing 5

1.1 Introduction 5
1.2 Fundamental Principles of GNSS-Reflectometry (GNSS-R) . . 6
1.3 Comparison of Carrier Phase Utility vs GNSS Signal Amplitude and Delay 8
1.3.1 Overview 8
1.3.2 Comparative Analysis of GNSS-R Observables 8
1.3.3 Trade-Offs and Use Case Recommendations 9
1.4 Review of Existing Carrier Phase-Based GNSS-R Techniques . 10
1.4.1 Example of Observations with Google Earth and Signal Variations 13
1.5 GNSS Signal Processing 15
1.5.1 GPS L5 Signal Acquisition and Analysis 16
1.5.2 GNSS-R Signal Processing 19
1.6 GNSS-R Observables and Measurement Models 22
1.6.1 Reflected GNSS signal phase measurement 22
1.6.2 Reflected GNSS signal phase noise distribution 23
1.6.3 Assisted GNSS-R Signal Tracking 25
1.7 Discussion 26

2 Change Point Detection: Literature Review **29**
2.1 Introduction . . . 29
2.2 Motivation and Relevance to GNSS-R Carrier-Phase Analysis . . . 30
2.2.1 Change in Distributional Parameters . . . 30
2.2.2 Change in the Underlying Model Due to Physical Regimes 30
2.3 Mathematical Formulation of Change Point Detection . . . 31
2.4 Challenges in Change Point Detection for GNSS-R Data . . . 32
2.5 Multiple Change Point Detection . . . 33
2.6 Single Change Point Detection . . . 39
2.7 Discussion . . . 41

3 A circular statistical test for change point detection **43**
3.1 Introduction . . . 43
3.2 The statistical tests in the circular domain . . . 44
3.2.1 Kolmogorov-Smirnov Test for Linear Data . . . 45
3.2.2 Kuiper's Test for Circular Data . . . 45
3.2.3 Watson Test for Circular Data . . . 46
3.2.4 Rao's Spacing Test for Circular Data . . . 46
3.2.5 Rayleigh Test for Circular Data . . . 47
3.2.6 Experimental Comparison of Linear vs Circular Uniformity Tests . . . 47
3.2.7 Discussion . . . 49
3.3 Phase Coherence Detection using Test for uniformity . . . 49
3.3.1 Phase Coherence Metrics . . . 51
3.3.2 Change Detection Method . . . 52
3.4 Experimentation . . . 54
3.4.1 Synthetic Experimentation . . . 54
3.4.2 Real Data Application . . . 56
3.5 Discussion . . . 61

4 Bayesian Offline Change Detection Applied to GNSS-Reflectometry Phase Data **63**
4.1 Introduction . . . 63
4.2 Method of reference . . . 66
4.3 Bayesian estimate . . . 67
4.3.1 Linear circular models . . . 67
4.3.2 Bayesian framework . . . 68
4.3.3 Bayesian change point estimate . . . 69

4.4 GNSS-R application 71
4.4.1 GNSS-R Radar observation 71
4.4.2 GNSS-R Phase model 73
4.5 Experimentation 74
4.5.1 Analysis of Synthetic Phase Data with a Single Change Point 75
4.5.2 Assessment on synthetic data with Multiple Change Points 76
4.5.3 Real GNSS-R measurement 78
4.6 Discussion 86

General Conclusion **89**

Bibliography **91**

Résumé Étendu de la Thèse **101**
1 Utilisation de la phase porteuse dans le traitement du signal GNSS-Reflectometry 101
1.1 Principes Fondamentaux de la GNSS-Reflectométrie (GNSS-R) 101
1.2 Intérêt de la Phase Porteuse en GNSS-R 102
1.3 Mesure de la Phase Réfléchie et Modélisation 103
1.4 Distribution du Bruit de Phase : Loi de Von Mises . . . 104
1.5 Campagne Aéroportée GNSS-R 104
2 Détection de points de changement : Revue de la littérature . 104
2.1 Introduction à la Détection de Points de Changement . 104
2.2 Taxonomie des Méthodes de CPD 105
2.3 Composantes Méthodologiques des Deux Catégories . 105
2.4 Intérêt de la Taxonomie 106
3 Test Statistique Circulaire pour la Détection de Points de Changement 106
3.1 Tests Statistiques dans le Domaine Circulaire 106
3.2 Application sur Données Réelles 106
3.3 Conclusion et Perspectives 107
4 Détection Bayésienne Hors-Ligne des Changements 108
4.1 Modélisation de la Phase 108
4.2 Principe de la Méthode BCPD 108
4.3 Estimation des Paramètres 109
4.4 Résultats sur Données Synthétiques 109

4.5 Résultats sur Données Réelles GNSS-R 109
4.6 Conclusion 110

Abstract **111**

Résumé **113**

List of Figures

1.1 GNSS-R phase coherence concept. 6
1.2 Geometry of a GNSS reflection 7
1.3 Google Earth visualization of the reflected signal trajectory of GPS PRN 5 between seconds 1770 and 1793 of the flight. . . . 14
1.4 Reflected GNSS signal from GPS PRN 5 showing the normalized amplitude (top), phase (middle), and a zoomed-in phase segment (bottom) corresponding to the first 189 samples of the 1770–1793 s interval. 15
1.5 Correlation amplitude versus code delay at the estimated Doppler frequency on the top, and correlation amplitude as a function of Doppler frequency at the detected code delay at the bottom of PRN 10 18
1.6 Correlation amplitude versus code delay at the estimated Doppler frequency on the top, and correlation amplitude as a function of Doppler frequency at the detected code delay at the bottom of PRN 14 19
1.7 Closed-Loop Tracking for reflected signal 20
1.8 Comparison between open-loop and closed-loop tracking phases for the direct GNSS L1 signal from GPS PRN-5. 21
1.9 Open-Loop Tracking for reflected signal 21
1.10 Probability density functions (PDFs) of the Von Mises distribution for different concentration parameters κ. 24
1.11 Reflected GNSS signal phase computing block diagram 26
1.12 Assisted tracking phase of reflected signal obtained from GPS satellite PRN-5 over the interval 1717.06–1722.6 seconds of the flight. 27

2.1 Structured taxonomy of Change Point Detection based on methodological aspects 33
2.2 Detailed taxonomy of Multiple Change Point Detection methods 35
2.3 Detailed taxonomy of Single Change Point Detection methods 39

3.1 Circular distribution of the 4 segments. Each segment is plotted with a distinct color. 47
3.2 Circular distribution of the four segments of synthetic data. Each segment is plotted separately, illustrating the progression from strict uniformity to strong non-uniformity. 48
3.3 Simulated phase noise; Circular Length (CL), Circular Kurtosis (CK) and Rayleigh Test (RT) outputs for 10 changes in coherence (black doted lines) ($dt = 1$ms, $N = 20$). 54
3.4 Cost functions $d(RT)$ and $d(CL, CK)$ for 10 changes in coherence (black doted lines) in phase noise measurements affected by residual oscillations ($dt = 1$ms, $N = 20$, $M = 100$). 55
3.5 Reflections traces of three GPS satellites (PRN 5, PRN 7, and PRN 30), corresponding respectively to path in (blue), path in (green), and path in (red). The tracks are visualized over the region of Northern France, in Calais. Each trajectory represents the spatial evolution of the specular reflection points detected during the airborne GNSS-R campaign. 57
3.6 The gyrocopter used during the flight was equipped with embedded sensors [71]. 58
3.7 Coherence levels as traces of the GPS satellites of PRN 5, 7 and 30 along a section of the flight trajectory (50.8763°, 1.9548°). . . 59
3.8 Reflected-signal analysis for GPS satellites PRN 7, PRN 5, and PRN 30. The upper panels show the cost function. While the lower panels show the corresponding Rayleigh test statistic (RT) used to quantify phase coherence over the flight time, where the blue points represent the RT values computed from the reflected carrier phase, and the red shows the means of RT 60
3.9 Coherence levels as traces of the GPS satellites of PRN 5, 7 and 30 along the complete flight trajectory. 61

4.1 Flow chart for the estimation of the contrast function 71
4.2 Multi reflections from rough sea surface 72
4.3 Equi-Doppler Multi reflections concept in GNSS-R 73
4.4 Phase sequence illustrating the detected change point at 6 s. The first segment (0–6 s) corresponds to the non-coherent region, while the second segment (6–12 s) represents the coherent region. A vertical dashed line marks the detected change location. 75

4.5 Spectrum analysis of the excess Doppler in coherent and non-coherent segments of the first realization of the synthetic data, along with phase estimation for both segments. 77
4.6 Comparison of change detection and probability of good detection for synthetic data: Evaluating the performance of the detection methods. 79
4.7 10 seconds of phase data from the reflected GNSS signal of GPS satellite PRN 5, showing a rough land surface (red) in the first segment and a smooth lake surface (yellow) in the second segment, with the detected change accurately identified. . . . 80
4.8 Computed Contrast Function corresponding to the reflected carrier-phase signal shown in Figure 4.7. The minimum value of the Contrast Function, indicated by a small red circle, marks the detected change point. 81
4.9 15 seconds of phase data from the reflected GNSS signal of GPS satellite PRN 5, showing a smooth lake surface (yellow) in the first segment and a rough land surface (red) in the second segment, with the detected change accurately identified. . . . 83
4.10 7 seconds of phase data from the reflected GNSS signal of GPS satellite PRN 5, showing a smooth lake surface (yellow) in the first segment and a rough land surface (red) in the second segment, with the detected change accurately identified. 84
4.11 7.5 seconds of phase data from the reflected GNSS signal of GPS satellite PRN 5, showing a rough surface(red) in the first segment and a smooth surface represented by flat stadium (yellow) in the second segment, with the detected change accurately identified. 86
R.1 Concept de cohérence de phase en GNSS-R. 102
R.2 Schéma de traitement de la phase réfléchie GNSS 103
R.3 Taxonomie structurée de la détection de points de changement selon les aspects méthodologiques 105
R.4 Traces des satellites GPS PRN 5, 7 et 30 le long de la trajectoire de vol et niveaux de cohérence de phase segmentés par l'approche Rayleigh (50.8763°, 1.9548°). 107
R.5 Résultat de détection des changements sur des données synthétiques. 109
R.6 Données réelles GNSS-R : détection d'un changement entre une surface lisse (lac) et une surface rugueuse (terre). 110

List of Tables

1.1 Comparison of GNSS-R Observables 10
1.2 L1 vs L5 properties [23] 16

3.1 KS and Rayleigh test statistics for the four segments of synthetic circular data. 49
3.2 Rate of good detection and RMSE on localization for changes in coherence. 55
3.3 Summary of flight parameters during the GNSS-R measurement campaign [71] 58

4.1 Parameter estimates for Figure 4.4, second segment (coherent from t = 6s to t = 12s). 76
4.2 Parameter estimates for Figure 4.4, first segment (non-coherent from t = 0s to t = 6s). 76
4.3 Parameter estimates for Figure 4.6(a), first and last segments (coherent). 78
4.4 Parameter estimates for Figure 4.6(a), second segment (non-coherent). 78
4.5 Parameter estimates for Figure 4.7, first segment (non-coherent). 81
4.6 Parameter estimates for Figure 4.7, second segment (coherent). 81
4.7 Parameter estimates for Figure 4.9, first segment (coherent). . 82
4.8 Parameter estimates for Figure 4.9, second segment (non-coherent). 83
4.9 Parameter estimates for Figure 4.10, first segment (coherent). . 84
4.10 Parameter estimates for Figure 4.10, second segment (non-coherent). 84
4.11 Parameter estimates for Figure 4.11, first segment (non-coherent). 86
4.12 Parameter estimates for Figure 4.11, second segment (semi-coherent). 86
R.1 Comparaison des observables GNSS-R 103

List of Abbreviations

GNSS-R	**G**lobal **N**avigation **S**atellite **S**ystems **R**eflectometry
GNSS	**G**lobal **N**avigation **S**atellite **S**ystem
PLL	**P**hase-**L**ocked **L**oop
DLL	**D**elay-**L**ocked **L**oop
FLL	**F**requency-**L**ocked **L**oop
POL	**P**hase **O**pen **L**oop
CA	**C**oarse/**A**cquisition code
ML	**M**aximum **L**ikelihood
CRLB	**C**ramer-**R**ao **L**ower **B**ound
SSH	**S**ea **S**urface **H**eight
RHCP	**R**ight-**H**and **C**ircular **P**olarization
LHCP	**L**eft-**H**and **C**ircular **P**olarization
PDF	**P**robability **D**ensity **F**unction
MCD	**M**inimum **C**ovariance **D**eterminant
CPD	**C**hange **P**oint **D**etection
MCPD	**M**ultiple **C**hange **P**oint **D**etection
SCPD	**S**ingle **C**hange **P**oint **D**etection
CUSUM	**C**umulative **S**um
GLR	**G**eneralized **L**ikelihood **R**atio
BIC	**B**ayesian **I**nformation **C**riterion
mBIC	**m**odified **B**ayesian **I**nformation **C**riterion
ED	**E**uclidean **D**istance
PCD	**P**earson **C**orrelation **D**istance
KCP	**K**ernel **C**hange-**P**oint
RKHS	**R**eproducing **K**ernel **H**ilbert **S**pace
PELT	**P**runed **E**xact **L**inear **T**ime
MCMC	**M**arkov **C**hain **M**onte **C**arlo
DFPS	**D**ouble-**W**indow **F**lexible **P**ace **S**earch
MAD	**M**ultivariate **A**lteration **D**etection
MAF	**M**aximum **A**utocorrelation **F**actor
CD	**C**hange **D**etection
BCPD	**B**ayesian **C**hange **P**oint **D**etection
SVM	**S**upport **V**ector **M**achine
SNR	**S**ignal to **N**oise **R**atio
KS	**K**olmogorov-**S**mirnov
CL	**C**ircular **L**ength
CK	**C**ircular **K**urtosis
RT	**R**ayleigh **T**est
EDF	**E**mpirical **D**istribution **F**unction

CDF	**C**umulative **D**istribution **F**unction
RMSE	**R**oot **M**ean **S**quare **E**rror
IF	**I**ntermediate **F**requency
LEO	**L**ow **E**arth **O**rbit
CDMA	**C**ode **D**ivision **M**ultiple **A**ccess
MLE	**M**aximum **L**ikelihood **E**stimate
AR	**A**uto**R**egressive
ARMA	**A**uto**R**egressive **M**oving **A**verage

List of Symbols

A_u	Amplitude of the u-th reflected component estimated using excess Doppler
a_u	Weight / amplitude of the u-th reflected component in the circular model
$a_{u,k}$	Amplitude of the u-th reflected component in segment k
$CA(\cdot)$	CDMA spreading code of GNSS signal
T_c	GNSS code period / coherent integration interval
dt	Sampling period
f_c	Carrier frequency of GNSS signal
$\hat{f}_c$	Estimated carrier frequency
f_d	Excess Doppler frequency
$f_{d,i}$	Excess Doppler frequency of the i-th reflection
$f_{d,u}$	Excess Doppler frequency of the u-th reflection
ω	Angular Doppler/frequency parameter, $\omega = 2\pi f_d$
ω_i	Angular-frequency parameter of the i-th reflection
ω_u	Angular-frequency parameter of the u-th reflection
$\omega_{u,k}$	Angular-frequency parameter of the u-th reflection in segment k
$\hat{\omega}$	Estimated angular-frequency parameter reported in tables
$\hat{\omega}_{u,k}$	Estimated angular-frequency parameter of the u-th reflection in segment k
$\phi(t)$	Carrier phase of received GNSS signal
$\hat{\phi}$	Estimated carrier phase
ϕ_i	Observed carrier phase at sample i
$\hat{\phi}_i$	Smoothed carrier phase at sample i
$\phi_i(t)$	Phase of the i-th reflection as a function of time
ϕ_i^{trend}	Carrier-phase trend caused by frequency error
α	Excess phase / intercept parameter
α_u	Excess phase of the u-th reflected component
$\alpha_{u,k}$	Excess phase of the u-th reflected component in segment k
$\hat{\alpha}$	Estimated excess phase parameter
$\hat{\alpha}_{u,k}$	Estimated excess phase of the u-th reflected component in segment k
$s(t)$	Received GNSS signal
$\hat{s}(t)$	Locally generated GNSS signal replica
$s_r(t)$	Reflected GNSS signal
I_i	In-phase component at sample i
Q_i	Quadrature component at sample i
$\tilde{I}_i$	Noiseless in-phase component
$\tilde{Q}_i$	Noiseless quadrature component
$\eta(t)$	Gaussian noise in reflected GNSS signal
η_I	Gaussian noise in the in-phase channel after correlation
η_Q	Gaussian noise in the quadrature channel after correlation
$\epsilon_I(i)$	Gaussian noise affecting in-phase observation

$\epsilon_Q(i)$	Gaussian noise affecting quadrature observation
ξ_i	Centered circular noise (Von Mises distributed)
ε_i	Carrier-phase noise after detrending, $\varepsilon_i = \phi_i - \hat{\phi}_i$
N	Number of samples in a window
M	Window size used for cost computation
U	Number of reflections
U_k	Number of reflections in segment k
$\hat{U}_k$	Estimated number of reflections in segment k
CL	Circular Length
CK	Circular Kurtosis
RT	Rayleigh Test statistic
R	Mean resultant length
V_n	Kuiper test statistic
V	Modified Kuiper test statistic
U_2	Watson test statistic
U_R	Rao's Spacing test statistic
D_n	Kolmogorov–Smirnov test statistic
κ	Concentration parameter of the Von Mises distribution
$\hat{\kappa}$	Estimated concentration parameter
$\hat{\kappa}_k$	Estimated concentration parameter in segment k
$\Gamma_k(f)$	Spectrum of the reflected signal in segment k
Ψ	Spectral noise term
$\delta(\cdot)$	Dirac delta function
$\underline{y}$	Sequence of observed phase data
$\underline{r}$	Configuration of change points
$\mathcal{R}$	Random change-point configuration variable
$\underline{\theta}$	Sequence of model parameters
θ_k	Parameter vector of segment k
t_k	Change-point instant of segment k
K	Number of stationary segments
L_k	Length of segment k
$V_y(\cdot)$	Contrast function
$U_y(\cdot)$	Penalized contrast function
$c_\Sigma(\cdot)$	Cost function for mean/variance changes
$d(\cdot)$	Sliding-window discrepancy function
λ	Prior probability of change occurrence
β	Penalization parameter, $\beta = \ln\left(\frac{\lambda}{1-\lambda}\right)$
γ	Shape parameter in Fisher circular regression mapping
ED	Euclidean Distance
T_1^i	Spectrum value of first segment at bin i
T_2^i	Spectrum value of second segment at bin i
n_b	Number of spectral bins

General Introduction

Global Navigation Satellite System Reflectometry (GNSS-R) has emerged as a valuable remote sensing technique that leverages signals of opportunity transmitted by GNSS constellations and reflected off the Earth's surface. Its passive, all weather, and cost-effective nature has enabled applications ranging from ocean surface monitoring to soil moisture estimation and snow depth retrieval. Most conventional GNSS-R systems and methodologies have focused on signal amplitude and delay characteristics, due to their relatively straightforward interpretation and measurement. However, the carrier phase of the reflected signal, despite being more sensitive to small surface changes and offering higher temporal and spatial resolution, remains underutilized in practical GNSS-R applications due to the challenges associated with its coherent processing, ambiguity resolution, and noise sensitivity.

This thesis addresses the underexploited potential of the carrier phase in GNSS-R by developing a robust methodology to analyze, model, and detect changes in the reflected GNSS signal phase. The central motivation lies in the fact that the phase component encodes subtle variations in the propagation path, which are directly influenced by the physical and geometric properties of the reflecting surface. Therefore, tracking phase variations can provide a powerful tool for surface-type differentiation, environmental monitoring, and geophysical inference.

To leverage the phase information effectively, this thesis begins by exploring the fundamental principles of GNSS-R with an emphasis on carrier phase characteristics. A comparative analysis is performed to highlight the trade-offs and complementarities betwen carrier phase and amplitude (SNR). A review of existing carrier phase-based GNSS-R techniques is conducted to situate the work within current research efforts, emphasizing the need for refined statistical tools to process the circular nature of phase data and to detect structural changes over time.

A core contribution of this work lies in the design and application of

change point detection (CPD) methodologies tailored for circular data. Classical CPD methods often assume linear data distributions and are ill-suited for phase observables, which are inherently defined on a modulo 2π domain. Therefore, a specialized circular statistical framework is introduced, with focus on uniformity tests such as the Rayleigh, Watson, Kuiper, and Rao's spacing tests.

In addition, the thesis introduces a novel multiple change point detection method based on Bayesian principles. The proposed offline Bayesian Change-Point Detection (BCPD) method represents a significant advancement in analyzing phase variations of reflected GNSS signals within the GNSS-R framework. Unlike conventional change detection techniques designed for linear data, this approach explicitly addresses the circular nature of carrier phase data by modeling phase noise using the Von Mises distribution, a natural choice for directional statistics. This modeling allows for accurate characterization of phase behavior, which is critical given the inherent periodicity and ambiguity of phase measurements. At the core of the method is the estimation of change points by minimizing a carefully constructed contrast function, which incorporates key spectral parameters linked to excess Doppler shifts. The Bayesian framework enables a principled segmentation of the data into statistically homogeneous intervals, balancing sensitivity and robustness through a penalized likelihood approach. This flexibility allows the method to detect subtle changes in phase coherence that correspond to variations in the reflecting surfce, such as transitions between smooth and rough terrains.

From a methodological standpoint, this thesis presents several original contributions. It bridges the gap between classical change detection techniques and directional statistics by enhancing uniformity tests for more effective phase coherence analysis. Furthermore, it adapts Bayesian change detection methods to operate specifically on phase observables, which are inherently circular. These advancements collectively establish a unified and robust framework for phase-based GNSS-R signal interpretation. Importantly, the proposed methods have been rigorously validated on synthetic datasets to demonstrate controlled performance and, crucially, on real GNSS-R measurements, underscoring their practical applicability and effectiveness

in real-world scenarios. This combination of theoretical innovation and empirical validation significantly extends the analytical toolbox available to researchers in remote sensing and signal processing.

Structurally, the thesis is organized as follows:

- **Chapter 1** introduces the foundations of GNSS-R and emphasizes the carrier phase's unique potential, followed by a technical review of its measurement models and noise characteristics.
- **Chapter 2** presents classical and modern change detection techniques in the literature and designs a classification for these change point detection approaches.
- **Chapter 3** introduces circular statistical tests and adapts them for phase coherence change detection, demonstrating their utility through both synthetic and real datasets.
- **Chapter 4** develops a Bayesian framework for offline multiple change point detection in circular data, and validating its effectiveness on both synthetic data and real GNSS-R measurements.

Ultimately, this thesis aims to demonstrate that the carrier phase of reflected GNSS signals, when analyzed through appropriate statistical frameworks, can become a powerful observable for environmental monitoring and geophysical interpretation. The convergence of GNSS signal processing, directional statistics, and Bayesian inference in this work opens new perspectives for high-resolution, passive remote sensing systems that are both theoretically grounded and practically effective.

Chapter 1

Utilization of Carrier Phase in GNSS-Reflectometry Signal Processing

1.1 Introduction

This chapter introduces the use of carrier-phase measurements as a central observable in GNSS-Reflectometry (GNSS-R) signal processing. GNSS-R is first presented as a bistatic remote sensing technique that exploits reflected GNSS signals to characterize Earth surfaces. Particular emphasis is placed on the physical meaning of the reflected carrier phase, whose short wavelength makes it highly sensitive to small variations in propagation path, surface roughness, and dielectric properties.

The chapter then compares carrier phase with other commonly used GNSS-R observables, mainly amplitude and signal-to-noise ratio, in order to clarify their respective advantages and limitations. A review of existing carrier-phase-based GNSS-R techniques is provided to position this work within the current scientific literature, especially in relation to altimetry, soil moisture monitoring, and surface characterization. To connect the theoretical concepts with real observations, examples from airborne GNSS-R data are presented using both geographical trajectories and corresponding signal variations.

Finally, the chapter describes the main GNSS signal processing strategies required to extract reliable phase observables from direct and reflected signals. Closed-loop, open-loop, and assisted tracking architectures are discussed, followed by the mathematical formulation of the reflected phase measurement model. Since the reflected phase is angular by nature, its noise is modeled using the Von Mises distribution, providing the circular statistical foundation required for the change detection methods developed in the following chapters.

1.2 Fundamental Principles of GNSS-Reflectometry (GNSS-R)

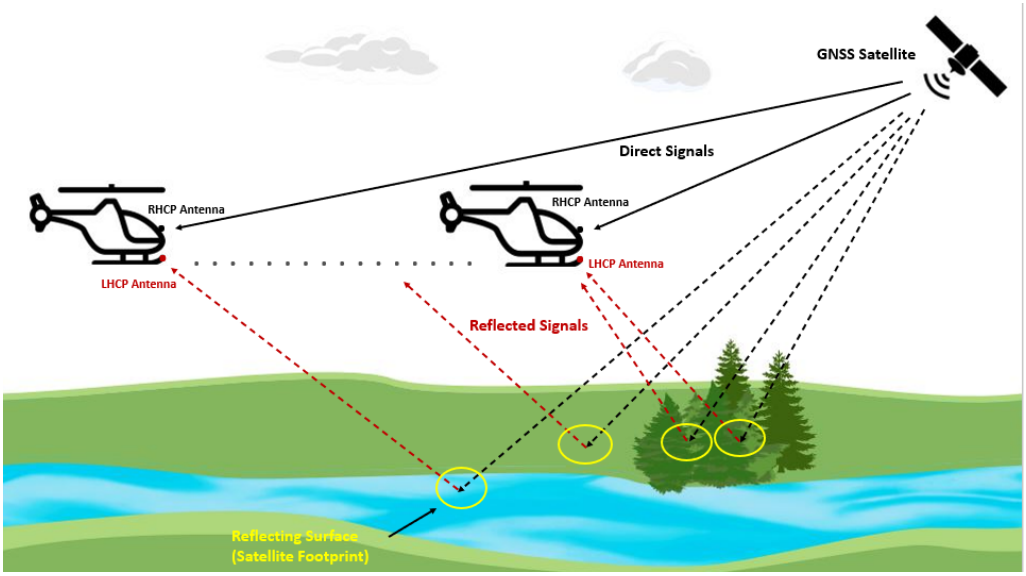

FIGURE 1.1: GNSS-R phase coherence concept.

GNSS-Reflectometry operates as a bistatic radar system, where the transmitter and receiver are spatially separated by a distance comparable to that between the receiver and the target surface [1], as illustrated in Figure 1.1, with its geometry defined in Figure 1.2. It uses the Global Navigation Satellites Systems (GNSS) signals as signals of opportunity. It was proposed in 1993 by Martín-Neira [2] for ocean altimetry measurements purpose and has been studied since then for a broad range of other applications, including sea state estimation and wind speed retrievals, soil moisture detection, surface topography, cryosphere sensing and ionospheric electron content determination. The key strengths of GNSS-R as a radar technique are the availability of a large number of emitters in space (GPS, GLONASS, Galileo and BeiDou systems all have global coverage of the Earth surface), the flexibility in the position of the receiver (spaceborne, airborne or fixed, ground-based antennas) and its ability to remotely sense multiple areas simultaneously.

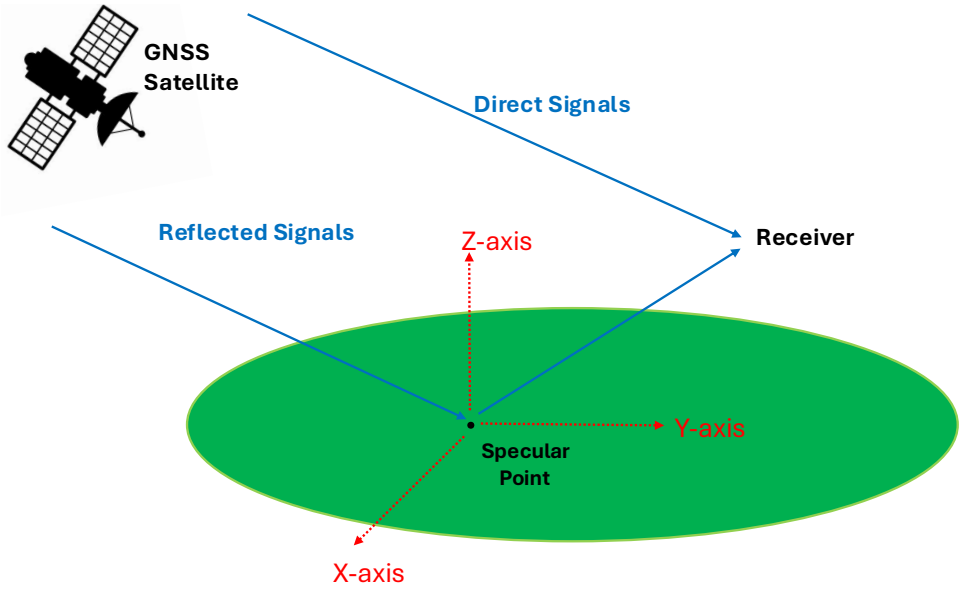

FIGURE 1.2: Geometry of a GNSS reflection

At the receiver location, the electromagnetic field is composed of contributions from several GNSS satellites. An individual GNSS transmitters can be distinguished and isolated thanks to the unique modulations applied to each signal. The received contributions include both direct signals that travel from the satellite to the receiver through the atmosphere, and reflected signals that first propagate down to the Earth's surface, scatter, and then reach the receiver. These different signal paths are referred to interchangeably as "rays" or "radio-links". In principle, these two types of contributions can be separated using two different antennas: one oriented toward the satellites to capture direct signals, and another directed at the Earth's surface to collect reflected signals.

Advancements in GNSS-Reflectometry have been propelled by the growing scientific and operational interest in leveraging reflected GNSS signals for Earth observation. This surge in attention has led to the development of dedicated instrumentation and a substantial number of flight campaigns. Between the late 1990s and October 2013, more than 270 airborne experiments were carried out using over 20 distinct GNSS-R receiver configurations. These missions spanned a wide range of geographical environments, successfully capturing reflected signals from surfaces such as open oceans, agricultural lands, bare soils, inland water bodies, polar ice, glaciers, and snow-covered terrains across mid- and high-latitude regions. A subset of

these experimental datasets has been made publicly accessible for scientific use through dedicated repositories [3], and detailed descriptions of these campaigns are available in prior documentation [4]. The extension of GNSS-R capabilities to spaceborne platforms has also been validated. A pioneering demonstration came from the SIR-C mission aboard the Space Shuttle, which first detected GNSS signal reflections from space [5]. Subsequently, satellites from the UK Disaster Monitoring Constellation (UK-DMC) equipped with moderate-gain GNSS-R receivers (gain $\approx$ 11.8 dBi) captured reflections from diverse surface types, including ocean, land, and ice, from altitudes near 700 km [6–8]. Additional GNSS-R datasets collected by these low-Earth orbit platforms are also available for further analysis and exploration.

1.3 Comparison of Carrier Phase Utility vs GNSS Signal Amplitude and Delay

1.3.1 Overview

GNSS-Reflectometry (GNSS-R) leverages different signal observables—primarily carrier phase, signal amplitude (or signal-to-noise ratio, SNR), and code delay—to infer surface characteristics. Each of these observables provides unique sensitivity to environmental parameters, temporal resolution, and robustness to noise. This section presents a comparative analysis of these observables, highlighting the distinct advantages of using carrier phase in GNSS-R, followed by a discussion on their potential fusion for enhanced sensing performance.

1.3.2 Comparative Analysis of GNSS-R Observables

1.3.2.1 Carrier Phase

The carrier phase of GNSS signals provides exceptionally high temporal and spatial resolution due to its short wavelength (e.g., $\sim$19 cm for the GPS L1 signal). When reflected from surfaces, the phase variations carry information about surface elevation, roughness, and dielectric properties [9, 10]. Phase observables are particularly sensitive to small-scale changes in path length,

making them ideal for detecting fine temporal or spatial variations in the reflecting surface.

1.3.2.2 Amplitude and SNR

The reflected signal amplitude or SNR provides information about the reflecting surface's roughness and dielectric properties. A soil moisture retrieval algorithm was developed and evaluated based on SNR observations acquired from a geodetic-grade GPS receiver, complemented by meteorological data inputs [9, 11, 12]. While [13] proposes a machine learning-based method for detecting snow-covered versus snow-free states using SNR arcs from GNSS-R data, with the goal of improving snow depth retrieval accuracy.

Although SNR-based GNSS-Reflectometry has shown promise for soil moisture monitoring, its reliability is often compromised by limitations in data quality and signal processing techniques. In many studies, the propagation of errors within the SNR data is overlooked—especially when wavelet decomposition is applied for signal smoothing. While wavelet methods can be effective, they introduce additional uncertainty through sensitive parameter choices and potential inaccuracies in signal reconstruction. These challenges are further compounded by the nonlinear amplification of errors during the extraction of multipath-related metrics, which can lead to distortion in the estimated soil moisture signal. To address this, the use of robust statistical techniques, such as the Minimum Covariance Determinant (MCD) estimator, has been proposed. This method offers improved resilience against outliers and noisy measurements, providing more reliable results under conditions where data quality may be compromised [14].

1.3.3 Trade-Offs and Use Case Recommendations

Table 1.1 summarizes the trade-offs among both primary observables.

TABLE 1.1: Comparison of GNSS-R Observables

Property	**Carrier Phase**	**SNR / Amplitude**
Resolution	High (cm-level)	Medium (decimeter-level)
Sensitivity to Moisture	High	Medium
Surface Roughness Detection	High	High
Phase Ambiguity	Present	None
Noise Sensitivity	Medium	High
Computational Complexity	High	Low
Antenna sensitivity	Gain-invariant	Gain-dependent

In summary, carrier phase observables provide superior resolution and sensitivity, making them particularly advantageous in airborne GNSS-R applications and for detecting fine-scale surface variations. While SNR or amplitude measurements are less precise, they remain valuable in conditions where signal coherence is degraded, such as in vegetated or rough terrain. Despite inherent challenges such as phase ambiguity and higher noise sensitivity, the carrier phase remains a highly informative observable for detecting subtle geophysical changes due to its fine spatial resolution and coherence-based sensitivity. The results presented in [15] provide clear evidence that carrier phase-based analysis (phase delay) achieves superior accuracy compared to SNR-based methods in GNSS-R sea level estimation. Specifically, the phase delay approach, which utilizes the difference in phase delay between direct and reflected GNSS signals, yielded root-mean-square (RMS) differences as low as 3.2–3.5 cm when compared to co-located tide gauge measurements. In contrast, the SNR-based analysis produced RMS differences ranging from 4.0 to 9.0 cm, depending on the frequency band and constellation. These results demonstrate that phase-based methods offer enhanced precision and closer agreement with ground truth, particularly under moderate sea surface conditions.

1.4 Review of Existing Carrier Phase-Based GNSS-R Techniques

Carrier phase-based GNSS-Reflectometry has emerged as a powerful technique for retrieving high-resolution geophysical information from Earth's surface. One of the earliest notable works in this domain was presented in [9,

11, 12], where GPS reflected signals were used to monitor soil moisture. This work demonstrated that phase delay and multipath interference observed in the carrier phase could be robustly linked to ground surface characteristics. Building on this foundation, [16] developed the PARFAIT algorithm to extract the coherent carrier-phase component of L1 GPS reflections recorded during the ESTEC Bridge 2 campaign. Demonstrated sea surface height retrieval with cm-level precision (1cm) through coherent phase interferometry.

[17] presents a novel application of GNSS-R using **carrier phase measurements** from the spaceborne CYGNSS mission to estimate river surface slope. A case study on the Orinoco River shows that the retrieved slopes for several river segments range between 3.9 cm/km and 5.1 cm/km, aligning well with the independently surveyed mean slope of 4.5 cm/k for the lower Orinoco. The authors detail the calibration procedures required to correct for systematic errors, including satellite orbit inaccuracies, atmospheric delays, and reference height offsets. A nearby lake reflection is used to calibrate residual errors and enhance retrieval accuracy. The analysis of GPS specular point (SP) tracks demonstrates that CYGNSS has the capability to observe river slopes with high spatial and temporal resolution for rivers of sufficient width, marking an important advancement in remote sensing of inland water dynamics.

The study in [18] establishes the theoretical limits of accuracy for ground-based GNSS-R altimetry using **carrier-phase measurements**. The height between the GNSS-R receiver and the reflecting surface is estimated through a maximum likelihood(ML) approach that fuses carrier-phase information from multiple satellites. The theoretical variance of the estimator is derived as a function of key system parameters: Carrier-to-Noise Ratio (C/N0), satellite geometry, and integration time. This variance corresponds to the Cramer-Rao Lower Bound (CRLB), representing the optimal precision achievable. Both simulations and real data demonstrate that, when multiple satellite signals reflect off the same surface, the achievable height precision reaches the **millimeter level** with integration times on the order of a few milliseconds. This confirms the high potential of carrier-phase GNSS-R for ultra-precise altimetry applications.

The authors in [19] proposed a novel GNSS-R altimetry method that overcomes the limitations of traditional carrier-phase measurements in high sea state conditions, where temporal incoherence degrades phase tracking. The

study introduces an improved algorithm that reconstructs clean direct signals and computes interferometric phase differences between direct and reflected signals in the complex domain. These signals are refined using open-loop tracking with a 60-second coherent integration, enabling the extraction of reliable phase delay measurements without prior carrier-phase tracking. Coastal and shipborne experiments using Quasi-Zenith Satellite System (QZSS) L1 and L5 signals confirm that centimeter-level sea surface height (SSH) accuracy is achievable, even at high satellite elevation angles and under rough sea conditions. Furthermore, the method demonstrates successful ambiguity resolution and platform adaptability, supporting its potential use in low-cost tide gauge applications across static and mobile platforms.

[20] presented a method to enhance GNSS-R sea surface altimetry by improving the continuity and reliability of carrier-phase measurements. The authors introduce a carrier-phase continuity detection algorithm combined with an adaptively weighted fitting strategy based on iteratively reweighted least squares, incorporating coherence-based weights. Applied to CYGNSS satellite data, the proposed method reduces the root-mean-square error of retrieved sea surface height (SSH) to approximately 5 cm, with a 1.59% gain in area-under-the-curve performance. A complementary coastal experiment confirms a precision of 1 cm in SSH estimation and an untracked data ratio of 13%. These results demonstrate the method's effectiveness in ensuring phase continuity and improving SSH retrieval accuracy in GNSS-R altimetry systems.

[21] introduces a high-precision coastal sea surface altimetry method based on dual-frequency carrier-phase measurements from Beidou-Reflectometry (Beidou-R). An integer ambiguity resolution strategy is proposed using B1I and B3I frequencies, combined with a parallel filtering algorithm and an adaptive iterative fusion approach that performs variance-based data fusion. Coastal experiments at the Shenxian River, utilizing reflected signals from GEO and IGSO Beidou satellites, validate the method's effectiveness. The root mean square error (RMSE) of sea surface height (SSH) retrievals is 2.85 cm and 2.89 cm for PRN 04 and PRN 33, respectively. Additionally, the study analyzes the influence of satellite elevation angle on SSH accuracy. The proposed fusion framework significantly enhances carrier-phase GNSS-R altimetry in coastal environments, offering potential for improved tide gauge systems and sea-level monitoring.

[22] proposed a grey model-based prediction method to enhance carrier-phase continuity in GNSS-R altimetry, specifically using BeiDou signals at B1 and B3 frequencies. Recognizing the challenges posed by phase discontinuities, particularly in high-altitude satellite geometries, the method aims to improve sea surface height (SSH) estimation with centimeter-level accuracy. Field experiments using reflected signals from GEO and IGSO BeiDou satellites demonstrate that the grey model improves the reliability of inversion, especially for satellites with large elevation angles. Comparative analysis between B1 and B3 frequency bands confirms enhanced performance in altimetric retrievals using the proposed approach. This work provides a predictive solution to phase loss problems, advancing the robustness of GNSS-R sea surface altimetry.

1.4.1 Example of Observations with Google Earth and Signal Variations

To better illustrate the reflected GNSS signal behavior and its geographical context, Figure 1.3 shows the corresponding trajectory of the flight path for GPS satellite PRN 5 as visualized in Google Earth. The track represents the reflection geometry during a short segment of the GNSS-R acquisition, covering approximately 23 seconds (from seconds 1770 to 1793 of the trajectory). This spatial visualization helps in linking the measured signal variations to the actual surface footprint observed during the flight, providing insight into the physical area contributing to the reflection. In this trajectory, the yellow portion corresponds to a smooth water surface (a lake), while the red segment indicates the transition to a rougher surface (a forested area), thereby illustrating the change in surface type encountered along the path.

Figure 1.4 displays the corresponding reflected signal characteristics in the temporal domain for the same trajectory segment. The top panel shows the normalized amplitude of the reflected signal, while the middle panel presents the phase evolution over time. The third panel provides a zoomed view of the phase over the first 8 seconds, offering a clearer visualization of short-term phase dynamics. These data correspond to the reflected component of the GNSS L1 signal from PRN 5. The joint analysis of amplitude and phase allows observing how coherence varies along the trajectory, highlighting transitions that can later be associated with surface-type changes.

Combining the geographical trajectory and the signal domain representation provides a comprehensive view of both the physical and signal-related aspects of the GNSS-R observation.

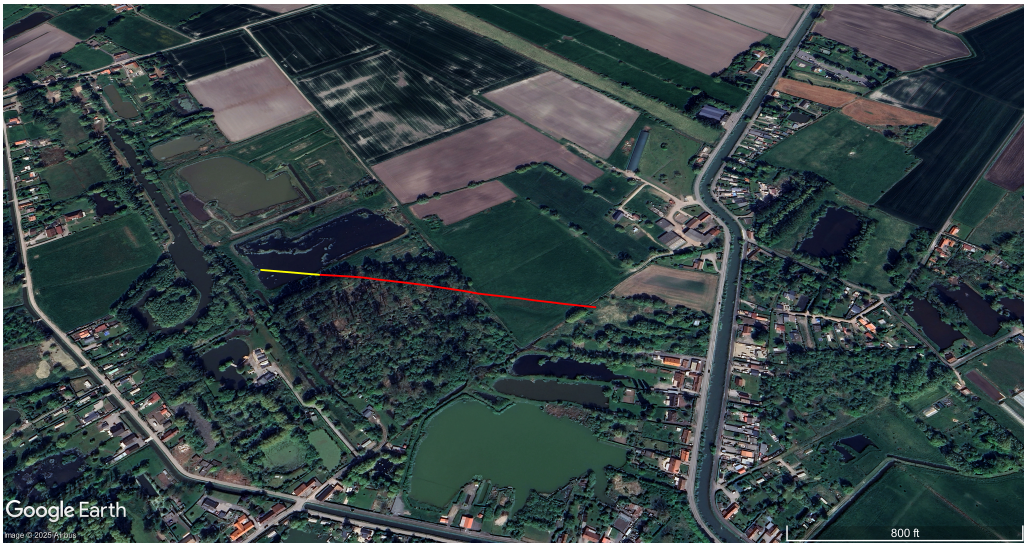

FIGURE 1.3: Google Earth visualization of the reflected signal trajectory of GPS PRN 5 between seconds 1770 and 1793 of the flight.

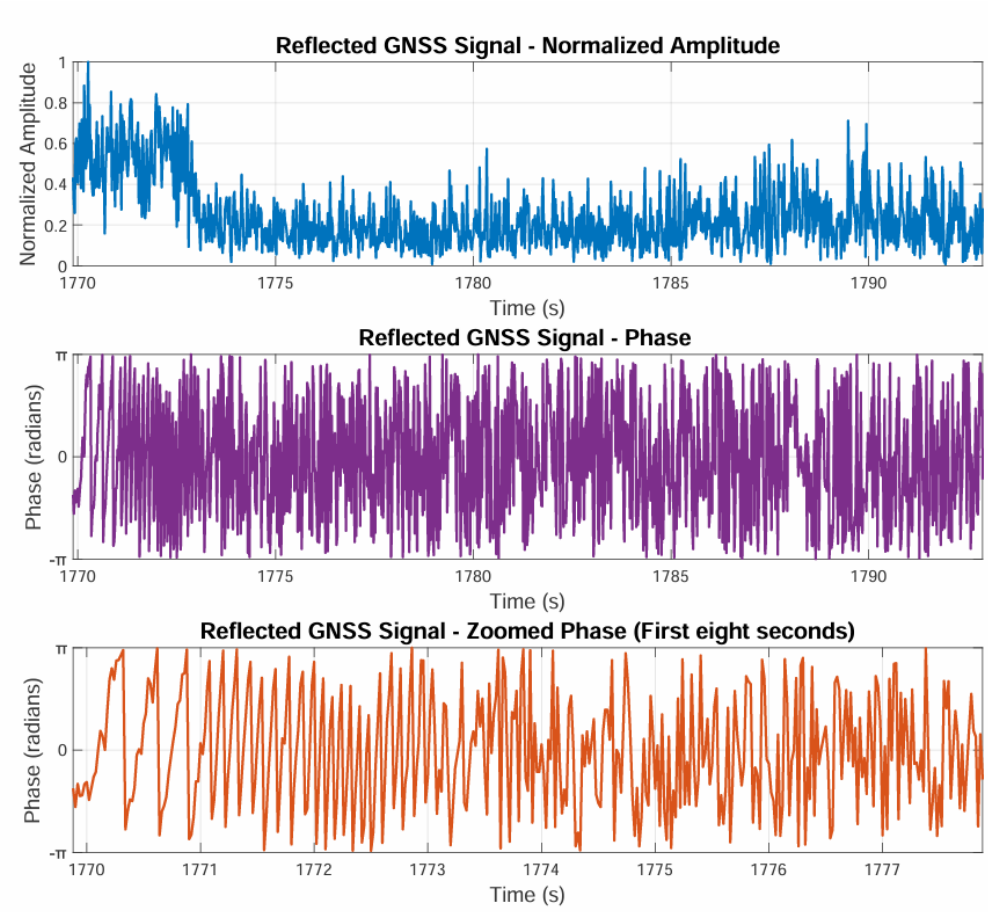

FIGURE 1.4: Reflected GNSS signal from GPS PRN 5 showing the normalized amplitude (top), phase (middle), and a zoomed-in phase segment (bottom) corresponding to the first 189 samples of the 1770–1793 s interval.

1.5 GNSS Signal Processing

Nearly every civilian (consumer and enterprise) receiver supports GPS's L1 signal at 1575.42 MHz, which includes the Coarse/Acquisition (C/A) code, as well the encrypted Precision (P(Y)) code. GPS's L5 signal at 1176.45 MHz was developed for aviation safety. It has higher power and lower frequency.

1.5.0.1 Characteristics

We can notice in Table 1.2 that GPS L5 includes two different codes on the same carrier frequency, with higher rate and longer length than the C/A code of the classic GPS L1 signal. The higher code rate and longer code length imply a larger bandwidth and improved robustness to interference and noise

when processing the signals. The processing indeed relies on the codes auto-correlation functions. The availability of two different codes allows for fusing the retrieved information on both codes. Also, the channel that uses the Q-code is free of data message, which makes its processing more stable. Such channel is called a pilot channel. L1 civil signal doesn't have a pilot channel.

Properties	**L1**	**L5**
Operating-freq(MHz)	1575.42	1176.45
Data-rate(bps)	50	50
PRN code	C/A code	L5-I & L5-Q
Code-rate(Mcps)	1.023	10.23
Code length(msec)	1 ms	10ms for I and 20ms for Q

TABLE 1.2: L1 vs L5 properties [23]

The benefits of the L5 signal include meeting the requirements for critical safety-of-life applications such as that needed for civil aviation. L5 GNSS signal has many advantages such as : Supports safety-of-life applications such as aviation navigation, has stronger power than L1, uses NH-codes which gives better performance in receiving the signal, uses two channels including a pilot channel, has larger bandwidth.

1.5.1 GPS L5 Signal Acquisition and Analysis

This section presents an initial exploratory analysis of the GPS L5 signal conducted at the early stage of this PhD work, with the objective of gaining practical insight into L5 signal characteristics and acquisition behavior, rather than contributing directly to the methodological developments introduced later in this thesis. The following analysis presents the acquisition of the GPS L5 signal from satellite PRN 8 using a static receiver installed on the rooftop of the LISIC site in Calais, France. The GPS L5 signal is transmitted in the L5 band at 1176.45 MHz and is specifically designed for safety-of-life and high-precision applications. Compared to legacy L1 signals, L5 offers higher chipping rates (10.23 MHz), increased signal bandwidth, and improved correlation properties, which enhance multipath resistance and reduce acquisition and tracking errors [24].

The L5I signal component is modulated using the Neumann-Hoffman 10-bit sequence (NH10) superimposed on the pseudorandom noise (PRN) code.

In our experiment, the receiver sampled the L5I signal at 25 MHz. Each coherent integration spanned 10 ms, and ten consecutive code periods were accumulated to increase the signal-to-noise ratio for reliable detection.

1.5.1.1 Acquisition Procedure

The complex baseband signals from GPS PRN 10 and PRN 14 was mixed with a locally generated L5I code replica modulated by the NH10 sequence. Circular correlation was computed across a Doppler search grid centered around the receiver's 1.45 MHz intermediate frequency with a resolution of 40 Hz, covering a 6 kHz span. This two-dimensional correlation, enabled simultaneous detection of both code delay and Doppler frequency.

The peak correlation was identified in the delay-Doppler plane, yielding a detected Doppler frequency of -2480 Hz and a code delay of 6.666 ms and -240 Hz, 1.660 ms for PRN 10 and PRN 14 respectively. These values correspond to the expected Doppler shift caused by the relative motion between satellites PRN (10,14) and the receiver, and the propagation delay of the L5 signal to the receiver. The results confirm that the acquisition algorithm effectively isolates the desired PRN signal from noise and interference.

1.5.1.2 Results and Discussion

Figures 1.5 and 1.6 show the correlation amplitude versus code delay at the Doppler frequency corresponding to the peak and the correlation amplitude as a function of Doppler frequency at the detected code delay. The detected peak at 6.666 ms for PRN 10 and 1.660 ms for PRN 14 precisely indicates the alignment between the received and locally generated code. The sharp peak at 1.44752 MHz reflects the Doppler shift of PRN 10 and 1.44976 MHz for PRN 14, and validates the implemented coherent integration and Doppler search strategy.

The narrow and distinct correlation peaks demonstrate the effectiveness of the L5 signal's NH10 modulation in mitigating multipath and improving detection performance. This also confirms that PRN 10's and 14's signals were sufficiently strong at the Calais site, allowing robust acquisition under real environmental conditions.

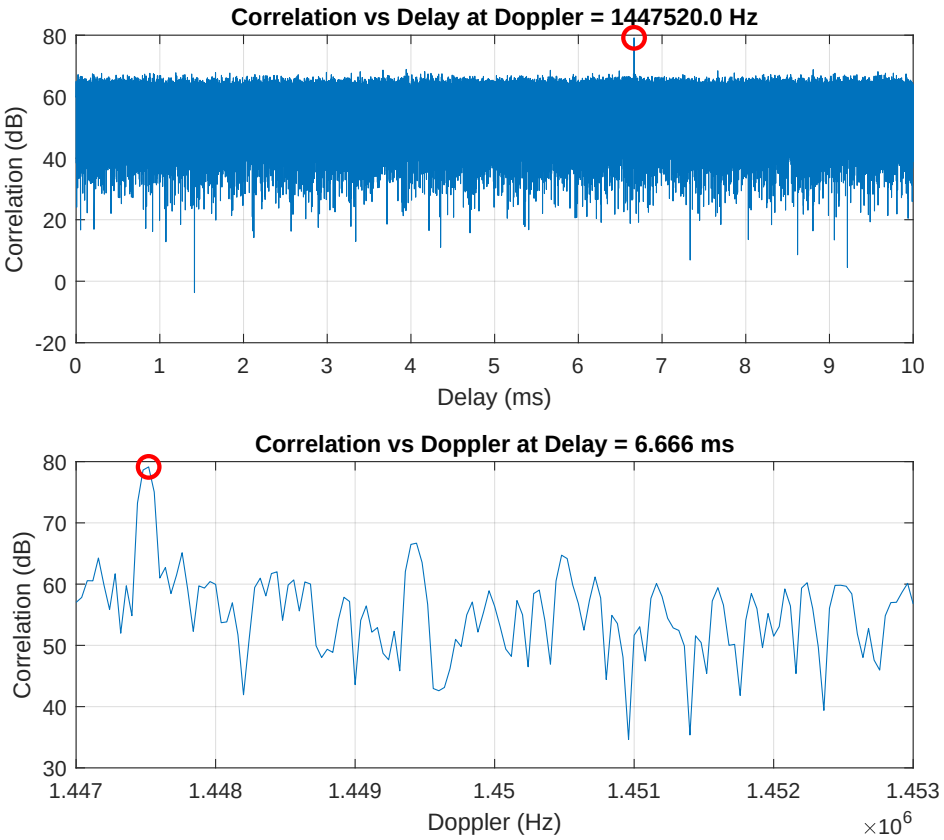

FIGURE 1.5: Correlation amplitude versus code delay at the estimated Doppler frequency on the top, and correlation amplitude as a function of Doppler frequency at the detected code delay at the bottom of PRN 10

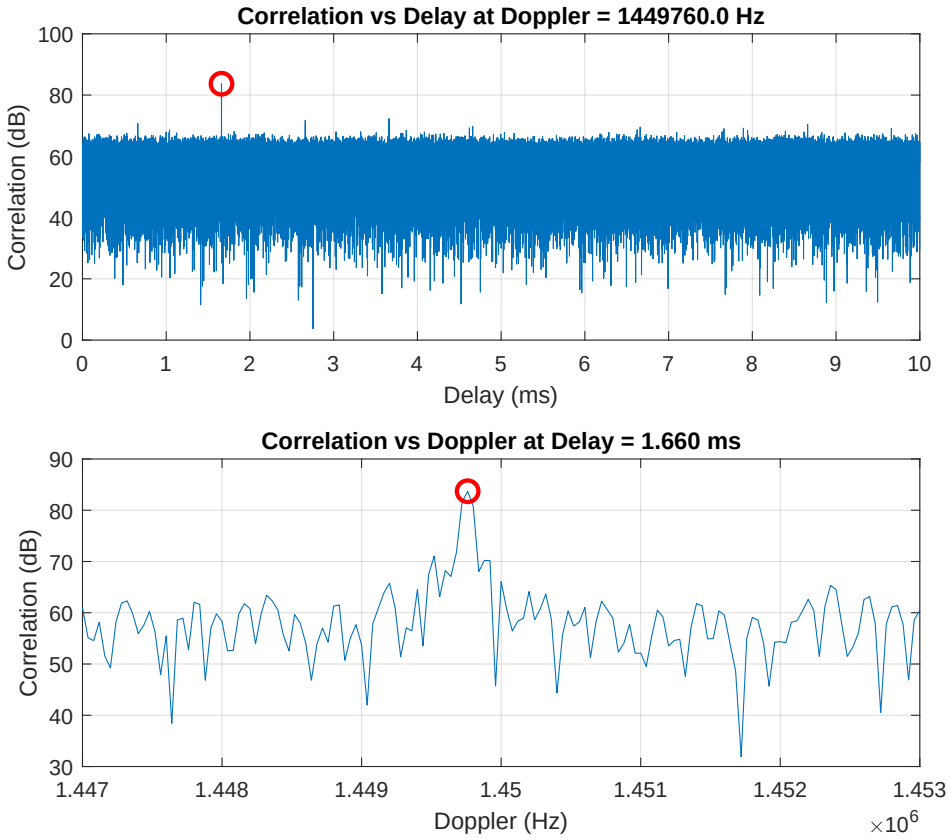

FIGURE 1.6: Correlation amplitude versus code delay at the estimated Doppler frequency on the top, and correlation amplitude as a function of Doppler frequency at the detected code delay at the bottom of PRN 14

Overall, the experimental results confirm the efficacy of the implemented acquisition algorithm for L5 GPS signals.

1.5.2 GNSS-R Signal Processing

Signal processing in GNSS-Reflectometry (GNSS-R) relies on adapted tracking strategies designed to extract both the direct and the reflected components of the GNSS signal. Unlike classical navigation receivers, where the primary goal is accurate positioning, GNSS-R receivers aim to retrieve observables such as carrier phase, amplitude, and Doppler shifts from multipath reflections. In this context, three main tracking architectures are generally employed: *closed-loop*, *open-loop*, and *assisted* tracking. Each architecture presents specific advantages and limitations depending on the level of signal coherence, the geometry of reflection, and the application scenario.

1.5.2.1 Closed-Loop GNSS Signal Tracking

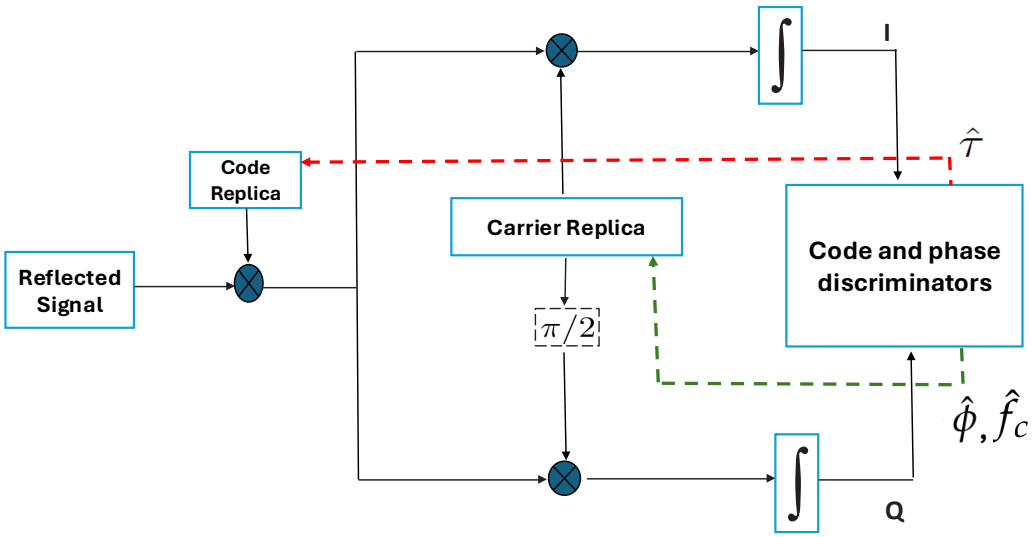

FIGURE 1.7: Closed-Loop Tracking for reflected signal

As shown in Figure 1.7, the Closed-loop tracking is the standard method employed in conventional GNSS receivers. It relies on feedback loops—typically the Phase-Locked Loop (PLL) and the Delay-Locked Loop (DLL)—to synchronize a locally generated replica of the carrier and code with the incoming signal. In airborne GNSS-R applications, a Frequency-Locked Loop (FLL) may also be introduced to compensate for rapid Doppler variations due to sensor motion.

Let $s(t)$ denote the received GNSS signal, composed of the spreading code $c(t)$ and carrier frequency f_c, expressed as

$$s(t) = A\, c(t-\tau)\cos(2\pi f_c t + \phi(t)) + n(t), \tag{1.1}$$

where τ is the code delay, $\phi(t)$ the carrier phase, and $n(t)$ an additive noise term. The local replica $\hat{s}(t)$ is generated by the receiver and adjusted iteratively such that the error between $s(t)$ and $\hat{s}(t)$ is minimized through feedback. The in-phase (I) and quadrature (Q) components are given by

$$I = \int_{T_c} s(t)\cos(2\pi \hat{f}_c t + \hat{\phi})\, dt, \quad Q = \int_{T_c} s(t)\sin(2\pi \hat{f}_c t + \hat{\phi})\, dt, \tag{1.2}$$

where $\hat{f}_c$ and $\hat{\phi}$ are the estimated carrier frequency and phase, and T_c is the integration interval. The tracking error is derived from the discriminator

function (e.g., arctangent or Costas loop), which is then used to update $\hat{f}_c$ and $\hat{\phi}$.

Figure 1.8a shows an example of closed-loop tracking applied on a real direct GNSS signal. The loop maintains lock as long as the signal remains coherent, enabling precise estimation of Doppler and phase.

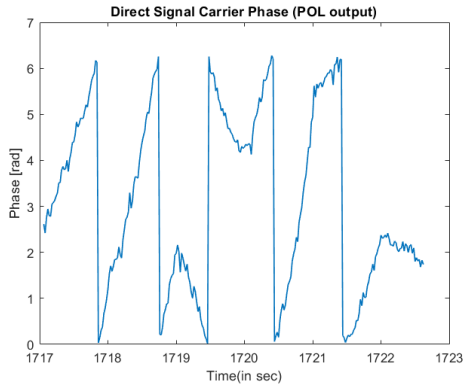

(a) Open-loop tracking applied to the direct GNSS L1 signal from GPS satellite PRN-5, over the interval 1717.06–1722.6 seconds of the flight.

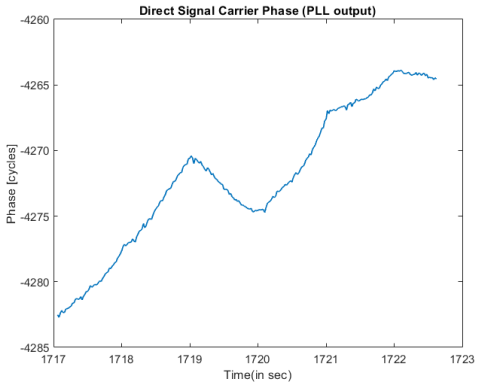

(b) Closed-loop tracking phase of direct signal obtained from GPS satellite PRN-5 over the interval 1717.06–1722.6 seconds of the flight.

FIGURE 1.8: Comparison between open-loop and closed-loop tracking phases for the direct GNSS L1 signal from GPS PRN-5.

1.5.2.2 Open-Loop GNSS Signal Tracking

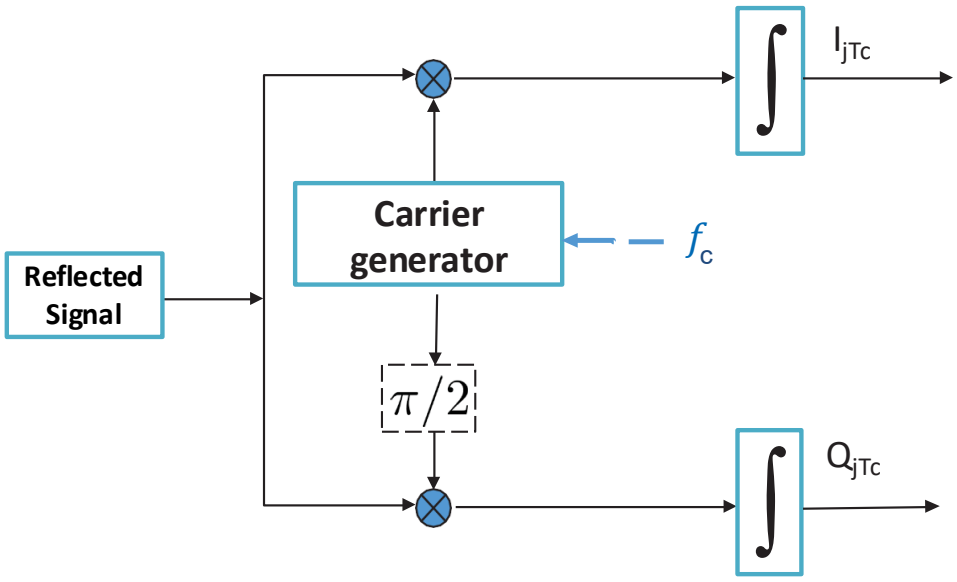

FIGURE 1.9: Open-Loop Tracking for reflected signal

In the context of GNSS-R, closed-loop architectures are often unsuitable for reflected signals due to their low SNR and loss of coherence. To overcome these limitations, open-loop tracking (also referred to as *Phase Open Loop*, POL) is used as explained in Figure 1.9. In this approach, the reflected signal is correlated with locally generated carriers without feedback control. Instead, the estimated parameters from the direct signal guide the processing.

Let the reflected signal be expressed as

$$s(t) = a \sin(2\pi f_c t + \alpha + \omega t) + \eta(t), \tag{1.3}$$

where a and α represent the amplitude and excess phase, $\omega = 2\pi f_d$ denotes the Doppler shift relative to the direct signal, and $\eta(t)$ is Gaussian noise.

The correlation over one integration period T_c yields

$$I_{jT_c} = \frac{a}{2}\cos(\alpha + j\omega T_c) + \eta_I, \tag{1.4}$$

$$Q_{jT_c} = \frac{a}{2}\sin(\alpha + j\omega T_c) + \eta_Q, \tag{1.5}$$

with η_I, η_Q Gaussian noise terms. The observed phase is then obtained as $\tilde{y}_i = atan2(\tilde{Q}_{jT_c}/\tilde{I}_{jT_c})$ which forms the basis of the phase observable used in GNSS-R change detection.

An example of Open-Loop tracking on a real GNSS Direct signal is shown in Figure 1.8b.

1.6 GNSS-R Observables and Measurement Models

1.6.1 Reflected GNSS signal phase measurement

We consider the following expression for a reflected GNSS signal:

$$s_r(t) = \sum_{u=1}^{U} a_u CA(t + \tau_u^r)\sin(2\pi f_1 t + \omega_u(t)) + \eta(t) \tag{1.6}$$

where $\eta(t)$ is a Gaussian noise. $CA(\dots)$ is the CDMA code of the GNSS signal defined as $CA(\dots) \in \{-1, 1\}$. This model assumes the presence of U reflections, each characterized by distinct Doppler shifts—resulting in varying phase errors—and amplitudes. The carrier phase is estimated using a Locked Loop for the direct signal and an Open Loop for the reflected signal,

as described in [25]. It is demonstrated that the two quadrature components provided by the Open Loop at each interval of the CDMA code period T_c can be represented by the following model:

$$I_i = \sum_{u=1}^{U} A_u \cos(\alpha_u + \omega_u i) + \eta_I(i) \tag{1.7}$$

$$Q_i = \sum_{u=1}^{U} A_u \sin(\alpha_u + \omega_u i) + \eta_Q(i) \tag{1.8}$$

where $i \in \{T_c, \ldots, N * T_c\}$. $\eta_I(i), \eta_Q(i)$ are Gaussian noises. $\omega_u = 2\pi f d_u$ with $f_{d,u}$ the excess Doppler associated to the uth reflection. The observed reflected phase can be modeled as:

$$y_i = \arctan\left(\frac{Q_i}{I_i}\right) = \lfloor \bar{y}_i + \xi_i \rfloor \mod 2\pi \tag{1.9}$$

where the phase $\bar{y}_i$ is the weighted sum of the phases $\{\alpha_u + \omega_u i\}_{u=1,\ldots,U}$ in the circular domain and $\{A_u\}_{u=1,\ldots,U}$ are the weights [26]. ξ_i is an additive noise distributed according to a centered Von Mises distribution.

1.6.2 Reflected GNSS signal phase noise distribution

In this work, as mentioned in [27] the phase data noise is assumed to follow a Von Mises distribution. The von Mises distribution is a continuous probability distribution on the circle, often regarded as the circular analogue of the normal distribution. It is characterized by a mean direction μ and a concentration parameter $\kappa \geq 0$.

The probability density function of the von Mises distribution is given by:

$$f(y; \mu, \kappa) = \frac{1}{2\pi I_0(\kappa)} \exp\left(\kappa \cos(y - \mu)\right),$$

where:

- $y \in [-\pi, \pi)$ is the angle (in radians),
- $\mu \in [-\pi, \pi)$ is the mean direction,
- $\kappa \geq 0$ is the concentration parameter,
- $I_0(\kappa)$ is the modified Bessel function of the first kind and order zero.

The modified Bessel function of the first kind and order zero is defined as:

$$I_0(\kappa) = \frac{1}{\pi} \int_0^{\pi} \exp(\kappa \cos \phi)\, d\phi.$$

The mean direction μ represents the average angle around which the data are concentrated. As shown in Figure 1.10, the concentration parameter κ indicates how tightly the data are clustered around the mean direction:

- As $\kappa \to 0$, the distribution approaches the uniform distribution on the circle.
- As $\kappa \to \infty$, the distribution becomes increasingly concentrated around μ.

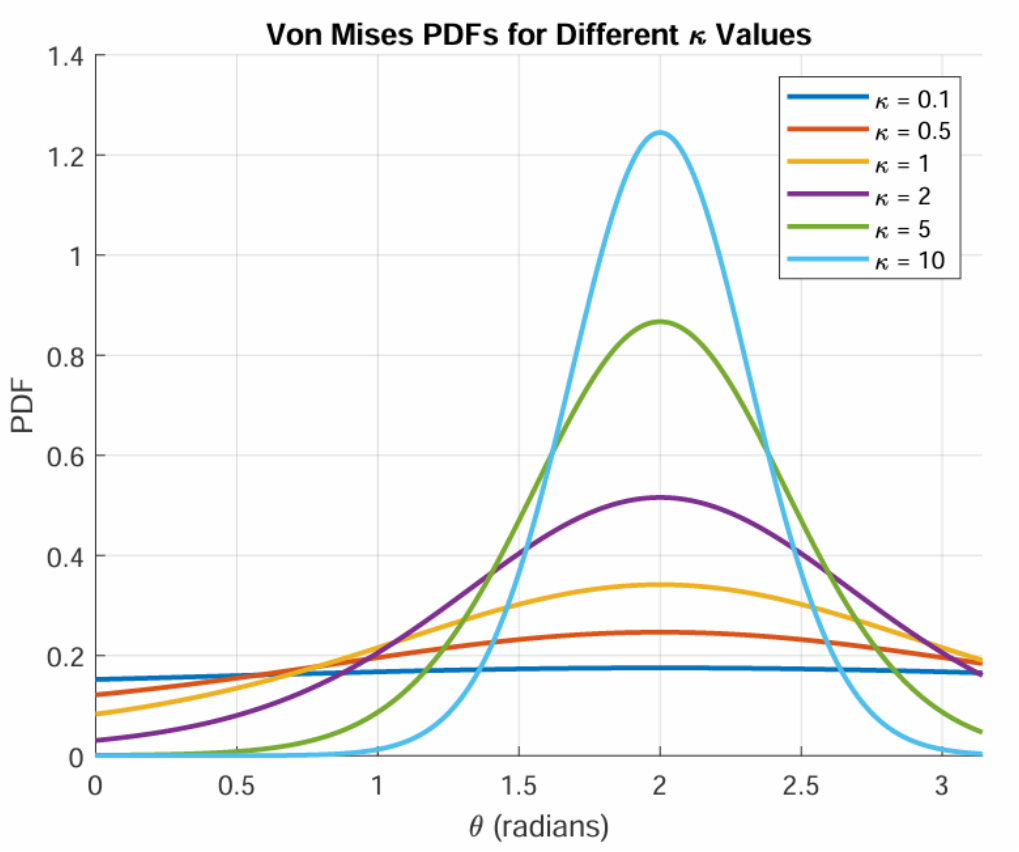

FIGURE 1.10: Probability density functions (PDFs) of the Von Mises distribution for different concentration parameters κ.

As shown in Figure 1.10, each curve corresponds to a different κ value: 0.1, 0.5, 1, 2, 5, and 10, while the mean direction μ is fixed at 2. The distribution becomes increasingly peaked around the mean as κ increases, indicating

higher concentration. For low values of κ, the distribution approaches a uniform distribution on the circle, while for high values, it resembles a normal distribution centered at μ in the circular domain.

The properties of the Von Mises distribution:

- The von Mises distribution is symmetric about the mean direction μ.
- It is often referred to as the "circular normal distribution" due to its similarity to the normal distribution on the real line.
- The distribution maximizes entropy among all distributions on the circle with a specified mean direction and concentration.

1.6.3 Assisted GNSS-R Signal Tracking

Figure 1.11 details the processing of the digitized signals for the retrieval of reflected carrier-phase data using assisted tracking. The direct GNSS signals are processed using classical GNSS signal processing approaches. The reflected signal is tracked in a model-aided open loop, taking as inputs the estimated carrier frequency ($\hat{f}_d$) and code delay ($\hat{\tau}_d$) of the direct signal as well as the modeled delay due to the path difference between the reflected and direct signals. The reflected carrier-phase measured by this open loop is further processed by means of an angular filter derived in [26].

Assisted tracking combines the robustness of closed-loop architectures with the flexibility of open-loop designs. The idea is to exploit the direct signal—which is generally strong and coherent—as a reference for processing the weaker reflected signal. In practice, the carrier frequency f_c and Doppler shift estimated from the direct signal are used to generate the local replica for the reflected signal, thereby reducing the complexity of the search space and improving the robustness of phase extraction.

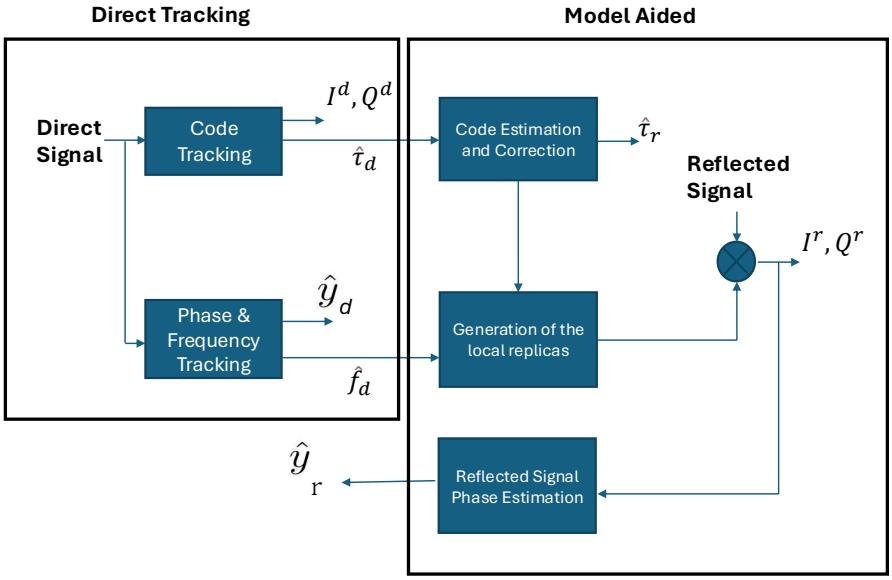

FIGURE 1.11: Reflected GNSS signal phase computing block diagram

In the assisted Phase Open Loop (POL) architecture, the direct signal's parameters are first tracked using PLL/DLL/FLL loops. These parameters are then injected into the open-loop processing chain of the reflected signal, enabling efficient extraction of (I_{jT_c}, Q_{jT_c}) and the corresponding phase y_j. This hybrid approach mitigates the coherence loss caused by multipath and enhances the stability of phase observables in low SNR conditions.

An example of phase observable obtained from assisted tracking on a real GNSS-R signal is shown in Figure 1.12.

1.7 Discussion

In this chapter, we established the role of carrier-phase measurements of the reflected GNSS signal within the GNSS-R framework. We first introduced the GNSS-R technique and outlined its operating principles. We then compared phase-based processing with amplitude-based approaches, highlighting the advantages of using carrier phase for surface characterization. Existing carrier-phase-based GNSS-R methods were also reviewed to situate our work within the current literature.

In this chapter a representative example from our flight experiment is presented. In addition, a dedicated subsection discussed prior work on processing the GPS L5 signal. Finally, we detailed the mathematical basis of GNSS

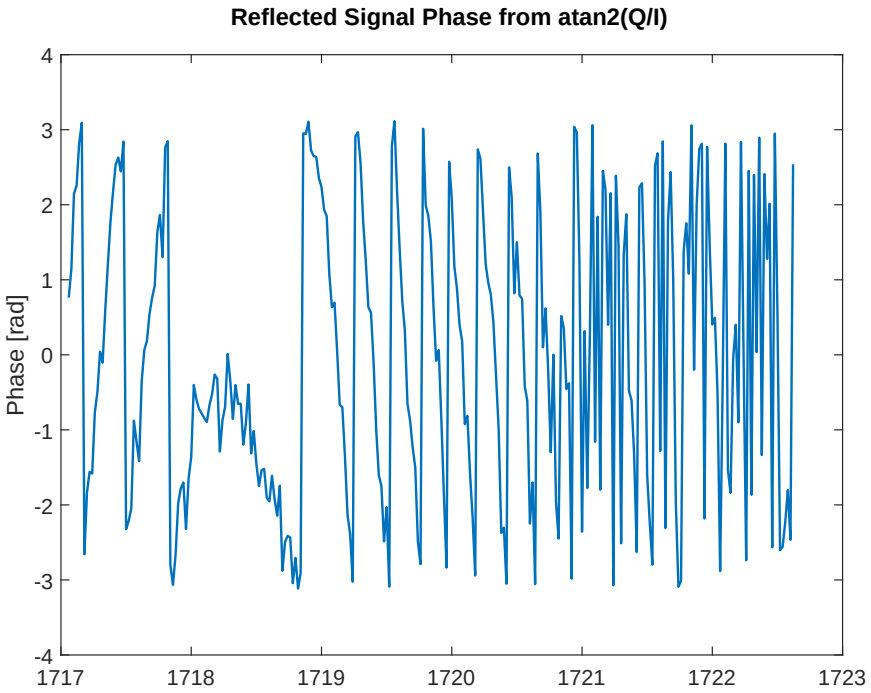

FIGURE 1.12: Assisted tracking phase of reflected signal obtained from GPS satellite PRN-5 over the interval 1717.06–1722.6 seconds of the flight.

signal tracking, with particular emphasis on the reflected carrier phase, its properties, and the procedure used for phase tracking in our analysis.

Chapter 2

Change Point Detection: Literature Review

2.1 Introduction

Change Point Detection (CPD) is a cornerstone of time-series analysis that aims to identify temporal locations where the underlying statistical properties of a signal undergo significant transitions. In the context of this PhD thesis, CPD plays a critical role in interpreting structural changes in refected Global Navigation Satellite System (GNSS) signals. Detecting such changes enables the differentiation of surface types, such as sea, land, or transitional zones—by capturing abrupt or gradual modifications in carrier-phase dynamics. Carrier-phase measurements in GNSS-R are inherently sensitive to surface properties due to variations in reflection geometry and surface roughness. This makes them well-suited for geophysical applications such as sea ice monitoring, wetland mapping, and agricultural land classification. However, their stochastic nature (often characterized by circular statistics, non-stationarity, and multipath interference) necessitates robust CPD algorithms.

This chapter is organized as follows. First, the motivation for applying CPD to GNSS-R carrier-phase analysis is presented by relating surface transitions to changes in distributional parameters and physical scattering regimes. Then, the general mathematical formulation of CPD is introduced through optimization- and Bayesian-based perspectives. The main challenges associated with GNSS-R carrier-phase data are then discussed, including circularity, non-stationarity, noise, and multiple reflections. Finally, the chapter reviews the main families of CPD methods, distinguishing between multiple and single change point detection approaches, and discusses their relevance and limitations for GNSS-R applications.

2.2 Motivation and Relevance to GNSS-R Carrier-Phase Analysis

2.2.1 Change in Distributional Parameters

The motivation behind employing CPD for GNSS-R carrier-phase signals arises from the need to identify surface transitions with high precision under uncertain observational conditions. A surface transition can be modeled as a change in the statistical properties of the carrier-phase data $\{y_t\}_{t=1}^{T}$, where each observation $y_t \in [-\pi, \pi]$ follows a potentially time-varying distribution, often modeled using circular distributions such as the Von Mises distribution:

$$f(y_t \mid \mu_t, \kappa_t) = \frac{1}{2\pi I_0(\kappa_t)} \exp(\kappa_t \cos(y_t - \mu_t)), \tag{2.1}$$

where μ_t is the mean phase, κ_t is the concentration parameter, and $I_0(\cdot)$ denotes the modified Bessel function of the first kind and order zero. A change point τ^* is defined as a time index where the parameters of the distribution experience a change in their characteristics:

$$\exists\, \tau^* : \ (\mu_t, \kappa_t) = \begin{cases} (\mu^{(1)}, \kappa^{(1)}) & t \leq \tau^*, \\ (\mu^{(2)}, \kappa^{(2)}) & t > \tau^*, \end{cases} \tag{2.2}$$

with $(\mu^{(1)}, \kappa^{(1)}) \neq (\mu^{(2)}, \kappa^{(2)})$. In practice, multiple change points may occur, leading to a partition $\{\tau_1, \tau_2, \ldots, \tau_K\}$ of the time series.

2.2.2 Change in the Underlying Model Due to Physical Regimes

In GNSS-R carrier-phase signals, changes may arise not only from shifts in distributional parameters but also from transitions between distinct physical scattering regimes. These regimes affect the generative model of the phase data $\{y_t\}_{t=1}^{T}$, where $y_t \in [-\pi, \pi]$, leading to different stochastic behaviors. For example:

- **Coherent reflection:** The phase evolves smoothly with low variance.
- **Incoherent or multi-path reflection:** The phase exhibits more complex, potentially multi-modal behavior.

Mathematically, we can represent the observations as

$$y_t \sim \mathcal{M}_t, \tag{2.3}$$

where $\mathcal{M}_t$ denotes the generative model corresponding to the scattering regime at time t. A change point τ^* then corresponds to a transition between regimes:

$$\exists\, \tau^* :\ \mathcal{M}_t = \begin{cases} \mathcal{M}^{\text{coh}} & t \leq \tau^*, \\ \mathcal{M}^{\text{incoh}} & t > \tau^*, \end{cases} \tag{2.4}$$

with $\mathcal{M}^{\text{coh}} \neq \mathcal{M}^{\text{incoh}}$ reflecting the change in the underlying reflection mechanism.

Detecting these model transitions allows for identifying and characterizing surface conditions and reflection behaviors that cannot be fully captured through changes in parameters such as the mean phase μ or concentration κ. In practice, multiple transitions may occur, resulting in a partition $\{\tau_1, \tau_2, \ldots, \tau_K\}$ corresponding to distinct scattering regimes.

2.3 Mathematical Formulation of Change Point Detection

The general problem of CPD can be expressed as an optimization over segmentations of the data:

$$\hat{\mathcal{T}} = \arg\min_{\mathcal{T} \subset \{1,\ldots,T\}} \left\{ \sum_{k=0}^{K} \mathcal{C}(y_{\tau_k+1:\tau_{k+1}}) + \lambda\, \phi(K) \right\}, \tag{2.5}$$

where $\mathcal{T} = \{\tau_1, \ldots, \tau_K\}$ denotes the set of change points with $\tau_0 = 0$ and $\tau_{K+1} = T$, $\mathcal{C}(\cdot)$ is a cost or contrast function quantifying within-segment homogeneity, λ is a penalty parameter, and $\phi(K)$ is a penalty function to control over-segmentation. In Bayesian frameworks, the segmentation is treated as a random variable, and inference is performed over its posterior distribution:

$$p(\mathcal{T} \mid y_{1:T}) \propto p(y_{1:T} \mid \mathcal{T})\, p(\mathcal{T}), \tag{2.6}$$

where $p(\mathcal{T})$ encodes prior knowledge on the number and location of change points, and $p(y_{1:T} \mid \mathcal{T})$ is the likelihood of the data under the chosen segmentation.

2.4 Challenges in Change Point Detection for GNSS-R Data

The application of CPD in GNSS-R carrier-phase signals presents unique challenges:

- **Circular statistics:** Carrier-phase is inherently a wrapped quantity ($y \in [-\pi, \pi]$), making standard linear CPD methods unsuitable without adaptation.
- **Non-stationarity:** Environmental conditions and satellite geometries introduce time-varying statistics that require robust detection strategies.
- **High noise levels:** Multipath reflections, receiver noise, and atmospheric effects can obscure subtle surface-induced changes.
- **Multiple reflections:** The presence of overlapping reflection paths complicates the segmentation process.
- **Computational constraints:** Offline methods must balance accuracy with tractable computational costs, especially for long-duration datasets.

The following sections build upon this taxonomy to provide a comprehensive review of CPD methods, distinguishing between Multiple Change Point Detection (MCPD) and Single Change Point Detection (SCPD), and highlighting their relevance to GNSS-R applications.

Change Point Detection (CPD) is the task of identifying points in a time series where the statistical properties undergo significant changes. These changes may represent shifts in the mean, variance, distribution, or higher-order structure of the data, and they are crucial for understanding system dynamics across disciplines such as signal processing, climatology, finance, manufacturing, and GNSS-reflectometry.

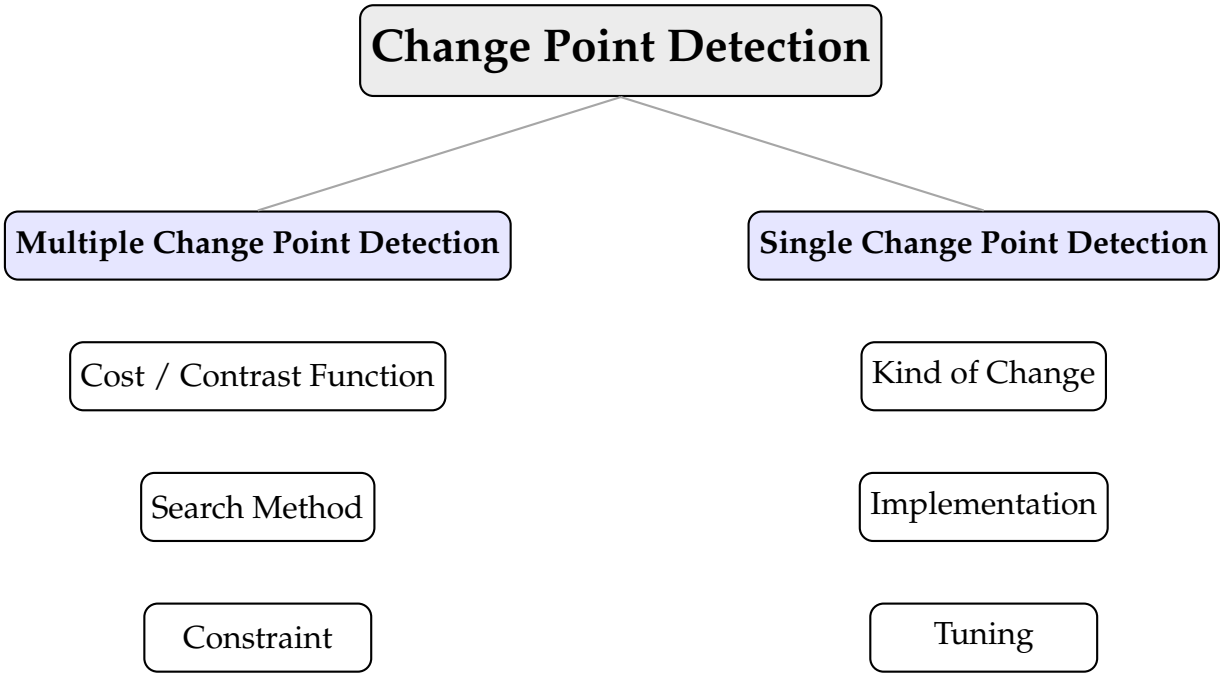

FIGURE 2.1: Structured taxonomy of Change Point Detection based on methodological aspects

We organize the methods based on the nature of the change as shown in Figure 2.1, breaking it down into two main categories: *Multiple Change Point Detection* (MCPD) and *Single Change Point Detection* (SCPD). Each category is then further divided based on key methodological components. For Multiple Change Point Detection, the focus is on the design of a cost or contrast function, the choice of a search method, and the application of constraints. On the other hand, Single Change Point Detection considers the nature of the change being detected, how the method is implemented, and any necessary tuning of parameters. This taxonomy helps in understanding how CPD approaches are typically structured and what elements are considered in their design.

2.5 Multiple Change Point Detection

This diagram shown in Figure 2.2 presents a structured breakdown of Multiple Change Point Detection (MCPD), organizing it into three main components: Cost Function, Search Method, and Constraint. Each of these is further classified to reflect typical methodological choices. The Cost Function can be either parametric, relying on specific distributional assumptions, or non-parametric, which avoids such assumptions and offers greater flexibility. The Search Method describes how potential change points are identified—either using optimal algorithms that guarantee the best solution, or approximate

methods that offer efficiency at the cost of precision. Finally, the Constraint component indicates whether the number of change points is known in advance or needs to be estimated. This taxonomy helps clarify the key design decisions involved in implementing MCPD algorithms.

The design of a cost or contrast function, a search algorithm for locating change points, and constraints governing the number or structure of changes. Cost functions may be parametric, assuming specific data distributions (e.g., Gaussian or Poisson), or non-parametric, offering greater flexibility. [28] provide a comprehensive treatment of parametric statistical change point analysis, presenting methodologies grounded in likelihood-based inference and Bayesian frameworks. Their approach assumes that the underlying data distributions belong to known parametric families, such as Gaussian or Poisson, and change points are identified by examining discontinuities in the estimated parameters. Likelihood ratio tests are employed to assess whether introducing a change point significantly improves model fit, while Bayesian methods incorporate prior beliefs to estimate the posterior distribution of the number and locations of change points. These techniques are particularly effective when strong distributional assumptions can be made, allowing for analytically tractable solutions and well-understood asymptotic properties.

In contrast, [29] introduce the Kernel Change-Point (KCP) detection algorithm, a fully non-parametric method that does not rely on distributional assumptions. KCP is formulated within the framework of Reproducing Kernel Hilbert Spaces (RKHS), where observations are implicitly mapped into a high-dimensional feature space via a positive-definite kernel function. Change points are detected by minimizing a penalized empirical risk criterion, which balances data fit with model complexity. The method estimates the optimal segmentation by selecting the number and location of change points that minimize this penalized criterion, with theoretical guarantees derived from concentration inequalities and model selection theory. The flexibility of the KCP method makes it particularly suitable for detecting complex or subtle changes in data distributions, including changes in higher-order moments or nonlinear dependencies.

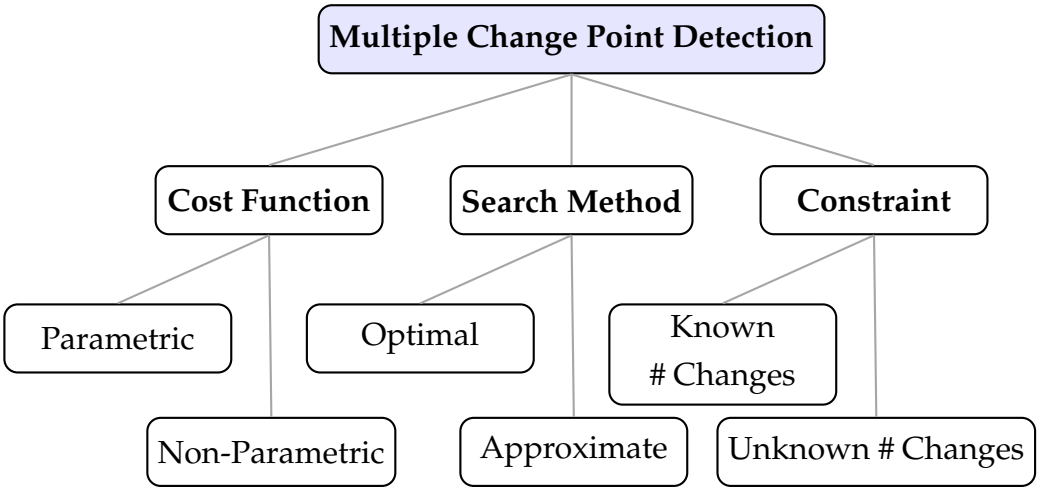

FIGURE 2.2: Detailed taxonomy of Multiple Change Point Detection methods

Change-point detection methods can be broadly categorized into exact and approximate search strategies, with recent advances addressing both computational efficiency and statistical rigor. [30] proposed the Pruned Exact Linear Time (PELT) algorithm, which achieves exact change-point detection with a computational cost that is linear in the number of data points under certain mild conditions. PELT is built upon the dynamic programming principle, which iteratively minimizes a cost function composed of a segment-wise loss term and a penalty on the number of change points to avoid overfitting. The algorithm improves upon traditional dynamic programming by employing a pruning rule that eliminates candidate change points that can be shown not to lead to an optimal solution, significantly reducing the search space. When the cost function satisfies the additive and subadditive properties (such as in least squares or negative log-likelihood settings), PELT guarantees optimal segmentation with proven consistency and linear-time performance in practice.

Complementing this, [31] adopt a Bayesian framework for change-point detection, particularly suited to time series data with complex or unknown underlying distributions. They construct a hierarchical model where change-point locations and model parameters are treated as random variables, enabling the full posterior distribution to be explored. Markov Chain Monte Carlo (MCMC) methods—specifically Metropolis–Hastings and Gibbs sampling—are used to generate samples from the posterior distribution of the number and positions of change points. This approach not only yields point

estimates but also quantifies uncertainty in both parameter values and change-point configurations. Applied to environmental time series data, their method demonstrates the capacity of Bayesian inference to flexibly accommodate data heterogeneity and uncertainty, offering a principled probabilistic alternative to deterministic segmentation algorithms.

Among approximate search strategies for change-point detection, non-exhaustive techniques such as sliding-window and bottom-up segmentation offer computationally efficient alternatives to exact algorithms. As reviewed by [32], the sliding-window method operates by moving two adjacent, fixed-length windows along the data sequence and evaluating a dissimilarity metric—such as the difference in means, variances, or divergence measures—between the windows at each location. Peaks in the dissimilarity profile are then interpreted as potential change points. While this approach does not guarantee optimal segmentation, it significantly reduces computational complexity and is particularly effective in detecting abrupt changes in large-scale datasets. Its simplicity and adaptability to various distance measures make it a widely used approximation technique, especially in settings where fast response times are prioritized over exact segmentation.

In contrast, Bottom-Up segmentation is a hierarchical agglomerative technique that begins with an over-segmented representation of the time series—i.e., dividing it into many small, possibly overlapping segments—and progressively merges neighboring segments based on a dissimilarity criterion. [33] introduced an online Bottom-Up segmentation algorithm designed for real-time processing, achieving linear time complexity and demonstrating practical success in audio and speech segmentation tasks. The method computes pairwise distances (e.g., Euclidean or piecewise linear fit error) between adjacent segments and merges the pair with the smallest distance, repeating the process iteratively while maintaining a global view of the segment structure.

Further insights by [34] highlight the strengths and limitations of Bottom-Up methods. They argue that Bottom-Up is "more generous than greedy," referring to its broader tolerance for segment inclusion during the merging process, which contrasts with top-down or greedy heuristics that may prematurely commit to local minima. While this generosity helps mitigate over-segmentation in noisy environments, it may also result in missed subtle changes if not carefully tuned. The authors emphasize the importance of

selecting appropriate merge criteria and stopping rules to balance detection sensitivity and false discovery, particularly when working with data prone to fluctuations.

In scenarios whhere parametric assumptions about the underlying data distribution are either inappropriate or overly restrictive, non-parametric cost functions offer a flexible alternative for change point detection. These methods do not rely on specific distributional models, making them particularly suitable for complex, high-dimensional, or noisy time series. Among non-parametric approaches, spectral-based methods have emerged as a powerful class for detecting structural changes, especially in signals where distributional shifts are reflected in the frequency domain. By analyzing changes in spectral characteristics—such as power distribution, coherence, or frequency content—these techniques can identify both abrupt and gradual transitions in the signal dynamics. Thier ability to operate effectively on multivariate and non-stationary time series makes them especially valuable in applications such as environmental monitoring, biomedical signal processing, and GNSS reflectometry. In the following, we review key contributions to spectral-based change point detection methods. Spectral change detection methods have been widely explored for analyzing spectral variations in various applications. Recent advancements in remote sensing change detection (CD) methods have addressed challenges such as cross-sensor variability, resolution mismatches, spectral heterogeneity, and computational complexity. [35] proposed an unsupervised CD framework capable of handling substantial spatial and spectral differences between pre- and post-change images by leveraging super-resolution techniques and domain-adaptive learning. Their approach avoids the need for co-registration at identical resolutions and demonstrates robustness across heterogeneous input data. Complementing this, [36] introduced FTA-Net, a lightweight deep neural network that integrates a frequency-domain temporal fusion module and supervised attention mechanisms. Utilizing a Transformer-INN architecture, FTA-Net captures multiscale temporal differences by fusing high-frequency local features with low-frequency global context, enabling improved semantic discrimination in multitemporal imagery.

[37] presented DESSN, a deep learning-based CD model designed for very-high-resolution (VHR) remote sensing imagery. DESSN enhances discriminative difference features through a Difference Enhancement Module

and a Spatial–Spectral Nonlocal Module. Additionally, the model incorporates an Asymmetric Double Convolution structure with Ghost modules, striking a balance between accuracy and computational efficiency. From a classical statistical perspective [38] proposed two unsupervised CD methods based on difference image analysis, applying Bayesian theory to determine decision thresholds and incorporating spatial contextual information. Their use of the Expectation-Maximization (EM) algorithm to estimate the statistical distributions of changed and unchanged pixels improves the robustness and reliability of the segmentation.

To address the spectral misalignment problem in multi-temporal, cross-sensor CD, [39] developed a method based on Kernel Canonical Correlation Analysis (kCCA). By projecting input images into a common latent space, the technique allows the application of conventional CD algorithms while automatically optimizing kernel parameters for enhanced feature alignment and extraction. [40] proposed an improved Change Vector Analysis (CVA) method featuring a Double-Window Flexible Pace Search (DFPS) mechanism to adaptively determine thresholds and analyze the magnitude and directional properties of change vectors, increasing sensitivity to both subtle and abrupt changes. Additionally, [41] developed a Multivariate Alteration Detection (MAD) transformation based on canonical correlation analysis. To further refine change maps, they applied Maximum Autocorrelation Factor (MAF) postprocessing, enhancing spatial coherence and reducing noise-induced artifacts.

Lastly, [42] proposed a fusion-based framework for urban land use/land cover CD by integrating multiple difference images generated from various CD algorithms. Their method employs both feature-level and decision-level fusion on multi-temporal CBERS and HJ-1 satellite images. The fusion strategy significantly reduces omission and commission errors, demonstrating its utility in complex urban environments where single-algorithm detection may be insufficient due to mixed pixels and variable land cover transitions.

Several studies, including [43] and [44], have proposed change detection techniques that leverage spectral variations quantified using Euclidean Distance (ED). ED serves as a fundamental baseline in spectral analysis due to its sensitivity to both shape and magnitude differences in the data. Unlike Pearson Correlation Distance (PCD), which captures only the similarity

in spectral shape and is invariant to scale, ED reflects absolute differences, making it more appropriate when amplitude or intensity variations are relevant. As [45] notes, correlation-based distances "do not account for systematic differences between objects," limiting their effectiveness in scenarios where changes in signal strength or coherence are significant. In this study, we adopt ED as the reference method to benchmark the performance of our proposed Bayesian Change Point Detection (BCPD) approach, which is designed to detect changes involving both spectral structure and magnetude.

2.6 Single Change Point Detection

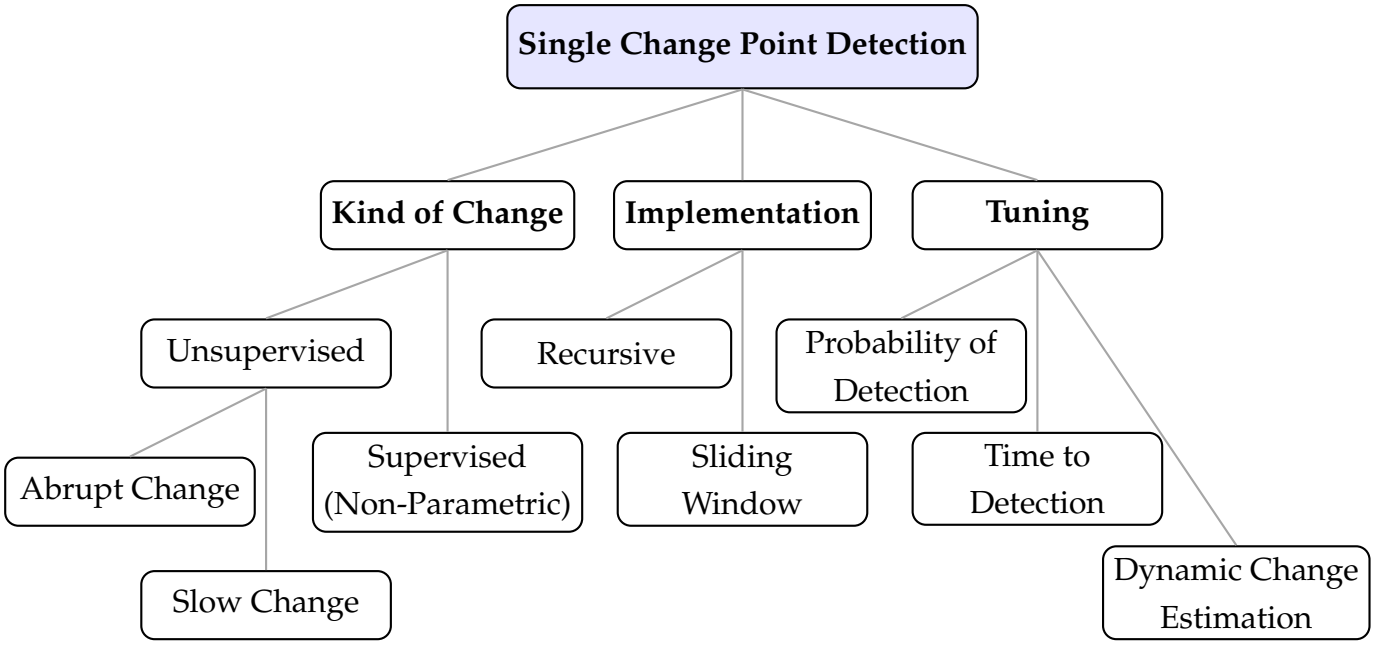

FIGURE 2.3: Detailed taxonomy of Single Change Point Detection methods

The diagram above Figure 2.3 presents a structured view of Single Change Point Detection (SCPD). It is broken down into three core methodological components: Kind of Change, Implementation, and Tuning. The Kind of Change can be Unsupervised, which includes either abrupt or slow changes, or Supervised using non-parametric techniques. The Implementation methods are categorized as either Recursive or Sliding Window strategies. Finally, the Tuning aspect involves optimizing the detection performance through

Probability of Detection, Time to Detection, and Dynamic Change Estimation, depending on the application's sensitivity and reactivity requirements.

SCPD techniques serve as the foundational case of CPD and are essential for theoretical analysis. Classical methods include the Cumulative Sum (CUSUM) procedure introduced by Page [46] for detecting gradual changes, and the Generalized Likelihood Ratio (GLR) test for abrupt changes, originally formalized by Lorden [47]. Bayesian approaches further enhance SCPD by integrating prior knowledge; notable contributions include the work of Barry and Hartigan [48] on partition priors and Fearnhead and Liu's online inference algorithm for multiple change points [49].

Recent advances focus on robust and high-dimensional scenarios. [50] introduced a doubly robust Bayesian framework using beta-divergence, enhancing resilience to outliers and model misspecification.

When the number of change points is unknown, model selection penalties (e.g., BIC, mBIC) are incorporated into the cost function. Yao [51] proposed a method to consistently estimate the number of change-points in a time series using the Schwarz Information Criterion (SIC), also known as the Bayesian Information Criterion (BIC). The approach penalizes model complexity linearly with the number of change-points, helping to avoid overfitting. Yao demonstrated that this penalized likelihood framework leads to consistent change-point estimation, meaning it correctly identifies the true number of change-points as the sample size grows. This paper laid important theoretical groundwork for model selection in change-point problems. While [52] extended the classical BIC by introducing a modified BIC (mBIC) tailored for detecting multiple change-points, especially in genomic data such as comparative genomic hybridization. Their modification accounts for the spacing between change-points, which classical BIC does not explicitly consider. The mBIC leads to improved detection power and lower false discovery rates in scenarios where change-points are sparse and unevenly distributed. Their framework is particularly effective in high-dimensional or large-scale settings and has influenced later developments in statistical genomics and segmentation methods.

Supervised non-parametric methods have also been employed, especially when labeled data are available. Techniques such as decision trees, support vector machines (SVM), and nearest-neighbor classifiers are used to detect

transitions in multivariate time series by learning discriminative segment boundaries [53].

This rich and evolving body of work provides a robust theoretical and practical foundation for applying CPD to diverse and complex datasets, with ongoing innovations addressing challenges such as noise, high dimensionality, and real-time constraints.

2.7 Discussion

The exploration of CPD throughout this chapter establishes its fundamental role in understanding complex, non-stationary signals such as those encountered in GNSS-R. The chapter traced CPD's evolution from classical parametric formulations to advanced non-parametric and Bayesian frameworks, demonstrating how these methods can capture both abrupt and gradual transitions in data. Central to this discussion was the formulation of CPD as an optimization or inference problem, where segmentation decisions rely on the balance between model fit and complexity, typically governed by a cost function and a penalty term. This mathematical framing provides the foundation for interpreting changes in carrier-phase data, a core focus of this thesis.

In the context of GNSS-R, the application of CPD is far from straightforward. The circular nature of carrier-phase measurements, coupled with environmental variability, multipath interference, and potential multiple reflections, introduces distinct challenges that traditional CPD methods are not designed to handle. Addressing these challenges requires adapting or extending CPD algorithms to account for circular statistics, high noise levels, and variable reflection geometries. The reviewed literature revealed that while many existing algorithms achieve high precision in controlled or linear data settings, their direct application to GNSS-R data often results in degraded performance, particularly under realistic, noisy, and mixed-surface conditions.

The review of multiple and single change point detection strategies emphasized how the choice of cost function, search method, and constraint formulation governs detection accuracy and computational efficiency. Parametric approaches, such as likelihood-based and Bayesian models, offer theoretical rigor and interpretability when distributional assumptions hold. In contrast, non-parametric and kernel-based methods provide flexibility and

robustness against model misspecification, making them more suitable for the complex, data-driven nature of GNSS-R phase analysis. Similarly, algorithmic design—ranging from exact search methods like PELT to approximate schemes such as sliding-window or bottom-up segmentation, reflects a constant trade-off between computational tractability and segmentation optimality.

Spectral and frequency-domain methods further extend CPD's applicability by detecting changes in signal characteristics beyond simple amplitude or variance shifts. Their capacity to identify alterations in coherence, frequency content, or power distribution aligns well with the behavior of GNSS-R reflections, where such spectral shifts often signify transitions between different surface types. Recent advances incorporating kernel methods, canonical correlation analysis, and deep learning architectures demonstrate the growing trend toward hybrid and adaptive frameworks capable of handling high-dimensional and non-stationary data.

In summary, this chapter positioned CPD as an indispensable analytical tool for detecting structural transitions in GNSS-R carrier-phase signals. It provided the theoretical and methodological grounding for subsequent chapters, where these principles are adapted and extended for circular data domains and realistic environmental conditions. The insights drawn from the reviewed literature underscore that effective change detection in GNSS-R requires not only statistical precision but also methodological adaptability—balancing rigor with robustness to capture the subtle, complex signatures of surface dynamics in reflected GNSS signals.

Chapter 3

A circular statistical test for change point detection

3.1 Introduction

Circular data is encountered in various scientific and engineering applications where observations are inherently directional or periodic in nature, such as angular measurements, time-of-day records, and phase information in signal processing. Unlike linear variables, circular variables wrap around at a fixed interval—typically 2π radians or 360°—requiring statistical techniques that respect this topology. Classical linear methods often fail to capture the essential characteristics of circular data, motivating the use of specialized tools in the analysis.

This chapter presents statistical methods designed for the circular domain, with emphasis on tests for uniformity. These tests determine whether the observed angular data is uniformly distributed around the circle or if there is evidence of clustering or directionality. Such tests are fundamental in a wide range of applications where uniformity, or its violation, has meaningful interpretations.

Following the theoretical background, the chapter introduces a method for detecting phase coherence based on circular uniformity testing. This approach is particularly relevant in contexts where phase information carries physical significance, such as in GNSS-Reflectometry. In these settings, detecting non-uniformity in the phase distribution may indicate coherent reflection or structural changes in the reflecting surface. The methodology outlined here offers a rigorous yet practical framework for identifying such phenomena using circular statistical theory.

The proposed change detection approach offers a powerful means to capture subtle variations in surface characteristics, enabling precise differentiation between distinct scattering environments. By focusing on the statistical

properties of the observed signals, the method highlights even minor transitions that traditional techniques may overlook. This capability is particularly motivating for studies where accurate identification of surface changes is essential, ensuring reliable insights into dynamic environmental conditions and supporting high-resolution characterization of diverse terrain types.

Section 3.2 consists of an overview about uniformity tests in the circular domain. In sections 3.3 and 3.4, the phase coherence detection method will be proposed and discussed using test for uniformity applied on the reflected GNSS signal phase for both synthetic and real GNSS-R data, where the GNSS-R campaign will be described in this chapter.

3.2 The statistical tests in the circular domain

One of the foundational problems in circular statistics is testing for uniformity, which assesses whether a set of angular data is evenly distributed around the circle or exhibits a preferred direction. A commonly used method for this is Rayleigh's test, this test evaluates the magnitude of the mean resultant vector and compares it to what would be expected under uniformity, with larger vectors indicating deviation from a uniform distribution. Uniformity tests are crucial in disciplines ranging from biology (e.g., animal orientation behaviors) to meteorology (e.g., wind direction patterns), as they help determine whether observed directional trends are statistically significant or due to chance.

Determining whether a set of circular measurements is uniformly distributed (often referred to as testing for randomness or isotropy) can be challenging based solely on visual inspection. Data that appear clustered to the eye may, upon formal statistical testing, conform to a uniform distribution. Conversely, data that look evenly spread might actually exhibit a significant concentration in a particular direction [54].

In [55] the authors showed that for testing uniformity of circular data, Rayleigh's test has many desirable properties such as local optimality, monotonicity and unbiasedness, admissibility, and consistency.

We identify four statistical tests for uniformity to differentiate areas with uniform distributed phase from non-uniform ones. The four tests are Modified Kuiper's test, Watson test, Rao's Spacing and Rayleigh test.

The tests statistics of each of these tests are the measure of the deviation of the circular data from a uniform distribution. They evaluate how well the observed distribution fits the expected uniform distribution. A higher output statistic value indicates a greater departure from uniformity, while a lower value suggests a more uniform distribution.

Let's assume that the phase observations y are sorted in an ascending order as real numbers:

$$-\pi < y_1 \leq y_2 \leq y_3 \leq \ldots \leq y_N < \pi$$

Before implementing the circular uniformity tests, it is essential to demonstrate experimentally that these tests are the most appropriate tools for assessing uniformity in circular data. Specifically, we aim to show that circular tests outperform the widely used linear Kolmogorov-Smirnov (KS) test, which is designed for linear data and may not correctly account for the periodic nature of angular measurements.

3.2.1 Kolmogorov-Smirnov Test for Linear Data

The Kolmogorov-Smirnov (KS) test is a widely used statistical method to test the hypothesis that a sample comes from a uniform distribution on the interval $[0, 1]$ [56]. For a set of N observations $y_1, y_2, \ldots, y_N$, the KS test compares the empirical distribution function (EDF) $F_n(y)$ with the cumulative distribution function (CDF) of the uniform distribution $F(y)$.

The KS test statistic is defined as:

$$D_n = \sup_y |F_n(y) - F(y)| \tag{3.1}$$

where $\sup_y$ denotes the supremum over all y values. A large value of D_n indicates that the sample deviates significantly from the uniform distribution.

It is important to note that the KS test is designed for **linear data**. As we will show experimentally, it does not correctly capture the non-uniformity of circular data, which wrap around 2π.

3.2.2 Kuiper's Test for Circular Data

The modified Kuiper's test [57] measures the distance between the Cumulative Uniform Distribution Function (CDF) and the Empirical Distribution

Function (EDF) on the circle. The test statistic V_n is defined as:

$$V_n = \max_{1 \le i \le N} \left(\frac{y_i}{2\pi} - \frac{i}{N} \right) - \min_{1 \le i \le N} \left(\frac{y_i}{2\pi} - \frac{i}{N} \right) + \frac{1}{N}$$

and the modified Kuiper's test is

$$V = V_n \left(\sqrt{N} + 0.155 + \frac{0.24}{\sqrt{N}} \right)$$

where y_i are the sorted angles of the circular dataset and N is the number of points. The Kuiper statistic V_n is an omnibus uniformity test on the circle, invariant under rotation and equally sensitive to deviations anywhere on the circle, making it appropriate when one seeks a general check for any departure from circular uniformity, though for von Mises–distributed data the Rayleigh test remains more powerful [57].

3.2.3 Watson Test for Circular Data

The Watson test [58] assesses the uniformity of circular data by quantifying deviations from the expected uniform distribution. The test statistic U_2 is:

$$U_2(y) = \sum_{i=1}^{N} \left(y_i - \frac{2i-1}{2N} \right)^2 + \frac{1}{12N} - N \left(\bar{y} - \frac{1}{2} \right)^2 \tag{3.2}$$

where $\bar{y}$ is the mean of the circular data. A high value of U_2 indicates clustering of data, while low values correspond to a uniform distribution. The Watson U^2 statistic is an omnibus uniformity test on the circle that is independent of the arbitrary angular origin, making it appropriate when one seeks a general check for any deviation from circular uniformity [58].

3.2.4 Rao's Spacing Test for Circular Data

Rao's Spacing Test [59] examines the spacing between consecutive ordered angles:

$$D_i = y_{i+1} - y_i, \quad i = 1, \ldots, N-1, \quad D_N = 2\pi - y_N + y_1$$

The test statistic is

$$U_R = \frac{1}{2} \sum_{i=1}^{N} |D_i - \bar{D}|, \quad \bar{D} = \frac{2\pi}{N}$$

A large value of U_R indicates departure from uniformity. Rao's spacing statistic U_R is an omnibus test for circular uniformity, as [60] showed, this test is most powerful invariant against alternatives with a constant density on an arc and its complementary arc, meaning that its rotation-invariant construction makes it sensitive to general deviations from uniformity.

3.2.5 Rayleigh Test for Circular Data

The Rayleigh test RT [61] is based on the mean resultant length R. RT is later defined in section 3.3.1. A high value of RT suggests non-uniformity, indicating a concentration of data points around specific angles. Conversely, a low RT value implies a more uniform distribution of points around the circle. [62] showed that the Rayleigh test RT is particularly suitable to the von Mises circular normal distribution, which is followed by GNSS carrier-phase noise measurements.

3.2.6 Experimental Comparison of Linear vs Circular Uniformity Tests

We applied the above tests to 80 synthetic circular samples divided into 4 segments of 20 samples each:

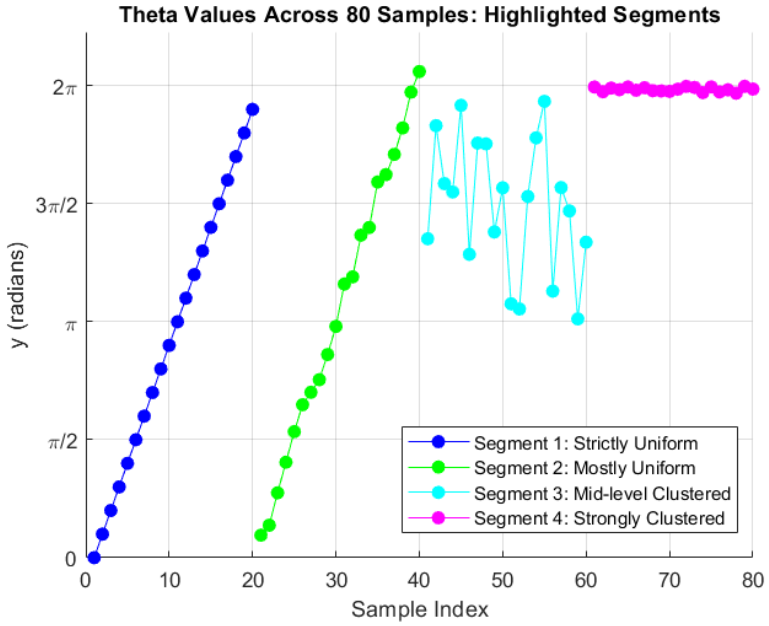

FIGURE 3.1: Circular distribution of the 4 segments. Each segment is plotted with a distinct color.

1. Segment 1: strictly uniform
2. Segment 2: mostly uniform
3. Segment 3: mid uniformity
4. Segment 4: strongly non-uniform

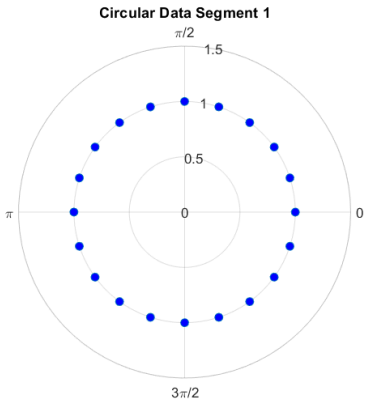

(a) Segment 1: Strictly Uniform

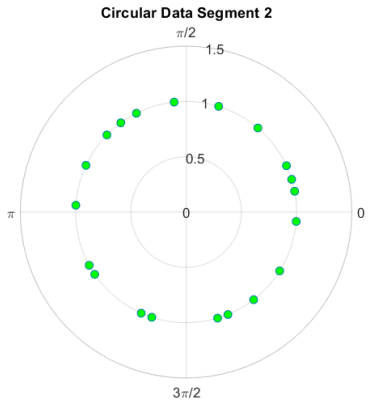

(b) Segment 2: Mostly Uniform

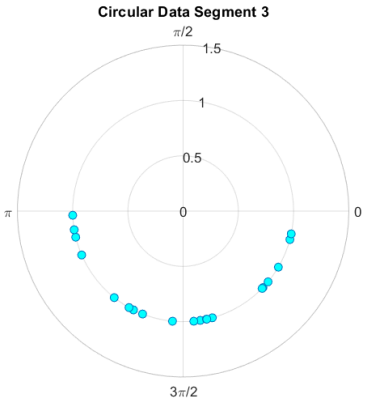

(c) Segment 3: Mid Uniformity

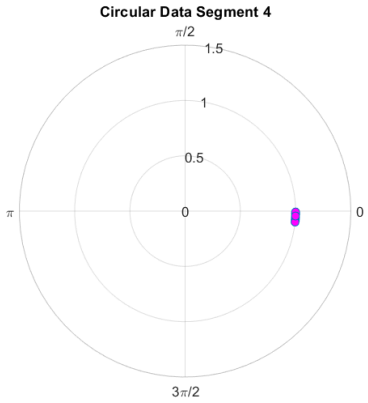

(d) Segment 4: Strongly non-uniform

FIGURE 3.2: Circular distribution of the four segments of synthetic data. Each segment is plotted separately, illustrating the progression from strict uniformity to strong non-uniformity.

The MATLAB simulation produced the following results (test outputs normalized by their maximum value):

Segment	KS	Rayleigh_RT
1	0.59	4.52e-17
2	0.61	0.038
3	0.82	0.66
4	1.000	1.000

TABLE 3.1: KS and Rayleigh test statistics for the four segments of synthetic circular data.

Figure 3.1 illustrates the four segments on the unit circle, showing the increasing deviation from uniformity.

3.2.7 Discussion

From Table 3.1, it is clear that the KS test, designed for linear data, fails to correctly capture the non-uniformity of circular data in segments 1-2. Its values remain relatively high even for segments that are nearly uniform on the circle. In contrast, the Rayleigh test accurately detect the progression from uniformity to non-uniformity.

This demonstrates the necessity of using circular uniformity test when analyzing angular data, as linear tests can produce misleading results due to the periodic nature of circular measurements.

3.3 Phase Coherence Detection using Test for uniformity

Understanding and selecting high-quality remote sensing data often relies on accurate phase coherence estimation and detection. Over recent years, various techniques tailored to a broad spectrum of sensors and applications have emerged to address this need. Within the context of GNSS-Reflectometry, state-of-the-art methods typically employ metrics such as Circular Length (CL) and Circular Kurtosis (CK) presented in [63, 64] to characterize different coherence levels in carrier-phase data. This section explores the potential of circular statistical tests, particularly the Rayleigh Test (RT), for assessing phase coherence in this framework. Given that CL, CK, and RT measurements exhibit fluctuations in both mean and variance with varying coherence levels, a dedicated change detection approach is introduced to effectively handle such variability. Through experiments on synthetic data, the ability of RT to produce more distinct output variations—especially under

oscillatory phase conditions—is demonstrated, outperforming the CL and CK combination. Finally, the RT-based approach is applied to real airborne GNSS-R signals, enabling the segmentation of distinct surface types based on reflected signal characteristics.

Phase coherence represents a fundamental concern in any use of kinematic and/or high-altitude GNSS-R. When multiple reflections of a GNSS signal, originating within the same delay-Doppler cell, arrive at a GNSS-R sensor, the resulting signal becomes non-coherent, affecting all parameters derived by the sensor: the signal's amplitude, carrier frequency, and carrier phase over time. This reception of multiple, phase-shifted signals occurs when the reflecting surface is rough, as illustrated in Figure 1.1. In such situations, temporal phase coherence is compromised because the geometry involving the GNSS satellite, the reflecting surface, and the GNSS-R receiver evolves with time. Therefore, detecting phase coherence becomes essential, similar to other remote sensing applications [65], in the context of GNSS-Reflectometry.

In [66], raw IF samples from the CYGNSS satellite constellation in low Earth orbit (LEO) are examined to detect coherent reflections based on carrier-phase information, highlighting the significance of this process for classifying data potentially suitable for precise phase altimetry. In [67], the coherence of GNSS reflections is identified as a necessary condition for performing sea ice altimetry using L0 raw samples from the TechDemoSat-1 satellite. In [68], the Doppler spread observed in airborne GNSS-R measurements is analyzed to investigate the coherence of the signals, their connection to sea state, and their potential application in retrieving Zenith Total Delay. The research group responsible for [63] and [64] introduced the use of circular statistical indicators on carrier-phase data to assess coherence levels. These indicators, namely the Circular Length (CL) and Circular Kurtosis (CK), are employed together to categorize GNSS-R data as non-coherent, semi-coherent, or coherent. Their methodology was applied to data from LEO satellites (Spire, CYGNSS) for the purpose of mapping inland water bodies, which is also a key objective of the forthcoming HydroGNSS space mission [69].

In this study, we present an innovative approach for detecting coherence in GNSS-R carrier-phase data using uniformity tests. These tests are designed to evaluate the extent to which angular data are dispersed within their defined interval [61]. Within this framework, uniformity signifies that all values around the circle are equally probable. The work reported in [70]

offers a concise summary of frequentist methods for assessing circular uniformity, including Kuiper's test, Rayleigh test, Rao's spacing test, Watson's test, and Ajne's test. In [62], it was demonstrated that the Rayleigh test (RT) is especially well-suited to the von Mises circular normal distribution, which characterizes GNSS carrier-phase noise measurements. Accordingly, this test will be employed in this work to quantify the coherence level of phase data. Additionally, a change detection method relying on a cost function appropriate for multi-dimensional time series that vary in both mean and variance—characteristics shared by the (CL,CK) in [63, 64], and RT outputs—will be utilized to identify sudden changes in the coherence level of circular phase data, as indicated by RT outputs and by the combined use of CL and CK outputs.

The ability of the RT outputs, as well as the combined CL and CK outputs, to detect changes in carrier-phase coherence was evaluated using synthetic data. The results will indicate that RT provides the most distinct and contrasted responses, particularly when the phase data exhibits oscillatory behavior, highlighting its superior sensitivity in capturing variations in coherence levels.

3.3.1 Phase Coherence Metrics

The Circular Length (CL) and Circular Kurtosis (CK), proposed for coherence assessment in [63, 64], are given by:

$$CL = \frac{1}{N}\left|\sum_{i=1}^{N}\cos y_i + \sum_{i=1}^{N}\sin y_i\right| \tag{3.3}$$

$$CK = \frac{1}{N}\sum_{i=1}^{N}\cos\left(2(y_i - \bar{y})\right) \tag{3.4}$$

The normalized Rayleigh test (RT):

$$RT = \frac{1}{N^2}\left|\sum_{i=1}^{N} e^{jy_i}\right|^2 \tag{3.5}$$

In these formulations, y_i denotes the circular samples under analysis, and N represents the total number of samples $(y_1, y_2, \ldots, y_N)$ used to compute a single output for CL, CK, or RT. The term $\bar{y}$ corresponds to the mean value of these N samples, and j is the imaginary unit. The values of CL and RT range

between 0 and 1, while CK varies from -1 to 1.

The measurements considered in this work are reflected GNSS signals carrier-phase values ϕ_i as processed by open-loop tracking algorithms, that correlate the received signal with a reference, clean-replica signal created using the modeled carrier-phase delay and carrier-frequency of that signal [68, 71]. When the carrier-frequency model accuracy is limited, which is the case in practice as it depends over several partly unknown parameters such as the geometry of the reflection, the atmospheric delays between the reflected and the direct signals and the phase wind-up effects [72], the observed carrier-phase values vary over time along a general trend function of the carrier-frequency error $errf$, which itself evolves over time:

$$\phi_{i+1}^{trend} = \phi_i^{trend} + 2\pi.errf_i.dt \tag{3.6}$$

with dt the sampling period, taking value 1ms in our work. In order to remove the phase variations due to the frequency error $errf_i$, [63] and [64] apply the formulas of CL and CK to carrier-phase noise measurements obtained as ε_i defined as $\varepsilon_i = \phi_i - \hat{\phi}_i$ with $\hat{\phi}$ a smoothed version of ϕ
. The objective is to obtain carrier-phase noise measurements only linked to the inner properties of the reflecting surface (roughness, permittivity, ...). However, the filters used for smoothing the phase cannot fully estimate the many components of the carrier-frequency error and random oscillations remain present in the carrier-phase noise measurements.

Figure 3.3 (top) presents a set of such carrier-phase noise data for different levels of concentration parameter κ, modeled as following the von Mises distribution, with (blue) and without (red) such oscillation residuals. The corresponding values of the CL, CK and RT outputs are displayed in the bottom part of this same figure. The (CL,CK) combination of outputs appears to be more sensitive than RT to oscillations in phase noise measurements, with a typical shift of the (CK,CL) curve shape towards larger values of CK and lower values of CL.

3.3.2 Change Detection Method

In this work, we apply a multi-dimensional change detection method, described in [32], to segment the RT outputs and the (CL,CK) paired outputs, treating them as two-dimensional datasets. The change detection strategy

adopted here is based on the cost function referred to as C3 in [32]:

$$c_{\Sigma}(x_{a..b}) := (b-a)\log\det\hat{\Sigma}_{a..b} + \sum_{t=a+1}^{b}(x_t-\bar{x}_{a..b})'\hat{\Sigma}_{a..b}^{-1}(x_t-\bar{x}_{a..b}) \tag{C3}$$

where $\bar{x}_{a..b}$ and $\hat{\Sigma}_{a..b}$ denote the empirical mean vector and the empirical covariance matrix, respectively, for the subset $x_{a..b}$ of a multi-dimensional sequence x_t between time indices a and b. Here, $M = b - a$ represents the size of the window for the cost computation. In the framework of this study, x_t corresponds to the temporal evolution of the RT and (CL, CK) coherence measures. The C3 cost function is particularly suited for detecting shifts in both the mean and variance of the input signal, which matches the observed behavior of the coherence indicators in this analysis.

The computation of this cost function is performed using the window sliding approach:

$$d(x_{a..t}, x_{t..b}) = c(x_{a..b}) - c(x_{a..t}) - c(x_{t..b}) \tag{3.7}$$

where $(1 \leq a < t < b \leq T)$. An illustration of the values taken by $d(\cdot)$ when x_t corresponds to the RT or (CL, CK) computations for carrier-phase noise measurements affected by residual oscillations is shown in Figure 3.4. It can be observed that, although all indicators effectively highlight changes in the coherence of phase noise measurements, the $d(CL, CK)$ cost function exhibits peaks even at locations where the coherence level remains constant, and sometimes its maximum values are shifted from the actual change points. These effects are attributed to the residual oscillations present in the phase noise measurements. In contrast, the $d(RT)$ cost function does not exhibit such behaviors.

The change detection on phase coherence level is performed on the values taken by $d(\cdot)$ over time in four steps:

- Apply a smoothing filter (e.g., moving mean) to $d(\cdot)$ in order to smooth local, negligible maximums.
- Detect the set of maximums on the filtered outputs (e.g., by locating the zeros of its empirical derivative).

- Apply a threshold to the detected maximums. Maximums satisfying this threshold are considered as the detected changes, with locations $(M_1, \ldots, M_P)$ in time.
- Locate the maximum of the raw values of $d(\cdot)$ closest to each of the M_i positions. This defines the estimated location of the detected changes.

3.4 Experimentation

This section is divided into two main parts: first, the validation of the proposed approach using synthetic data under controlled coherence changes, and second, its application to real airborne GNSS-R measurements for practical surface characterization and change detection.

3.4.1 Synthetic Experimentation

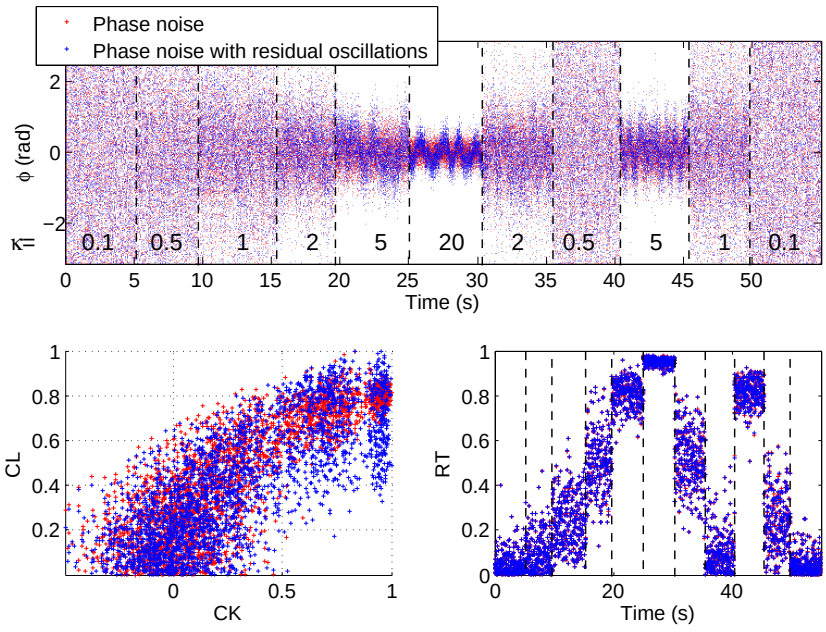

FIGURE 3.3: Simulated phase noise; Circular Length (CL), Circular Kurtosis (CK) and Rayleigh Test (RT) outputs for 10 changes in coherence (black doted lines) ($dt = 1$ms, $N = 20$).

The experimentation on synthetic data follows the scheme described in the previous sections. Phase noise samples are simulated every 1 ms, corresponding to the GPS L1C code period, the outputs of the CK, CL and RT coherence indicators are computed over $N = 20$ samples, meaning at a 50 Hz

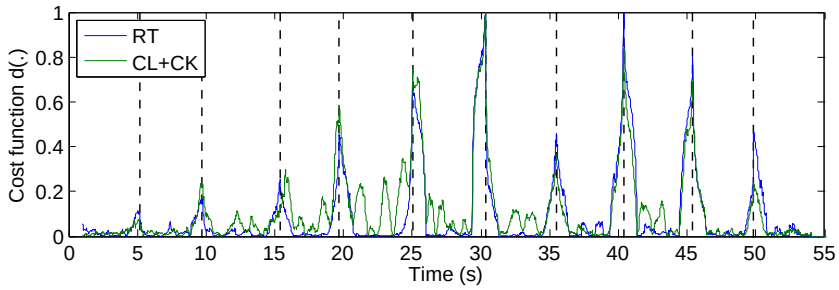

FIGURE 3.4: Cost functions $d(RT)$ and $d(CL,CK)$ for 10 changes in coherence (black doted lines) in phase noise measurements affected by residual oscillations ($dt = 1$ms, $N = 20$, $M = 100$).

rate, and the cost function C3 is computed in a window of size $M = 100$. A moving mean filter over 50 cost function samples (1 s) is performed for its smoothing. The changes are located with a resolution of 20 ms.
The (CL,CK) and RT approaches are compared in terms of good detection and false alarm rates, and in terms of estimation accuracy through the mean and standard deviation of the location of the detected change (Mean Time to Detect). For both approaches:

- A change detection located 1.5 s before or after an actually simulated coherence change, whose positions are randomized every 5 s with 0.5 s uncertainty (see Figure 3.3, top), is considered as a good detection. If more than one change is detected for the same simulated change, the additional detections are considered as false alarms.
- Change detections located outside such a 1.5 s interval from either side of an actual change are considered as false alarms.

Change in κ	0.1→0.5	0.5→1	1→2	2→5	5→20	20→2	2→0.5	0.5→5	5→1	1→0.1
Percentage of good detection (%) – CL+CK	62	88	100	100	100	100	100	100	100	100
Percentage of good detection (%) – RT	59	91	100	100	100	100	100	100	100	100
RMSE on localization (ms) – CL+CK	492	428	348	155	204	20.0	152	7.53	8.12	158
RMSE on localization (ms) – RT	349	164	22.5	29.6	19.0	9.83	11.7	7.13	8.12	62.4

TABLE 3.2: Rate of good detection and RMSE on localization for changes in coherence.

The change localization accuracy is computed independently from the change detection process by computing the position in time of the maximum of the raw cost function $d(.)$ inside each 1.5 s interval from either side of an actual change.

The thresholds applied for detecting changes in the variations of (CL, CK) and RT are both fixed so that the overall good detection rate is 95%. Table 3.2 presents the details on the probability of good detection and the mean error and standard deviation on the change localization as a function of the considered coherence changes, which are similar to those of the example in Figure 3.3. Values of κ from 0.5 to 5 are those that have been observed for the data used in the following real data section (with a phase measurement sampling rate of 1 kHz).

The results are in accordance with what was observed in Figures 3.3 and 3.4: while both approaches present similar ability at detecting changes between the same levels of coherence κ, with only changes between two very low levels of coherence not being detected, the RT approach outperforms the (CL, CK) approach in terms of false alarm rates. The RT approach significantly reduces the probability of false alarms, yielding a false-alarm probability of 5.45×10^{-5}, compared to 2.49×10^{-3} for the CL+CK method (per 55 s signal).

The RT approach also outperforms the (CL, CK) approach in terms of estimation accuracy in the location of the detected change, typically providing 10 to 30 ms accurate locations in terms of standard deviation, except when the changes occur between two highly non-coherent phase segments ($\kappa =$ 0.1 to 0.5, 0.5 to 1, or 1 to 0.1). The (CL, CK) approach only displays accuracies similar to those of the RT approach either in the extreme cases of changes between two highly different, easy to differentiate, segments ($\kappa = 0.5$ to 5 or 5 to 1) or in the case of two highly non-coherent, very difficult to differentiate, segments ($\kappa = 0.1$ to 0.5). The mean localization errors, or Mean Time to Detect, do not display apparent offsets for either approach. Since the localization process is performed offline, their values can be negative.

3.4.2 Real Data Application

As discussed in [71], a dedicated flight mission was conducted in northern France on October 19, 2020, commencing at 14:45 UTC and concluding at 15:30 UTC, with a total flight duration of 45 minutes. The operation was carried out using a gyrocopter that departed from the Calais–Dunkerque Airport, situated in the commune of Marck, approximately 7 kilometers east-northeast of Calais, within the Hauts-de-France administrative region. The flight path extended over an area adjacent to the English Channel, covering

an approximate linear distance of 71 kilometers. The trajectory encompassed the regions between Calais, Escalles, and Ardres. A graphical representation of this flight path is illustrated in Figure 3.5.



FIGURE 3.5: Reflections traces of three GPS satellites (PRN 5, PRN 7, and PRN 30), corresponding respectively to path in (blue), path in (green), and path in (red). The tracks are visualized over the region of Northern France, in Calais. Each trajectory represents the spatial evolution of the specular reflection points detected during the airborne GNSS-R campaign.

A lightweight and compact GNSS-R system was specifically developed and integrated onto a gyrocopter. The system includes a GNSS-R sensor composed of a bit-grabber, an RHCP antenna and an LHCP antenna to capture GNSS signals. The RHCP antenna is positioned at the front of the gyrocopter to acquire direct GNSS signals, while the LHCP antenna is mounted underneath the aircraft to collect reflected signals. A drone board sensor complements the setup by recording the gyrocopter's attitude, altitude, and position relative to GPS Time throughout the flight.

Although the gyrocopter is a manned aircraft, it is capable of flying at very low altitudes and relatively low speeds while maintaining high maneuverability. These characteristics are essential for our application, which seeks to maximize the spatial resolution of airborne GNSS measurements. The footprint size of the satellite signals is directly influenced by the receiver's altitude. The gyrocopter can cover distances of up to 500 km during a single flight lasting approximately four hours. Operating at higher altitudes would extend the coverage area and increase the volume of data collected

TABLE 3.3: Summary of flight parameters during the GNSS-R measurement campaign [71]

Parameter	**Value**
Date of Operation	19 October 2020 (14:45 UTC)
Survey Region	North of France
Flight Duration	45 minutes
Mean Flight Velocity	95 km/h
Average Flight Altitude	315 m
Sampling Rate (Parent/Child)	25 MHz / 1 kHz
Satellites Used	PRN 5, PRN 7, PRN 30 (elev. $> 50°$)
GNSS Signal	GPS L1 carrier ($\sim$1575.42 MHz)

by the airborne GNSS-R system within the same flight time; however, this would come at the cost of reduced spatial resolution. Thus, a balance must always be struck between achieving high spatial resolution and maximizing overall coverage. Figure 3.6 illustrates the gyrocopter used for the flight experiments, along with the various sensors installed on board.

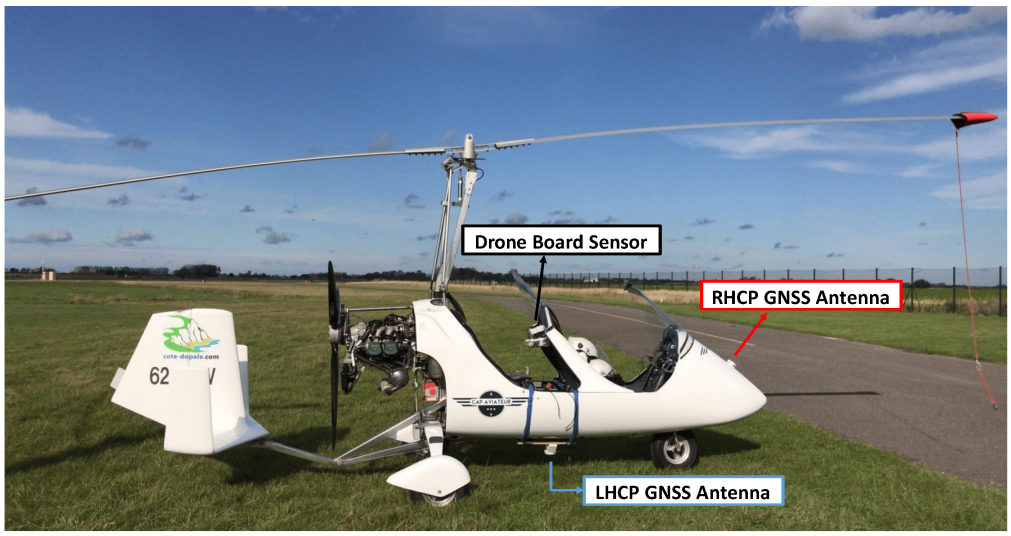

FIGURE 3.6: The gyrocopter used during the flight was equipped with embedded sensors [71].

Table 3.3 presents the key details of the airborne GNSS-R acquisition campaign:

In this study, airborne GNSS-R measurements were acquired at an average altitude of 315 meters using a gyrocopter traveling at approximately 95 km/h. The raw signal was sampled at 25 MHz, while the recorded data

(GPS L1 only) was processed at a 50Hz rate (parent) and reprocessed at a 1kHz rate (child) for time resolution purpose. Given the platform's velocity, this corresponds to a spatial displacement of approximately 0.53 meters between consecutive specular reflection points, resulting in a temporal resolution of 20 milliseconds per footprint. This configuration enables sub-meter spatial resolution along the reflection tracks. Furthermore, since a GNSS receiver can simultaneously process signals from multiple satellites, the system benefits from broad spatial coverage and high-density surface sampling. While spaceborne GNSS-R typically yields reflection tracks spaced hundreds of kilometers apart, the airborne setup used here provides significantly finer spatial detail, which is critical for localized surface monitoring and coherence analysis.

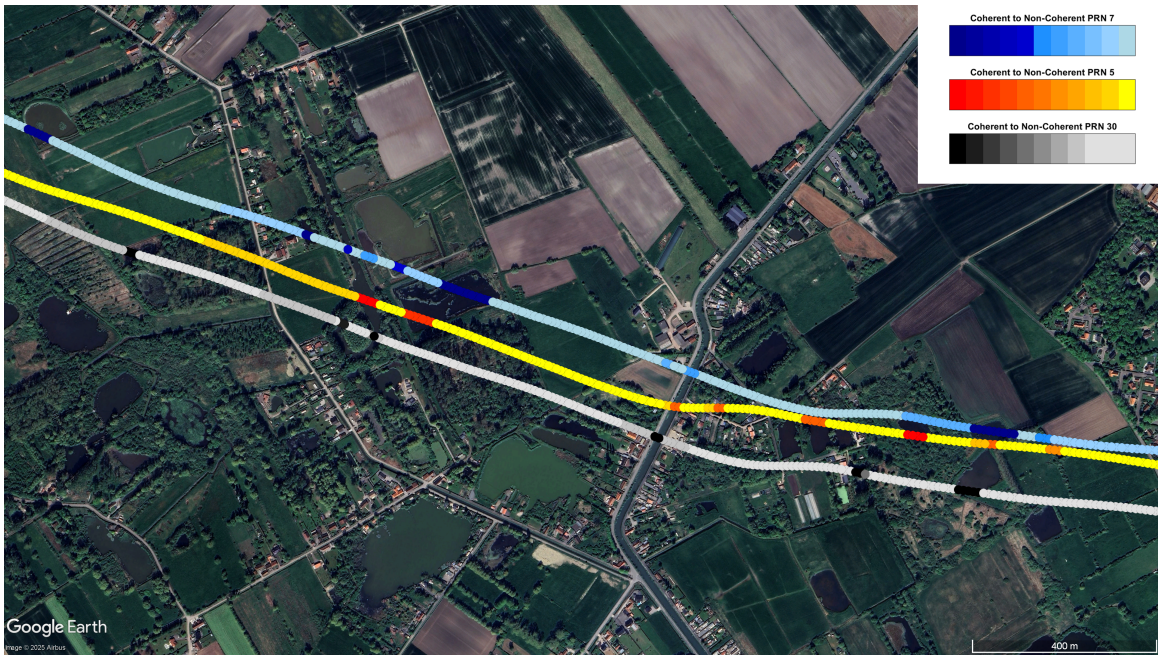

FIGURE 3.7: Coherence levels as traces of the GPS satellites of PRN 5, 7 and 30 along a section of the flight trajectory (50.8763°, 1.9548°).

In [71], segmentation of the measured signals reflectivity was performed. In this section, segmentation is realized based on the RT change detection approach described above. The parameters used are the same as for the synthetic case ($N = 20$, $M = 100$, detection threshold), as the concentration parameter of the phase noise is similar. A sample of results of this segmentation corresponding to ∼2.5 km of reflection traces over highly irrigated terrain is displayed in Figure 3.7. The associated $d(.)$ cost function and raw and segmented RT outputs, computed at a rate of 50 Hz, are displayed in Figure 3.8.

Levels of RT phase coherence segments between 0.07 and 0.4 have been determined over the area, which consists of fields, forests, villages, ponds, and canals. These levels of coherence are displayed as color tones on the reflection traces as computed knowing the positions of the satellites and receiver over time. It can be observed that all water bodies along these traces have been detected by the RT approach as smooth, coherent surfaces. Fields and forests are more difficult to distinguish by phase coherence levels, with low sensitivity in the data of PRN 5 but better differentiation for PRN 30. The ability of the proposed approach to accurately locate and estimate the size of the detected items can be appreciated in the figure.

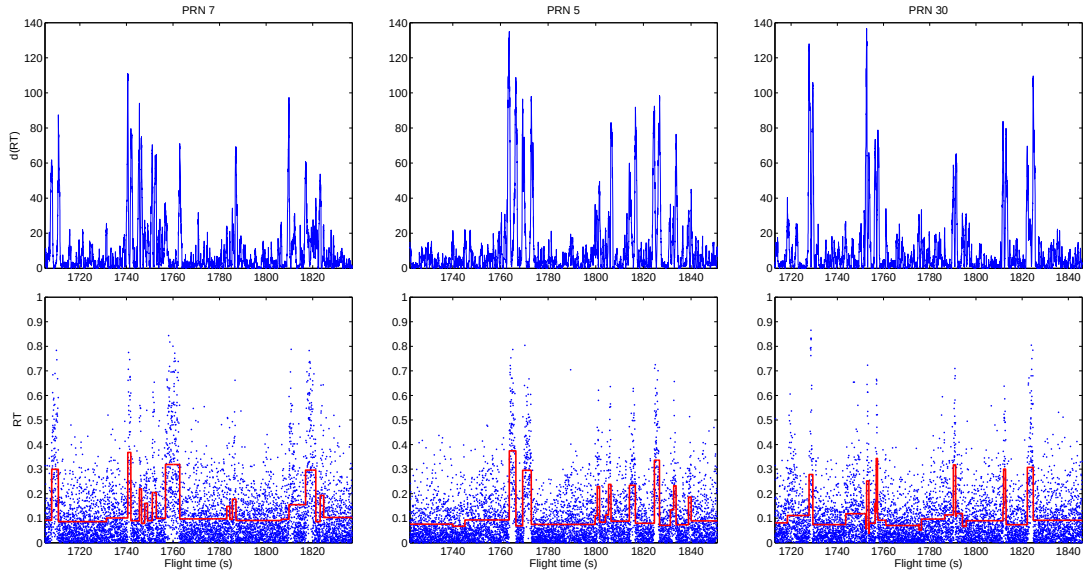

FIGURE 3.8: Reflected-signal analysis for GPS satellites PRN 7, PRN 5, and PRN 30. The upper panels show the cost function. While the lower panels show the corresponding Rayleigh test statistic (RT) used to quantify phase coherence over the flight time, where the blue points represent the RT values computed from the reflected carrier phase, and the red shows the means of RT

An overview of the phase coherence levels obtained by the proposed RT segmentation approach over the complete flight trajectory is displayed Figure 3.9. Various items of interest were detected, such as:

- the sandy beach of Les Hemmes de Marck (North-East), displaying the highest continuous levels of coherence over the whole flight,
- the dike and port of Calais (North) with the dike and port entrance displaying particularly low levels of coherence,

- long sections of agricultural areas with consistently low coherence levels (South West, East),
- the various water bodies present in the swampy area between Guînes (50.8889°, 1.8681°) and Ardres (50.8755°, 1.9680°).

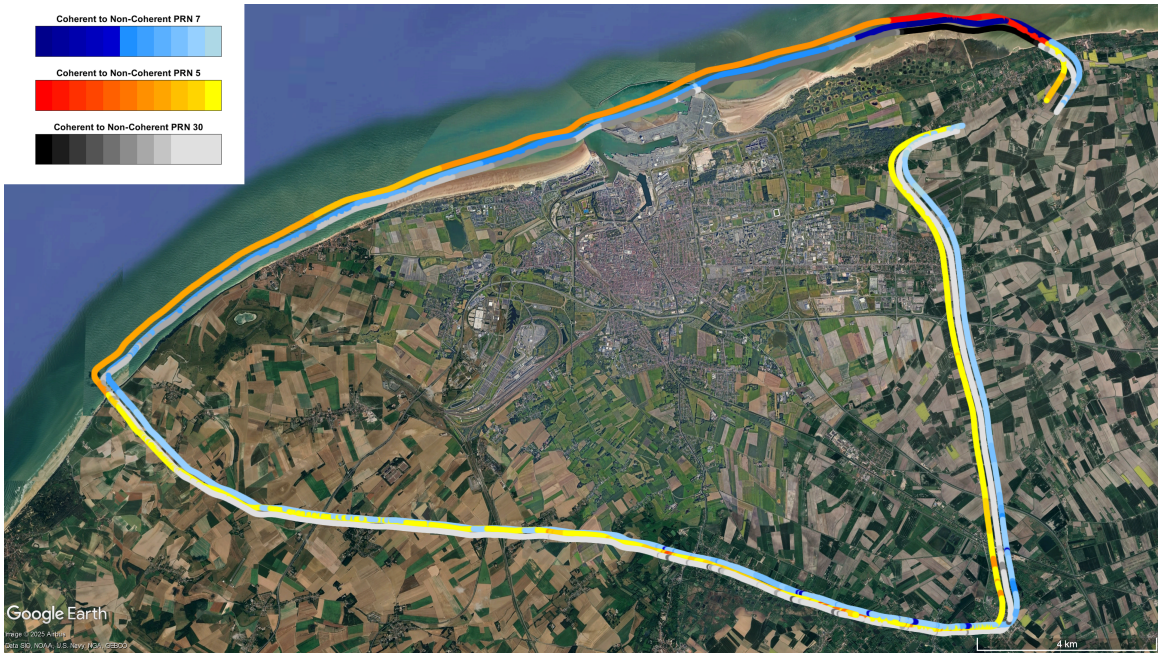

FIGURE 3.9: Coherence levels as traces of the GPS satellites of PRN 5, 7 and 30 along the complete flight trajectory.

3.5 Discussion

The work in this chapter was dedicated to studying the use of circular uniformity tests for the detection of coherent phase data in remote sensing, and more particularly in GNSS-Reflectometry. Phase coherence detection not only allows for the selection of remote sensing data that can be used for a range of applications, but it can also, by itself, be a source of information on the sensed surfaces. The computation of phase coherence indicators usually relies on the extraction of phase noise information from the global signal phase, a process that is imperfect due to the nature of the noise data. In this chapter, we showed on synthetic data that the Rayleigh uniformity test is particularly well-suited for separating noise information from other residual oscillations. Rayleigh test output segmentation is performed using a change detection approach that is sensitive to changes in both the mean and variance of an input signal. The proposed approach is shown to be able to accurately

detect and localize changes in phase noise coherence. The application of the proposed approach to real airborne GPS L1 reflectometry data demonstrates its ability to detect different types of small water bodies on land. It also shows promise for the detection of forests and other types of surface and land moisture. Perspectives in this respect include the added use of other GNSS signal frequencies and reflectivity information.

Chapter 4

Bayesian Offline Change Detection Applied to GNSS-Reflectometry Phase Data

4.1 Introduction

We can find in the published works number of applications where the data are first acquired before being processed. In this case the processing is off line and the multiple change point detection process is the piecewise segmentation of the signal. Multiple change point in the data model exist for many time series, with application to economic [73], industrial quality control [74], genetics, medicine, finance [75]. Multiple change point estimates rely on a contrast function that can be defined with parametric models or non-parametric approaches [76]. In the case of parametric models, the pieces of the signal can be distinguished by their statistic properties (Likelihood, Bayes and Mahalanobis approaches [76, 77]), their structural model (Multiple regression approach [75]). Non-parametric approaches can be supervised or non-supervised and include non-parametric Maximum likelihood, rank based detection, kernel-based detection or spectral detection (Spectral distances [78]).

This chapter is about parametric change in the structure of a model. In this context, change detection can be realized by fitting the model on each segment of the signal. Obviously this approach rely on the estimation of the parameters of the model and the change instants. The proposed change point detector belong to the family of regression models. We can find in the published works of the parametric approaches, several regression models used to design change point detector. In [79] a maximum likelihood estimate is designed for change point detection in peace wise linear regression model.

In [80] a Bayes estimate based on a vague prior probability density was proposed. As a generalization of the linear model, multiple linear model was also investigated for the design of change point. In [81] a least mean square estimate of the change point was proposed and a Bayesian estimate was designed in [82]. The linear factor models and partially linear time-series are multiple linear regression used in economics and finance. It is proposed in [83] a likelihood ratio test for the estimate of a structural break in the factor loading matrix. For a partially linear time-series it is proposed in [84] a structural change estimate in the parametric component of the model. In the case of on-line structural change point detection, we can find in the published work several recursive approaches based on AR, ARMA or state model of the process. In [85] and [86, 87] a change point estimate of the structural parameters is respectively proposed for an AR and an ARMA process. A state equation can model the linear evolution of a process. In this context it is proposed in [88] a change point estimate based on the detection of change in the innovation of a Kalman GLR filter.

In our radar application the data are measurements of phase obtained as a function of time by a moving sensor that observe the earth [25, 89]. We show that the phase model of the observed data (associated with the variation of the earth surface) is a piecewise circular multiple regression model. A circular random variable is a directional variable defined on the circle, taking values in $[0, 2\pi]$. In the circular domain there is several multiple regression models [55, 90]. In a circular-circular regression model the response and the explanatory variables are both circular data. A linear-circular regression model defines the linear relationship between a linear explanatory variable and a circular response. In our radar application the model is linear circular because we have measurements of phase between $-\pi$ and π as a function of time. The model is multiple because it is defined as the weighted sum of several linear circular regressions.
Unlike the linear case there is no direct estimate of the parameter of a multiple linear circular regression. Assuming that the observation are corrupted by a circular noise distributed according to a centred Von Mises distribution, in [91] a maximum likelihood estimate (MLE) of the model parameters was proposed. It was shown in [92] that this estimate, based on an iterative method has several solutions according to its initialization leading to ambiguously defined MLEs. To address this problem, it was proposed to map

the real line to the circle with a monotonic function $g(q)$ that maps the multiple linear regression model q from $(-\infty, \ldots, \infty)$ to $[-\pi, \ldots, \pi)$. In [92] it is proposed to define $g(.)$ as the marginal distribution of the noise and an unambiguous iterative estimate is derived for the case of a single explanatory variable. The function $2\,arctan(.)$ is used in [93] in the case of a multiple linear regression. Unfortunately for these approaches, due to the use of non-linear functions, the estimated parameters are not the real parameters of the linear regression that fit the data when the explanatory variables are not close to zero. It is pointed out in [94] that for these approaches the likelihoods are multimodal and the global are difficult to find. Spherically projected multivariate linear models were proposed to solve this issue [94–96]. In those cases, the model parameter estimation requires computationally expensive approaches [97]. In [97] a transformation of dependent circular variable distributed according to non-negative trigonometric sums distribution is proposed. This method transforms a circular random variable to a unique linear random variable such that commonly used linear regression models can be fit to the transformed linear variable.

In this work we propose a penalized contrast function derived from a Bayesian modeling of the multiple change point detection problem in a piecewise linear circular process. For this multiple linear circular model, we propose to estimate the parameters in the spectral domain. We present the physical meaning of these parameters regarding our application. The multiple linear circular regression model is the weighted sum of circular linear models. We show that this model is linked to our GNSS-R application.

This chapter is organized as follows. First, a reference spectral change detection method based on the Euclidean Distance is introduced to provide a benchmark for comparison. Then, the proposed Bayesian framework is developed by presenting the linear circular model, the posterior formulation, and the penalized contrast function used for offline multiple change point estimation. The link between this statistical model and GNSS-R reflected carrier-phase observations is then established through the radar observation model and the derived phase model. Finally, the proposed method is validated on synthetic phase data and real airborne GNSS-R measurements, including transitions between coherent and non-coherent reflection regimes such as lake–land and rough-terrain–stadium scenarios.

4.2 Method of reference

This section presents the reference method used for performance comparison with the proposed Bayesian Change Point Detection (BCPD) framework. There is no parametric change point estimate in the published work for our problematic. In this context, non-parametric cost functions offer a flexible alternative for change point detection. Among non-parametric approaches, spectral-based methods have emerged as a powerful class for detecting structural changes, especially in signals where distributional shifts are reflected in the frequency domain. By analysing changes in spectral characteristics—such as power distribution, coherence, or frequency content—these techniques can identify both abrupt and gradual transitions in the signal dynamics. Their ability to operate effectively on multivariate and non-stationary time series makes them especially valuable in numerous applications. The method of reference is presented, where a spectral change detection approach based on the Euclidean Distance is introduced as a non-parametric benchmark for evaluating the proposed method.

Several studies, including [78], have presented this type of change detection techniques that leverage spectral variations using spectral distances. Euclidean Distance (ED) serves as a fundamental baseline in spectral analysis due to its sensitivity to both shape and magnitude differences in the data. Unlike Pearson Correlation Distance, which captures only the similarity in spectral shape and is invariant to scale, ED reflects absolute differences, making it more appropriate when amplitude or intensity variations are relevant. As [78] notes, correlation-based distances "do not account for systematic differences between objects," limiting their effectiveness in scenarios where changes in signal strength or coherence are significant. In this study, we adopt ED as the reference method to benchmark the performance of our proposed Bayesian Change Point Detection approach, which is designed to detect changes involving both spectral structure and magnitude.

The contrast function used to detect spectral changes in our Bayesian framework is defined with the Euclidean Distance by the following formulation:

$$ED(\underline{\hat{r}}, \underline{\hat{\theta}}(\underline{\hat{r}})) = \sum_{i=1}^{nb} \left(T_1^i - T_2^i \right)^2 . \tag{4.1}$$

where T_1^i and T_2^i represent the power spectrum values for the first and

second segments and n_b is the number of points used to compute each spectrum. A lower Euclidean distance signifies a greater similarity between spectra, thereby indicating minimal change in the observed region. This method of reference is compared to the proposed approach.

4.3 Bayesian estimate

4.3.1 Linear circular models

We can distinguish several linear circular models in the published works. Let's consider $q = (1, q_1, \ldots, q_U)^T$ to be a vector of covariate values (the linear explanatory variables) associated, in the regression model, to a set of parameters $\boldsymbol{\omega} = (\alpha, \omega_1, \ldots, \omega_U)^T$. We denote by y the circular response of the linear circular regression model and by α the intercept of the regression. The classical linear circular model is the wrapping of the linear model in the circular domain. This model can be defined as follows :

$$\rightarrow z = atan2\left(\frac{sin(\boldsymbol{\omega}^T q)}{cos(\boldsymbol{\phi}^T q)}\right) \tag{4.2}$$

with the following model of observation :

$$y = \lfloor \rightarrow z + \xi \rfloor \ _{\text{mod } 2\pi} \tag{4.3}$$

where ξ is a centered noise distributed according to a Von Mises distribution in [91], an offset normal distribution in [94], and a non-negative trigonometric sums distribution in [98]. $atan2$ is the four-quadrant inverse tangent and $\lfloor \rfloor \ _{\text{mod } 2\pi}$ denotes the conversion between $-\pi$ and π. In this expression the regression function is assumed to spiral infinitely many times around the cylinder. For a single spiral the following models were proposed :

$$\rightarrow z = 2\pi F(\boldsymbol{\omega}^T q) \tag{4.4}$$

$$\rightarrow z = 2 \tan^{-1}\left(\text{sign}(\boldsymbol{\omega}^T q)\left|\boldsymbol{\omega}^T q\right|^{\gamma}\right) \tag{4.5}$$

Where $F(\ldots)$ is the marginal distribution of the noise [92], γ a parameter to estimate [93]. The observation y is assumed to follow a centered noise distributed according to a Von Mises distribution. For a set of K linear regressions, [97] proposes the following linear circular observation model:

$$y = \boldsymbol{\omega}^T q + 2k\pi - \pi + \xi \tag{4.6}$$

In this model k takes several values $k \in \{k_0, \ldots, k_K\}$ with $k_i \in \mathbb{Z}$. ξ is a Von Mises distributed noise. The weighted sum of data in the circular domain is defined in [99]. In this context another circular model is the weighted sum of U linear model in the circular domain :

$$\rightarrow z = atan2\left(\frac{\sum_{i=1}^{U} a_i \sin(\alpha_i + \omega_i q_i)}{\sum_{i=1}^{U} a_i \cos(\alpha_i + \omega_i q_i)}\right) \tag{4.7}$$

where a_i is a weight.

4.3.2 Bayesian framework

Let's consider the following Bayesian framework described in [100, 101]. We define $\underline{y} = (y_i,\ 1 \leq i \leq n)$ as the phase data. We assume that the process is piecewise stationary. Let $\underline{r} = (r_i,\ 1 \leq i \leq n)$ be the configuration of change points in the process $\underline{y}$. Let $\hat{t} = (t_k, k \geq 0, t_0 = 0)$ be the real instant of change we want to detect. The value of r_i is 0 between two changes and 1 at the change instant. Let $\underline{\theta} = (\theta_1, \ldots, \theta_K)$ be the sequence of parameters in the process y, composed of k stationary segments (θ_k is the parameter in the k-th segment of the series $\underline{y}$).

The parameters $\underline{\theta}$ and the sequence of changes $\underline{r}$ are estimated by maximizing the posterior distribution:

$$(\hat{\underline{r}}, \hat{\underline{\theta}}) = \arg\max_{(\underline{r},\underline{\theta})} Pr(\mathcal{R} = \underline{r} \mid Y = \underline{y}; \underline{\theta}) \tag{4.8}$$

$$(\hat{\underline{r}}, \hat{\underline{\theta}}) = \arg\max_{(\underline{r},\underline{\theta})} h(\underline{y} \mid \underline{r}, \underline{\theta}) f(\underline{\theta}) p(\underline{r}) \tag{4.9}$$

where $p(\underline{r})$, the prior law of $\underline{r}$, is given by the binomial law:

$$p(\underline{r}) = \lambda^K (1-\lambda)^{n-K}, \tag{4.10}$$

with λ the probability of a change on $\underline{y}$ and

$$K = \sum_{i=1}^{n} r_i + 1,$$

Then we have :

$$\ln p(\underline{\hat{r}}) = n\ln(1-\lambda) + K\ln\left(\frac{\lambda}{1-\lambda}\right) \quad (4.11)$$

$$= Cst + K\beta \quad (4.12)$$

For a fixed λ the penalty function is a linear penalty of the number of change points with parameter $\beta = \ln\left(\frac{\lambda}{1-\lambda}\right)$.

Let $f(\underline{\theta})$ be the probability to have the sequence of parameters θ for the process $\underline{y}$. We do not have any prior information on $\underline{y}$, so we suppose $f(\theta)$ to follow a uniform distribution (vague prior). In our approach the parameters $\underline{\theta}$ are estimated as $\underline{\hat{\theta}}$. When we take the negative logarithm of Eq 4.12, we define a penalized empirical criterion, where $\underline{r}$ (the number and position of changes) is estimated by minimizing the penalized contrast function defined by:

$$U_y(\underline{\hat{r}}) = V_y(\underline{\hat{r}}, \underline{\hat{\theta}}(\underline{\hat{r}})) - \ln p(\underline{\hat{r}}) \quad (4.13)$$

The parameter λ of the penalization is fixed by the user.

4.3.3 Bayesian change point estimate

At each instant i we have two observations in quadrature of the Cosine and Sine functions I_i, Q_i. The observed phase is processed as follows :

$$y_i = atan2\left(\frac{Q_i}{I_i}\right) \quad (4.14)$$

Let's consider the following model of the two components in quadrature :

$$\tilde{I}_i = \sum_{u=1}^{U} a_u \cos(\alpha_u + \omega_u i) \quad (4.15)$$

$$\tilde{Q}_i = \sum_{u=1}^{U} a_u \sin(\alpha_u + \omega_u i) \quad (4.16)$$

In this context, the model for the observation y_i is given by :

$$y_i = atan2\left(\frac{\tilde{Q}_i + \epsilon_Q(i)}{\tilde{I}_i + \epsilon_I(i)}\right) = \lfloor \rightarrow z_i + \xi_i \rfloor \mod 2\pi \quad (4.17)$$

where $\epsilon_I(i), \epsilon_Q(i)$ are centred Gaussian noises.
The linear circular regression model $\rightarrow z_i = atan2(\tilde{Q}_i/\tilde{I}_i)$ is the weighted

sum of the phases $\{\alpha_u + \omega_u i\}_{u=1,\dots,U}$ in the circular domain and $\{a_u\}_{u=1,\dots,U}$ are the weights [99]. We show that ξ_i is a Von Mises centred noise. Let's consider the following likelihood function for one observation y_i of the linear circular model:

$$f(y_i; \theta_k, \kappa_k) = \frac{1}{2\pi I_0(\kappa_k)} \exp\left(\kappa_k \cos\left(y_i - \rightarrow z_i\right)\right) \tag{4.18}$$

where κ_k is the concentration parameter of the Von Mises distribution in the segment k. I_0 is the modified Bessel function of the first kind and order zero. θ_k is the parameter vector including $\{\alpha_{u,k}, \omega_{u,k}, a_{u,k}\}_{u=1,\dots,U}$.

We can process the spectrum of the linear circular regression in each segment k. The spectrum is given by $\Gamma_k(f) = TF(I_k + jQ_k)$, where TF is the Fourier Transform.

The expression of the norm of the spectrum is:

$$|\Gamma_k(f)| = \sum_{u=1}^{U_k} a_{u,k}\delta(f - \frac{\omega_{u,k}}{2\pi}) + \Psi \tag{4.19}$$

where $\delta(f)$ is the Dirac function, Ψ is a noise and $a_{u,k}$ is the power of the uth reflection. We define $\{\hat{\omega}_{u,k}, \hat{a}_{u,k}\}$ respectively as the set of frequencies and amplitudes of the peaks in the spectrum $\Gamma(f)$. The estimated number of peaks $\hat{U}_k$ is the number of peaks superior to a percentage of the maximum peaks power. This estimate can be defined with the normalized $\{a_{u,k}\}$ as follows :

$$\hat{U}_k \quad = \quad card\left\{\frac{a_{u,k}}{max(\{a_{u,k}\})} > th\right\} \tag{4.20}$$

where th is a threshold defined by the user between $[0, 1]$. The phase $\alpha_{u,k}$ is estimated using the argument of the spectrum:

$$\hat{\alpha}_{u,k} = \angle\left(\Gamma(\frac{\hat{\omega}_{u,k}}{2\pi})\right) \tag{4.21}$$

We show in [99], that the maximum likelihood estimate $\hat{\kappa}_k$ is given by the following equation:

$$\hat{\kappa}_k \quad = \quad A^{-1}(\frac{1}{N}\sum_{i=t_{k-1}}^{t_k} \cos(y_i - \rightarrow \hat{z}_{k,i})) \tag{4.22}$$

with $A(x) = \frac{I_1(x)}{I_0(x)}$ and :

$$\rightarrow \hat{z}_{k,i} \quad = \quad atan2\left(\frac{\sum_{u=1}^{U_k} \hat{a}_{u,k}\ \sin(\hat{\alpha}_{u,k} + \hat{\omega}_{u,k} i)}{\sum_{u=1}^{U_k} \hat{a}_{u,k}\ \cos(\hat{\alpha}_{u,k} + \hat{\omega}_{u,k} i)}\right) \tag{4.23}$$

For n observations and K changes the likelihood of the observations is given by :

$$f(\underline{\hat{r}}, \underline{\hat{\theta}}(\underline{\hat{r}})) = \frac{1}{2\pi} \prod_{k=1}^{K} \frac{1}{I_0(\hat{\kappa}_k)} \prod_{i=t_{k-1}}^{t_k} \exp\left(\hat{\kappa}_k \cos\left(y_i - \hat{y}_{k,i}\right)\right) \tag{4.24}$$

Finally, the contrast function is derived from the log likelihood by the following equation:

$$\begin{aligned} V_y(\underline{\hat{r}}, \underline{\hat{\theta}}(\underline{\hat{r}})) = \sum_{k=1}^{K} \Bigg\{ & L_k \log I_0(\hat{\kappa}_k) \\ & - \hat{\kappa}_k \sum_{i=t_{k-1}}^{t_k} \cos\left(y_i - \rightarrow \hat{z}_{k,i}\right) \Bigg\} \end{aligned} \tag{4.25}$$

Where $L_k = t_k - t_{k-1}$ is the length of segment k.

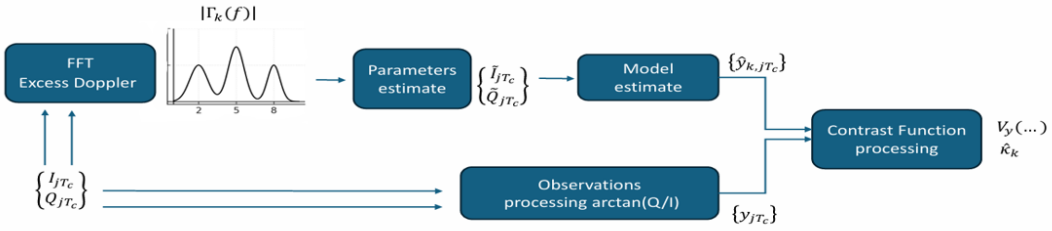

FIGURE 4.1: Flow chart for the estimation of the contrast function

4.4 GNSS-R application

4.4.1 GNSS-R Radar observation

As illustrated in Figure 4.2, when a GNSS signal is reflected from a rough surface, multiple reflections arrive at the GNSS-R receiver. The resulting signal loses coherence because the multiple reflections, that are integrated by the antenna, arrive with different frequencies, phases and amplitudes.

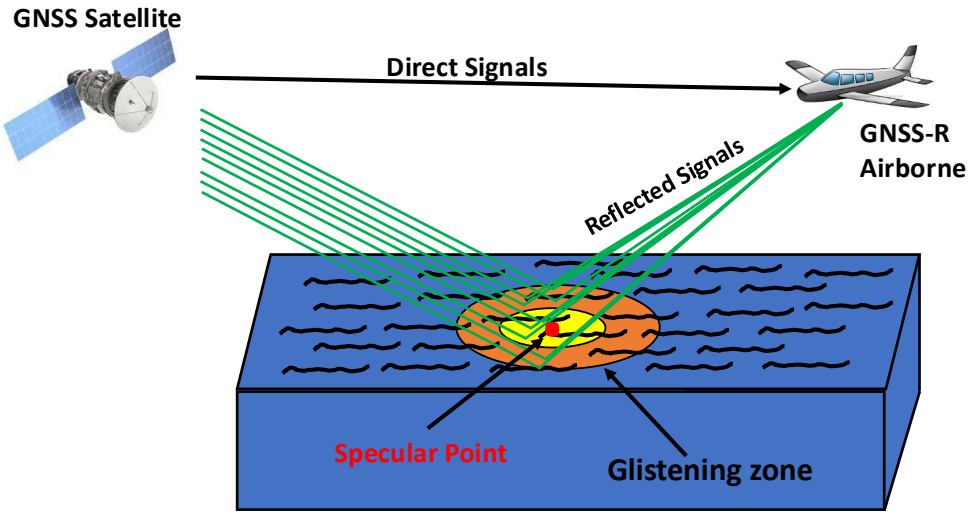

FIGURE 4.2: Multi reflections from rough sea surface

A received GNSS signal is composed of a CDMA (Carrier Division Multiple Access) code and a carrier that are processed by the receiver. Our radar system utilizes two tracking loops for the GNSS signal, each processing both the direct and reflected signals from every satellite. Tracking of the direct signal employs traditional Phase-Locked Loop (PLL) and Delay-Locked Loop (DLL) techniques. Due to the dynamic nature of the airborne GNSS-R receiver, Frequency-Locked Loop (FLL) is also implemented to keep track of the changes in the Doppler frequency along the flight trajectory.

For the reflected signal, we employ an assisted loop that uses information from the direct signal. This assisted loop allow to remove the CDMA code in the signal and a POL (Phase Open Loop) is used to get the observables of the reflected signal phase. In this architecture the reflected signal is multiplied, in a first stage of demodulation, by two local carriers in quadrature. f_1 is the carrier frequency of the direct signal. In a second stage of correlation the signal is integrated over a period T_c defined by the application. We derive in the next section the expressions of I_{jT_c} and Q_{jT_c}.

4.4.2 GNSS-R Phase model

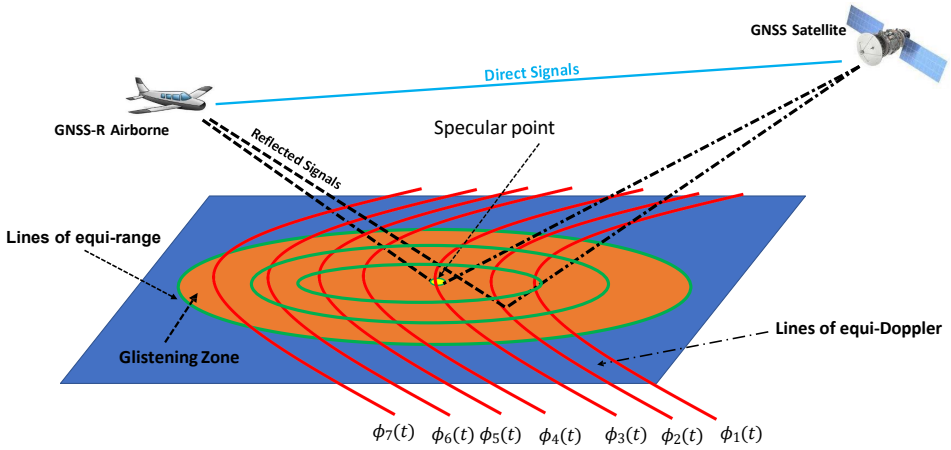

FIGURE 4.3: Equi-Doppler Multi reflections concept in GNSS-R

The expression of the reflected signal composed of the multiple reflections of the signal is given by the following expression and can be physically shown in Figure 4.3:

$$s_r(t) = \sum_{i=1}^{U} a_i \sin(2\pi f_1 t + \phi_i(t)) + \eta(t) \tag{4.26}$$

Where $\eta(t)$ is a Gaussian noise and U the number of reflections. The SNR (Signal to Noise Ratio) of each reflexion is defined by the ratio between a_i and the standard deviation of the noise $\eta(t)$. $\phi_i(t)$ is assumed to contain the difference of phase and carrier between the reflected and direct GNSS signals. According to the flow chart of Figure 4.1 the mathematical expression of the two components in quadrature are given by :

$$I_{jT_c} = \int_{jT_c}^{(j+1)T_c} \sin(2\pi f_1 t) s_r(t) dt \tag{4.27}$$

$$Q_{jT_c} = \int_{jT_c}^{(j+1)T_c} \cos(2\pi f_1 t) s_r(t) dt \tag{4.28}$$

In practice the numerical implementation of the stage of correlation can be assumed to be a low pas filtering process. In this chapter, the double

frequencies of the demodulation stage can be removed and we have the following simplification of expressions 4.27, 4.28 :

$$I_{jT_c} = \sum_{i=1}^{U} \int_{jT_c}^{(j+1)T_c} \frac{a_i}{2} \cos(\phi_i(t))dt + \eta_I \tag{4.29}$$

$$Q_{jT_c} = \sum_{i=1}^{U} \int_{jT_c}^{(j+1)T_c} \frac{a_i}{2} \sin(\phi_i(t))dt + \eta_Q \tag{4.30}$$

with the gaussian noises :

$$\eta_I = \int_{jT_c}^{(j+1)T_c} \sin(2\pi f_1 t)\eta(t)dt \tag{4.31}$$

$$\eta_Q = \int_{jT_c}^{(j+1)T_c} \cos(2\pi f_1 t)\eta(t)dt \tag{4.32}$$

We assume that the phase is a linear function of time during T_c:

$$\phi_i(t) = \alpha_{i0} + \omega_i t$$

with $\omega_i = 2\pi f_{d,i}$. Here, $f_{d,i}$ is the excess Doppler frequency between the direct signal and the i-th reflection. Then we can derive the noiseless part of the two components in quadrature :

$$\tilde{I}_{jT_c} = \frac{T_c}{2} \sum_{i=1}^{U} a_i \cos(\alpha_{0i} + j\omega_i T_c - \frac{\omega_i T_c}{2}) \tag{4.33}$$

$$\tilde{Q}_{jT_c} = \frac{T_c}{2} \sum_{i=1}^{U} a_i \sin(\alpha_{0i} + j\omega_i T_c - \frac{\omega_i T_c}{2}) \tag{4.34}$$

These last expressions show that the observed phase process with I_{jT_c} and Q_{jT_c}, provided by the POL, can be modelled by a linear circular regression defined by $\rightarrow z_i = atan2(\tilde{Q}_{jT_c}/\tilde{I}_{jT_c})$. We report Figure 4.1 the flow chart of the estimation of the contrast function and parameters.

4.5 Experimentation

This section presents the experimental validation of the proposed change detection framework. The methodology is first assessed using synthetic carrier-phase data, where controlled scenarios with known change points allow a

quantitative evaluation of detection accuracy under both single and multiple transition conditions. The analysis is then extended to real GNSS-R measurements, demonstrating the applicability of the proposed approach to real-world reflected carrier-phase data and its ability to reliably detect surface-induced statistical changes.

4.5.1 Analysis of Synthetic Phase Data with a Single Change Point

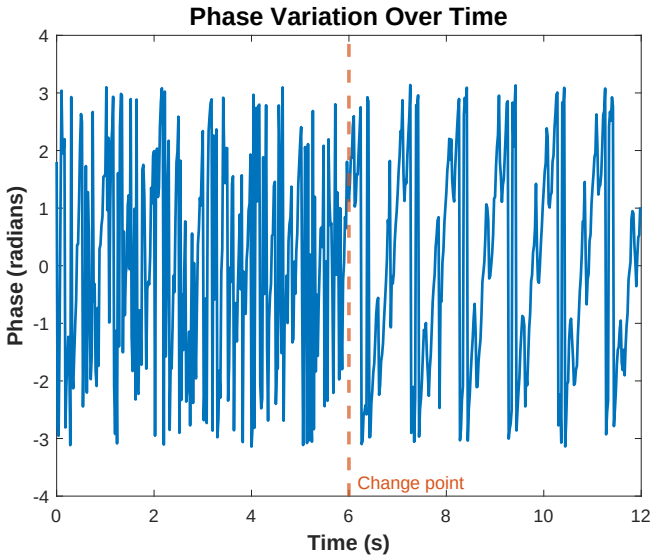

FIGURE 4.4: Phase sequence illustrating the detected change point at 6 s. The first segment (0–6 s) corresponds to the non-coherent region, while the second segment (6–12 s) represents the coherent region. A vertical dashed line marks the detected change location.

Figure 4.4 illustrates the phase sequence used for the analysis, consisting of two consecutive 12-second segments separated by a change point. The first segment exhibits non-coherent behavior, characterized by multiple phase components with low concentration, while the second segment demonstrates coherent phase evolution, indicating a stable scattering condition. The parameter estimates for both segments are summarized in Tables 4.1 and 4.2. In the non-coherent segment, the estimated phase parameters $\hat{\omega}$ vary over a wider range, and the corresponding amplitudes $\hat{A}$ and shape parameters $\hat{\alpha}$ show higher variability, consistent with multiple interfering reflections. The low concentration parameter $\hat{\kappa} = 1.47$ further confirms the absence of phase alignment. Conversely, in the coherent segment, only two dominant phase

components are identified, with relatively stable $\hat{\alpha}$ and $\hat{A}$ values, and a high concentration $\hat{\kappa} = 13.84$, indicating strong phase stability and coherence. These results highlight the method's ability to discriminate between coherent and non-coherent scattering regimes based on the estimated parameters and the detected change point in the phase sequence.

TABLE 4.1: Parameter estimates for Figure 4.4, second segment (coherent from t = 6s to t = 12s).

Parameter	Estimated Values
$\hat{\omega}$	6.28, 31.41
$\hat{\alpha}$	1.07, 1.55
$\hat{A}$ ($\times 10^7$)	10.48, 7.08
$\hat{\kappa}$	13.84

TABLE 4.2: Parameter estimates for Figure 4.4, first segment (non-coherent from t = 0s to t = 6s).

Parameter	Estimated Values
$\hat{\omega}$	37.69, 12.56, 6.28, 25.13
$\hat{\alpha}$	-2.99, 1.45, 1.53, 2.41
$\hat{A}$ ($\times 10^7$)	10.34, 6.09, 5.26, 5.23
$\hat{\kappa}$	1.47

The proposed detection method successfully identifies this change point with high precision, even under challenging conditions where both the noise level and the underlying signal model vary across the dataset.

4.5.2 Assessment on synthetic data with Multiple Change Points

In order to evaluate the proposed BCPD method, we simulated 6 seconds of GNSS signal phase data, consisting of three distinct segments with two changes on y_1 at $t = 2$ seconds and y_2 at $t = 4$ seconds, as shown in Figure 4.6 (a). The first and third segments represent the coherent phase with two reflections, while the second segment represents the non-coherent phase with four reflections. The parameter vectors $\hat{\alpha}$, $\hat{\omega}$, $\hat{A}$, and $\hat{\kappa}$ for the three segments were estimated using the equations provided in Section 4. For the first and last 2 seconds, representing the coherent segments, the parameter estimates are computed in Table 4.3. For the second segment, the parameters estimated for the non-coherent phase are presented in Table 4.4.

Figure 4.5 illustrates the spectrum analysis of excess Doppler in both coherent and non-coherent segments of the synthetic data. Sub-figure 4.5a shows the spectrum for the coherent portions—specefically the first and last two seconds of the first realization—characterized by a dominant spectral peak corresponding to a single strong reflection with relatively low noise, indicating a stable and coherent propagation path. In contrast, sub-figure 4.5b presents the spectrum for the non-coherent segment (the middle two seconds), which displays a broader and more scattered spectral content due to multiple reflections and higher noise, leading to reduced temporal coherence and increased frequency dispersion. This comparison highlights the spectral distinction between coherent and non-coherent behaviors influenced by the underlying propagation conditions.

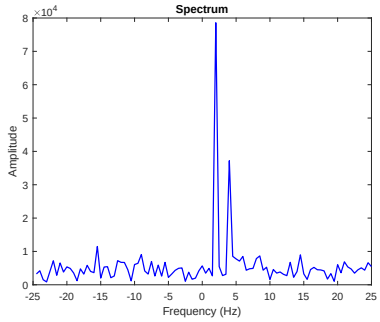

(a) Spectrum for excess Doppler of the coherent part (first and last 2 seconds).

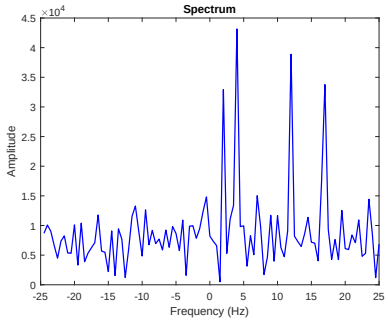

(b) Spectrum for excess Doppler of the non-coherent middle segment (second 2 seconds).

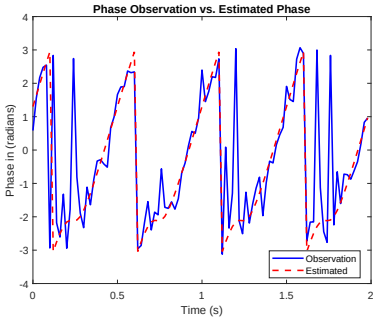

(c) Phase Estimated and Observation for the coherent segments

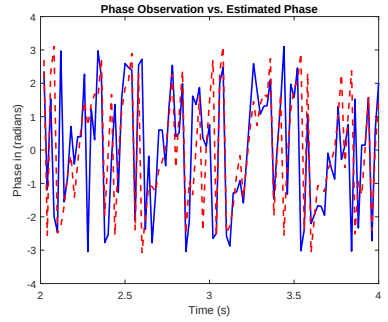

(d) Phase Estimated and Observation for non-coherent segment

FIGURE 4.5: Spectrum analysis of the excess Doppler in coherent and non-coherent segments of the first realization of the synthetic data, along with phase estimation for both segments.

The lower row of Figure 4.5 features the phase estimation results. Subfigure 4.5c depicts the phase estimation and observation for the coherent part,

where the estimated phase is compared with the observed data to evaluate the accuracy of the estimation method. Similarly, subfigure 4.5d shows the phase estimation and observation for the non-coherent segment, highlighting the differences in phase behavior between the two segments. Together, these figures provide a comprehensive view of both the spectral characteristics and the phase estimation performance for coherent and non-coherent segments of the data, aiding in understanding the signal behavior under different conditions.

TABLE 4.3: Parameter estimates for Figure 4.6(a), first and last segments (coherent).

Parameter	Estimated Values
$\hat{\omega}$	12.56, 25.13
$\hat{\alpha}$	1.14, 1.35
$\hat{A}$ ($\times 10^7$)	8.18, 4.21
$\hat{\kappa}$	3.82

TABLE 4.4: Parameter estimates for Figure 4.6(a), second segment (non-coherent).

Parameter	Estimated Values
$\hat{\omega}$	25.13, 75.39, 12.56, 106.81
$\hat{\alpha}$	1.49, 2.86, -3.10, -2.94
$\hat{A}$ ($\times 10^7$)	4.63, 3.70, 3.61, 3.43
$\hat{\kappa}$	1.71

By minimizing Eq 4.25, the change points, $\hat{r}$, were precisely detected at $t = 2$ and $t = 4$ seconds. The BCPD, utilizing a multiple search approach, is implemented as outlined in [100].

4.5.3 Real GNSS-R measurement

The experimental data for this study were discussed in 3.4.2.

4.5.3.1 Contrast Function Evaluation

The Contrast Function defined in Eq. 4.25 is evaluated on the considered real GNSS-R measurement to quantify statistical changes in the reflected carrier-phase signal. In this experiment, the Contrast Function is computed using the estimated model parameters obtained from successive segments of a part of real data record corresponding to the phase time series shown in Figure 4.7. The resulting Contrast Function evolution is displayed in Figure 4.8.

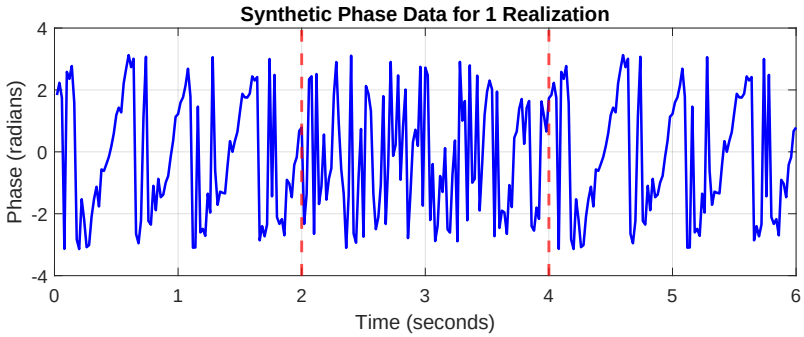

(a) Change Detection results for one realization of synthetic phase data

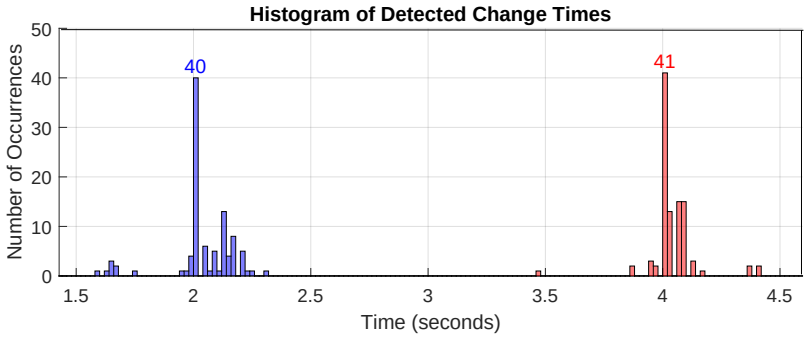

(b) Histogram of the change detection method using Euclidian Distance (ED): Distribution of detected changes over 100 realization.

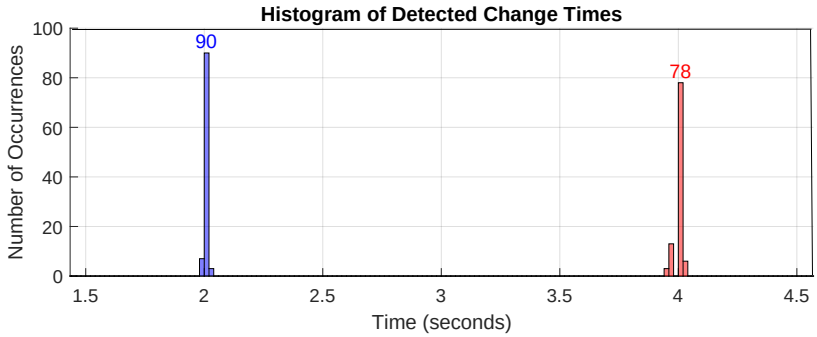

(c) Histogram of our BCPD method's results: Distribution of detected changes over 100 realization.

FIGURE 4.6: Comparison of change detection and probability of good detection for synthetic data: Evaluating the performance of the detection methods.

The detected change point is obtained by minimizing the Contrast Function, which identifies the time instant at which a significant transition in the phase statistics occurs. The result shows that the change is detected with high precision and accurately coincides with the transition between the two surface types observed in the phase data.

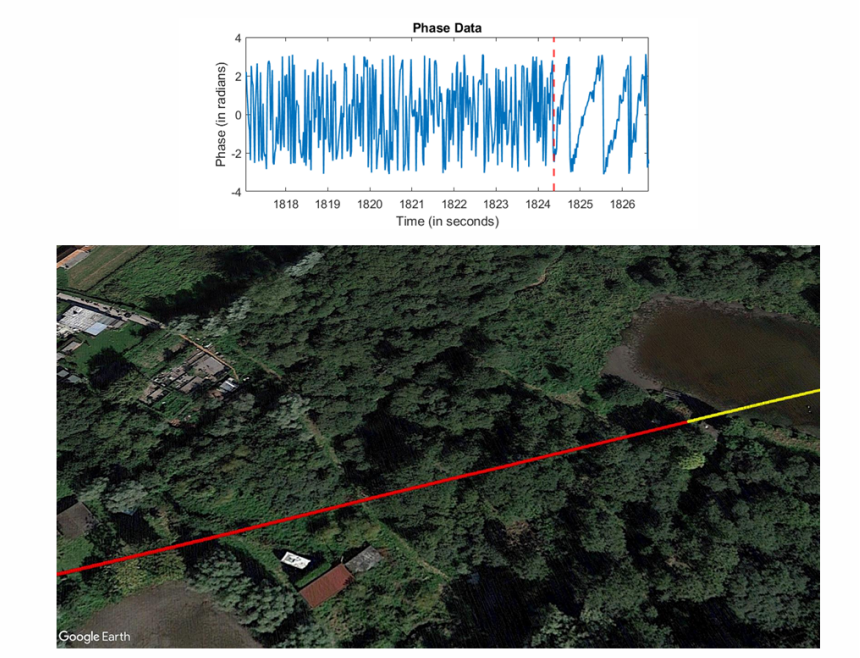

FIGURE 4.7: 10 seconds of phase data from the reflected GNSS signal of GPS satellite PRN 5, showing a rough land surface (red) in the first segment and a smooth lake surface (yellow) in the second segment, with the detected change accurately identified.

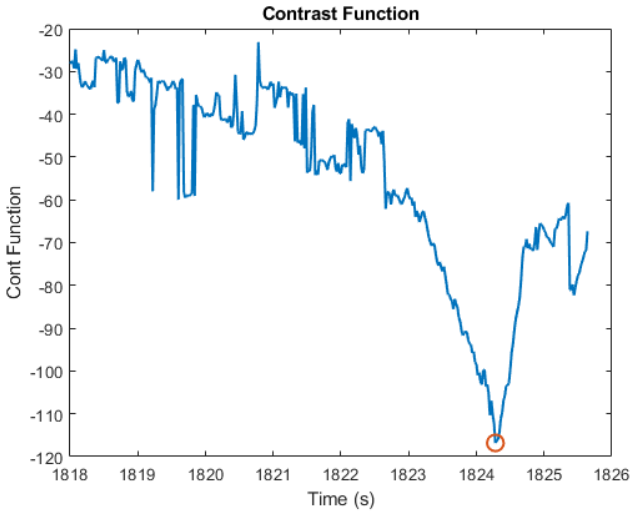

FIGURE 4.8: Computed Contrast Function corresponding to the reflected carrier-phase signal shown in Figure 4.7. The minimum value of the Contrast Function, indicated by a small red circle, marks the detected change point.

TABLE 4.5: Parameter estimates for Figure 4.7, first segment (non-coherent).

Parameter	Estimated Values
$\hat{\omega}$	26.81, 305.59, 58.95, 243.73, 2.71, 66.40
$\hat{\alpha}$	1.64, 2.80, 0.16, 1.94, 1.03, 1.38
$\hat{A}$ $(\times 10^4)$	8.02, 7.83, 7.34, 6.71, 6.68, 6.58
$\hat{\kappa}$	0.52

The parameter estimates for the first segment in Figure 4.7 correspond to the non-coherent segment. The estimated values for $\hat{\omega}$, $\hat{\alpha}$, $\hat{A}$, and $\hat{\kappa}$ are presented in 4.5.

TABLE 4.6: Parameter estimates for Figure 4.7, second segment (coherent).

Parameter	Estimated Values
$\hat{\omega}$	9.23, 13.94, 17.57
$\hat{\alpha}$	0.41, 1.84, -0.54
$\hat{A}$ $(\times 10^4)$	25.72, 16.61, 7.54
$\hat{\kappa}$	3.04

While for the second segment of Figure 4.7, which represents the coherent segment, the parameter estimates are provided in 4.6. These estimates reflect the behavior of the reflected signal in a coherent environment, where higher

$\hat{\kappa}$ values indicate better coherence. The estimated values for $\hat{\omega}$, $\hat{\alpha}$, and $\hat{A}$ emphasize the distinguishing features between the non-coherent and coherent segments.

4.5.3.2 Real Data Results: Lake–Land Transition

Figure 4.9 shows 15 seconds of phase data from the reflected GNSS signal of the GPS satelite PRN 5, split into two segments. The first segment corresponds to a lake, representing a very smooth surface, while the second segment pertains to land, which is considered a rougher surface. Similarly, Figure 4.7 presents 10 seconds of phase data from the reflected GNSS signal of GPS satellite PRN 5, also divided into two segments: the first represents land, and the second corresponds to a smooth lake surface. The parameter estimates for the first segment in Figure 4.9 correspond to the coherent segment. The estimated values for $\hat{\omega}$, $\hat{\alpha}$, $\hat{A}$, and $\hat{\kappa}$ are presented in 4.7.

TABLE 4.7: Parameter estimates for Figure 4.9, first segment (coherent).

Parameter	Estimated Values
$\hat{\omega}$	303.99, 300.14, 297.04
$\hat{\alpha}$	-1.24, -1.14, -1.48
$\hat{A}$ ($\times 10^5$)	2.67, 1.61, 0.89
$\hat{\kappa}$	3.84

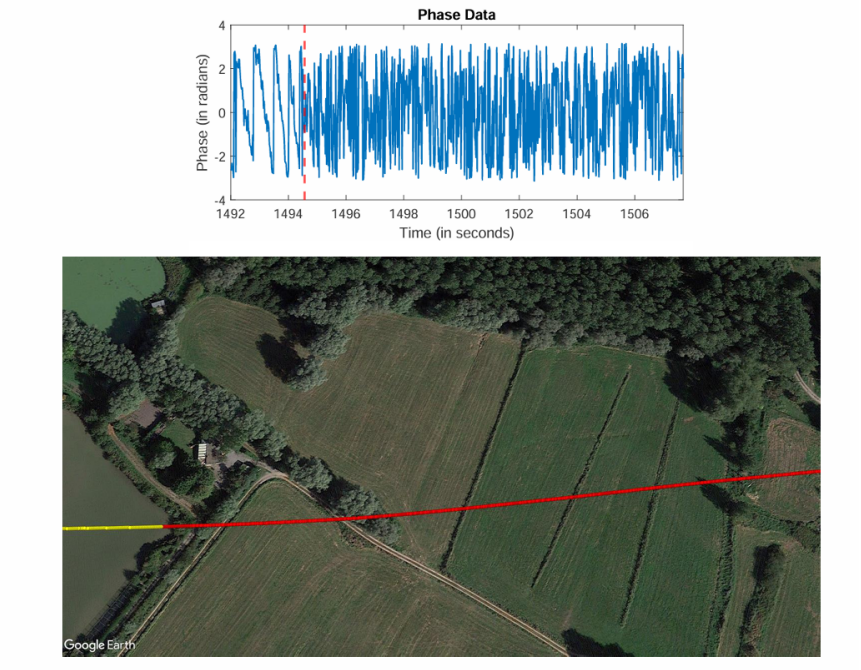

FIGURE 4.9: 15 seconds of phase data from the reflected GNSS signal of GPS satellite PRN 5, showing a smooth lake surface (yellow) in the first segment and a rough land surface (red) in the second segment, with the detected change accurately identified.

TABLE 4.8: Parameter estimates for Figure 4.9, second segment (non-coherent).

Parameter	Estimated Values
$\hat{\omega}$	304.59, 295.09, 2.45, 0.12, 291.93, 6.11, 305.16, 284.11
$\hat{\alpha}$	0.96, -2.43, -1.12, 1.62, 0.31, 2.12, -1.58, 1.43
$\hat{A}$ ($\times 10^5$)	1.46, 1.41, 1.34, 1.31, 1.25, 1.24, 1.22, 1.19
$\hat{\kappa}$	0.49

The parameter estimates for the second segment in Figure 4.9 correspond to the non-coherent phase. The estimated values for $\hat{\omega}$, $\hat{\alpha}$, $\hat{A}$, and $\hat{\kappa}$ are given in Table 4.8.

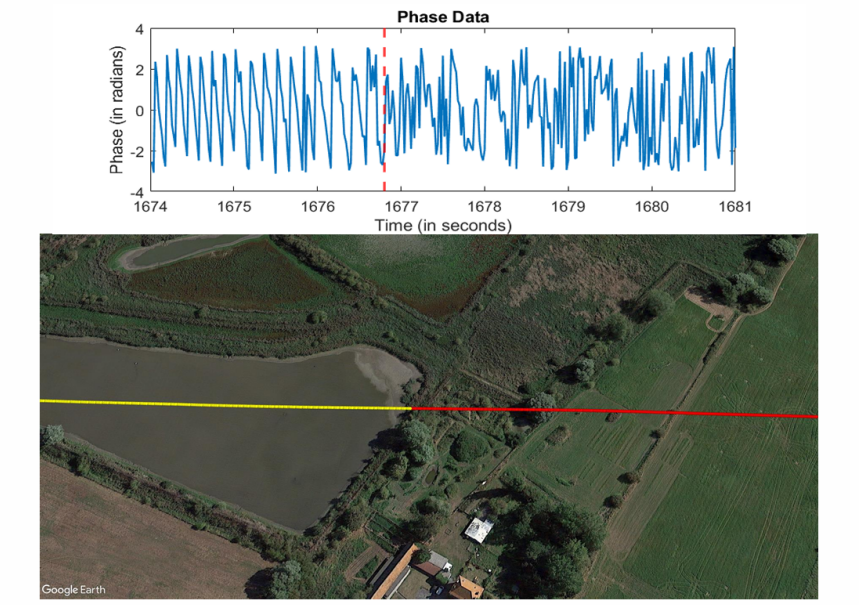

FIGURE 4.10: 7 seconds of phase data from the reflected GNSS signal of GPS satellite PRN 5, showing a smooth lake surface (yellow) in the first segment and a rough land surface (red) in the second segment, with the detected change accurately identified.

TABLE 4.9: Parameter estimates for Figure 4.10, first segment (coherent).

Parameter	Estimated Values
$\hat{\omega}$	272.76, 262.34
$\hat{\alpha}$	2.25, -0.63
$\hat{A}$ $(\times 10^5)$	2.36, 0.47
$\hat{\kappa}$	3.74

TABLE 4.10: Parameter estimates for Figure 4.10, second segment (non-coherent).

Parameter	Estimated Values
$\hat{\omega}$	27.00, 25.19, 17.49, 44.11, 297.54, 283.44, 290.06
$\hat{\alpha}$	-1.99, -1.98, 0.75, 0.25, -0.59, 0.74, -0.35
$\hat{A}$ $(\times 10^4)$	6.43, 6.14, 6.04, 6.04, 5.65, 5.60, 5.57
$\hat{\kappa}$	0.79

The parameter estimates for the first segment in Figure 4.10 corresponds to the coherent segment. The estimated values for $\hat{\omega}$, $\hat{\alpha}$, $\hat{A}$, and $\hat{\kappa}$ are shown in 4.9. Finally, the parameter estimates for the second segment in Figure 4.10 corresponds to the non-coherent phase. The estimated values for $\hat{\omega}$, $\hat{\alpha}$, $\hat{A}$, and $\hat{\kappa}$ are presented in 4.10.

4.5.3.3 Real Data Results: Rough Terrain–Stadium Transition

To further verify that the proposed method remains reliable when transitioning from a rough surface to a less smooth but still structured surface, the following experiment considers a flat stadium as the reference coherent environment. Figure 4.11 presents 7.5 seconds of reflected GNSS carrier-phase data from GPS satellite PRN 5, where the first segment corresponds to a rough surface (red) and the second segment corresponds to a smooth surface represented by a flat stadium (yellow). The detected change point accurately marks the transition between these two reflection regimes.

The parameter estimates for the first segment of Figure 4.11, which corresponds to the rough, non-coherent surface, are summarized in Table 4.11. The relatively low value of $\hat{\kappa}$ indicates weak phase coherence, as expected in the presence of surface roughness. The associated estimates of $\hat{\omega}$, $\hat{\alpha}$, and $\hat{A}$ further reflect the unstructured nature of the reflected signal in this segment.

In contrast, the parameter estimates for the second segment of Figure 4.11, corresponding to the flat stadium surface, are reported in Table 4.12. The higher $\hat{\kappa}$ value reveals a clear increase in phase coherence, consistent with a smoother and more specular reflecting surface. The estimated values of $\hat{\omega}$, $\hat{\alpha}$, and $\hat{A}$ highlight the distinct statistical behavior of the reflected signal compared to the rough-surface segment. Altogether, these results demonstrate that the proposed method effectively captures transitions from non-coherent to coherent reflection conditions, even when the smooth surface is not an ideal natural reflector such as a lake.

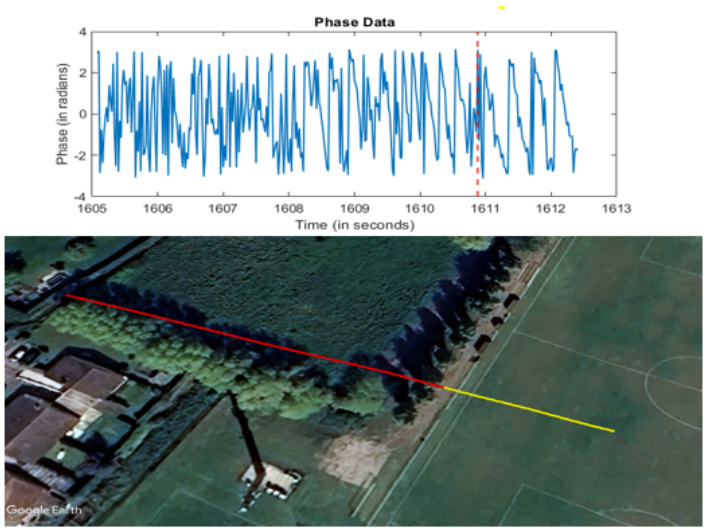

FIGURE 4.11: 7.5 seconds of phase data from the reflected GNSS signal of GPS satellite PRN 5, showing a rough surface(red) in the first segment and a smooth surface represented by flat stadium (yellow) in the second segment, with the detected change accurately identified.

TABLE 4.11: Parameter estimates for Figure 4.11, first segment (non-coherent).

Parameter	Estimated Values
$\hat{\omega}$	298.96, 294.21, 280.55, 296.20, 23.34, 302.77
$\hat{\alpha}$	$-0.81, -2.14, -0.12, 2.68, 2.98, -2.11$
$\hat{A}$ $(\times 10^5)$	1.03, 0.90, 0.85, 0.83, 0.72, 0.71
$\hat{\kappa}$	0.76

TABLE 4.12: Parameter estimates for Figure 4.11, second segment (semi-coherent).

Parameter	Estimated Values
$\hat{\omega}$	286.07, 281.19, 291.44, 271.24
$\hat{\alpha}$	0.98, 2.45, 2.86, 2.34
$\hat{A}$ $(\times 10^4)$	9.98, 8.24, 7.53, 6.82
$\hat{\kappa}$	2.09

4.6 Discussion

This chapter formulates a Bayesian offline multiple change point detection framework tailored to GNSS-R reflected carrier-phase time series, modeled

as a piecewise-stationary multiple linear circular regression corrupted by centered Von Mises noise. A penalized contrast function is derived from the posterior distribution, where the prior on the change configuration yields a linear penalty in the number of change points controlled by λ. To avoid ambiguity issues of circular regression parameter estimation in the time domain, the model parameters $(\hat{\omega}_{u,k}, \hat{a}_{u,k}, \hat{\alpha}_{u,k})$ are estimated in the spectral domain from the quadrature components (I, Q), and the segment coherence is quantified by the concentration parameter $\hat{\kappa}_k$. Experiments on synthetic data demonstrate accurate localization of both single and multiple transitions between coherent and non-coherent regimes, with clear separation in estimated $\hat{\kappa}$ and spectral structure. Validation on real airborne GNSS-R measurements (e.g., lake–land and rough-terrain–stadium transitions) shows that minimizing the proposed contrast function detects surface-induced statistical changes with high precision and provides physically interpretable parameter variations, while Euclidean-distance spectral detection is used as a reference benchmark.

General Conclusion

This thesis has explored the use of carrier-phase measurements in GNSS-R for the purpose of robust surface change detection, with a particular focus on detecting phase coherence variations using statistical and Bayesian methods adapted to circular data. The motivation stemmed from the observation that most existing GNSS-R methodologies rely on signal amplitude and delay observables, while largely overlooking the carrier phase due to its circular nature and the associated processing challenges. However, carrier phase signals encode fine-grained information about surface changes, and thus offer a powerful yet underutilized opportunity for high-resolution environmental monitoring and geophysical applications.

The contributions of this work are both theoretical and practical. On the theoretical side, the thesis established a formal framework for change point detection in circular phase data. A thorough review and adaptation of circular statistical tests such as the Rayleigh Test was undertaken to evaluate its effectiveness in identifying transitions in phase coherence. This test was integrated within a unified detection and localization strategy aimed at distinguishing changes in surface type, as evidenced by alterations in the statistical properties of reflected GNSS signals.

In parallel, a significant methodological advancement was achieved by developing an offline Bayesian Change-Point Detection (BCPD) framework tailored specifically for phase-based GNSS-R signals. By modeling the phase noise with the Von Mises distribution, the method captured th e circularity of the phase domain in a statistically rigorous manner. Change points were identified through the minimization of a contrast function that incorporated spectral features, including excess Doppler shifts. The Bayesian formulation provided a principled mechanism for segmenting the phase data into statistically homogeneous intervals, enabling accurate change detection while accounting for uncertainty in both the parameters and segmentation.

These methods were first evaluated on synthetic datasets, allowing precise control over the underlying signal and noise conditions. The results confirmed the sensitivity and robustness of the proposed approaches in detecting subtle changes in the phase structure. More importantly, the techniques

were then applied to real GNSS-R measurements, where they successfully identified phase transitions associated with changes in the reflective surface. This empirical validation not only underscores the feasibility of carrier-phase analysis in real world GNSS-R systems but also highlights the practical relevance of the proposed methodology across a range of environmental monitoring scenarios.

From a broader perspective, the thesis bridges a crucial methodological gap by integrating tools from directional statistics and Bayesian inference into GNSS-R signal processing. This fusion of domains enabled the development of detection algorithms that are not only mathematically sound but also highly applicable to modern GNSS-R systems. The work contributes to advancing the state-of-the-art in change detection by offering novel solutions tailored for circular data—solutions.

In summary, this thesis presents a comprehensive approach to carrier-phase-based change detection in GNSS-R, combining advanced statistical modeling with practical implementation and validation. By rigorously addressing the challenges posed by the circular nature of phase data, the proposed methods lay a strong foundation for the future development of high-resolution, passive remote sensing tools using GNSS-R. The insights and methodologies presented herein are expected to have an lasting impact on both the scientific understanding and operational capabilities of GNSS-based Earth observation.

Bibliography

[1] Shuanggen Jin, Estel Cardellach, and Feiqin Xie. *GNSS Remote Sensing: Theory, Methods and Applications*. Ed. by Shuanggen Jin. Vol. 16. Dordrecht: Springer, 2014. ISBN: 978-94-007-7482-7. DOI: 10.1007/978-94-007-7482-7. URL: https://link.springer.com/book/10.1007/978-94-007-7482-7.

[2] Manuel Martín-Neira. "A Passive Reflectometry and Interferometry System (PARIS): Application to Ocean Altimetry". In: *ESA Journal* 17.4 (1993), pp. 331–355.

[3] Institut de Ciències de l'Espai. *GOLD-RTR MINING Web Server for GNSS-R Experimental Data and Related Information*. http://www.ice.csic.es/research/gold-rtr-mining. Accessed online.

[4] Estel Cardellach et al. "GNSS-R Ground-Based and Airborne Campaigns for Ocean, Land, Ice, and Snow Techniques: Application to the GOLD-RTR Data Sets". In: *Radio Science* 46.6 (2011), pp. 1–16. DOI: 10.1029/2011RS004683.

[5] S. T. Lowe et al. "First Spaceborne Observation of an Earth-Reflected GPS Signal". In: *Radio Science* 37.1 (2002), pp. 1–28. DOI: 10.1029/2000RS002539.

[6] S. Gleason et al. "Detection and Processing of Bistatically Reflected GPS Signals from Low Earth Orbit for the Purpose of Ocean Remote Sensing". In: *IEEE Transactions on Geoscience and Remote Sensing* 43.6 (2005), pp. 1229–1241. DOI: 10.1109/TGRS.2005.845307.

[7] Scott Gleason. "Remote Sensing of Ocean, Ice and Land Surfaces Using Bistatically Scattered GNSS Signals from Low Earth Orbit". PhD thesis. University of Surrey, 2006. URL: https://cygnss.engin.umich.edu/wp-content/uploads/sites/534/2021/06/Gleason_Thesis_GNSS.pdf.

[8] Scott Gleason. "Towards Sea Ice Remote Sensing with Space Detected GPS Signals: Demonstration of Technical Feasibility and Initial Consistency Check Using Low Resolution Sea Ice Information". In: *Remote Sensing* 2.8 (2010), pp. 2017–2039. DOI: 10.3390/rs2082017.

[9] Kristine M. Larson et al. "Use of GPS Receivers as a Soil Moisture Network for Water Cycle Studies". In: *Geophysical Research Letters* 35.24 (2008), p. L24405. DOI: 10.1029/2008GL036013.

[10] Alejandro Egido. "GNSS Reflectometry for Land Remote Sensing Applications". PhD thesis. Polytechnic University of Catalonia, 2013. URL: https://www.tdx.cat/handle/10803/129090.

[11] Kristine M. Larson et al. "Using GPS Multipath to Measure Soil Moisture Fluctuations: Initial Results". In: *GPS Solutions* 12.3 (2008), pp. 173–177. DOI: 10.1007/s10291-007-0076-6.

[12] Kristine M Larson et al. "GPS multipath and its relation to near-surface soil moisture content". In: *IEEE Journal of Selected Topics in Applied Earth Observations and Remote Sensing* 3.1 (2009), pp. 91–99.

[13] Yuan Hu et al. "An SVM-Based Snow Detection Algorithm for GNSS-R Snow Depth Retrievals". In: *IEEE Journal of Selected Topics in Applied Earth Observations and Remote Sensing* 15 (2022), pp. 6046–6052. DOI: 10.1109/JSTARS.2022.3188561.

[14] Rui Ding et al. "A Study of GNSS-IR Soil Moisture Inversion Algorithms Integrating Robust Estimation with Machine Learning". In: *Sustainability* 15.8 (2023), p. 6919. DOI: 10.3390/su15086919.

[15] Johan S. Löfgren and Rüdiger Haas. "Sea Level Measurements Using Multi-Frequency GPS and GLONASS Observations". In: *EURASIP Journal on Advances in Signal Processing* 2014.1 (2014), p. 50. DOI: 10.1186/1687-6180-2014-50.

[16] M. Caparrini, L. Ruffini, and G. Ruffini. "PARFAIT: GNSS-R Coastal Altimetry". In: *arXiv preprint physics/0311052* (2003).

[17] Yang Wang and Y. Jade Morton. "River Slope Observation from Spaceborne GNSS-R Carrier Phase Measurements: A Case Study". In: *IEEE Geoscience and Remote Sensing Letters* 19 (2021), pp. 1–5. DOI: 10.1109/LGRS.2021.3095360.

[18] Hatchouelou Kant Williams Kouassi, Georges Stienne, and Serge Reboul. "Theoretical Study of the Carrier-Phase GNSS-R Altimetry Accuracy". In: *2021 IEEE Specialist Meeting on Reflectometry using GNSS and Other Signals of Opportunity (GNSS+R)*. 2021, pp. 13–16. DOI: 10.1109/GNSSR53121.2021.9561834.

[19] Tianhe Xu et al. "High-Precision GNSS-R Altimetry Based on Carrier Phase Measurement Combination". In: *EGU General Assembly Conference Abstracts*. 2023, EGU–4062.

[20] Jin Xing et al. "Carrier Phase Continuity Monitoring and Correction in GNSS-R Sea Surface Altimetry Systems". In: *IEEE Sensors Letters* 9.1 (2024), pp. 1–4.

[21] Jin Xing et al. "An Adaptive Fusion Algorithm for Coastal Sea Altimetry Based on Dual-Frequency BeiDou-R Carrier Phase". In: *PLOS ONE* 19.5 (2024), e0302305. DOI: 10.1371/journal.pone.0302305.

[22] Jin Xing et al. "Prediction of carrier phase in GNSS-R altimetry application using grey model at B1/B3 frequencies". In: *Fourth International Conference on Geology, Mapping, and Remote Sensing (ICGMRS 2023)*. Vol. 12978. SPIE. 2024, pp. 513–519.

[23] Jérôme Leclère, René Landry, and Cyril Botteron. "Comparison of L1 and L5 Bands GNSS Signals Acquisition". In: *Sensors* 18.9 (2018), p. 2779. DOI: 10.3390/s18092779.

[24] Christophe Macabiau et al. "GPS L5 Receiver Implementation Issues". In: *Proceedings of the 16th International Technical Meeting of the Satellite Division of the Institute of Navigation (ION GPS/GNSS 2003)*. 2003, pp. 153–164.

[25] Sarah El Hajj Chehade et al. "Change Point Detection in Radar Reflectivity Measurements Contaminated by Speckle Noise". In: *IEEE Journal of Selected Topics in Applied Earth Observations and Remote Sensing* 17 (2024), pp. 11208–11218. DOI: 10.1109/JSTARS.2024.3410039.

[26] Georges Stienne et al. "A Multi-Temporal Multi-Sensor Circular Fusion Filter". In: *Information Fusion* 18 (2014), pp. 86–100. DOI: 10.1016/j.inffus.2013.05.012.

[27] Jean-Christophe Kucwaj et al. "Circular Regression Applied to GNSS-R Phase Altimetry". In: *Remote Sensing* 9.7 (2017), p. 651. DOI: 10.3390/rs9070651.

[28] Jie Chen and Arjun K. Gupta. *Parametric Statistical Change Point Analysis*. Vol. 192. Boston: Birkhäuser, 2000. DOI: 10.1007/978-1-4757-3131-6.

[29] Sylvain Arlot, Alain Celisse, and Zaid Harchaoui. "A Kernel Multiple Change-Point Algorithm via Model Selection". In: *arXiv preprint arXiv:1202.3878* (2012). URL: https://arxiv.org/abs/1202.3878.

[30] Rebecca Killick, Paul Fearnhead, and Idris A. Eckley. "Optimal Detection of Changepoints with a Linear Computational Cost". In: *Journal of the American Statistical Association* 107.500 (2012), pp. 1590–1598. DOI: 10.1080/01621459.2012.737745.

[31] Jaromír Antoch and Dušan Legát. "Application of MCMC to Change Point Detection". In: *Applications of Mathematics* 53 (2008), pp. 281–296. DOI: 10.1007/s10492-008-0017-2.

[32] Charles Truong, Laurent Oudre, and Nicolas Vayatis. "Selective Review of Offline Change Point Detection Methods". In: *Signal Processing* 167 (2020), p. 107299. DOI: 10.1016/j.sigpro.2019.107299.

[33] Eamonn Keogh et al. "An Online Algorithm for Segmenting Time Series". In: *Proceedings of the 2001 IEEE International Conference on Data Mining*. IEEE, 2001, pp. 289–296. DOI: 10.1109/ICDM.2001.989531.

[34] Eamonn Keogh et al. "Segmenting Time Series: A Survey and Novel Approach". In: *Data Mining in Time Series Databases*. Vol. 57. World Scientific, 2004, pp. 1–22.

[35] Julia Prexl, Sudipan Saha, and Xiao Xiang Zhu. "Mitigating Spatial and Spectral Differences for Change Detection Using Super-Resolution and Unsupervised Learning". In: *Proceedings of the 2021 IEEE International Geoscience and Remote Sensing Symposium (IGARSS)*. IEEE, 2021, pp. 3113–3116.

[36] T. Zhu et al. "FTA-Net: Frequency-Temporal-Aware Network for Remote Sensing Change Detection". In: *IEEE Journal of Selected Topics in Applied Earth Observations and Remote Sensing* 18 (2025), pp. 3448–3460. DOI: 10.1109/JSTARS.2025.3525595.

[37] Tao Lei et al. "Difference Enhancement and Spatial–Spectral Nonlocal Network for Change Detection in VHR Remote Sensing Images". In: *IEEE Transactions on Geoscience and Remote Sensing* 60 (2021), pp. 1–13. DOI: 10.1109/TGRS.2021.3097691.

[38] Lorenzo Bruzzone and Diego F. Prieto. "Automatic Analysis of the Difference Image for Unsupervised Change Detection". In: *IEEE Transactions on Geoscience and Remote Sensing* 38.3 (2000), pp. 1171–1182. DOI: 10.1109/36.843009.

[39] Michele Volpi, Gustau Camps-Valls, and Devis Tuia. "Spectral Alignment of Multi-Temporal Cross-Sensor Images with Automated Kernel Canonical Correlation Analysis". In: *ISPRS Journal of Photogrammetry and Remote Sensing* 107 (2015), pp. 50–63. DOI: 10.1016/j.isprsjprs.2015.02.002.

[40] Jin Chen et al. "Land-Use/Land-Cover Change Detection Using Improved Change-Vector Analysis". In: *Photogrammetric Engineering and Remote Sensing* 69.4 (2003), pp. 369–379. DOI: 10.14358/PERS.69.4.369.

[41] Allan Aasbjerg Nielsen, Knut Conradsen, and James J. Simpson. "Multivariate Alteration Detection (MAD) and MAF Postprocessing in Multispectral, Bitemporal Image Data: New Approaches to Change Detection Studies". In: *Remote Sensing of Environment* 64.1 (1998), pp. 1–19. DOI: 10.1016/S0034-4257(97)00162-4.

[42] Peijun Du et al. "Fusion of Difference Images for Change Detection over Urban Areas". In: *IEEE Journal of Selected Topics in Applied Earth Observations and Remote Sensing* 5.4 (2012), pp. 1076–1086. DOI: 10.1109/JSTARS.2012.2200879.

[43] Xiaoxia Wen and Xiaojun Yang. "Change Detection from Remote Sensing Imageries Using Spectral Change Vector Analysis". In: *Asia-Pacific Conference on Information Processing*. Vol. 2. 2009, pp. 189–192.

[44] Osmar Abílio de Carvalho et al. "Spectral Change Detection". In: *2007 IEEE International Geoscience and Remote Sensing Symposium*. IEEE, 2007, pp. 1935–1938.

[45] Roberto Todeschini, Davide Ballabio, and Viviana Consonni. "Distances and Other Dissimilarity Measures in Chemometrics". In: *Encyclopedia of Analytical Chemistry*. John Wiley & Sons, 2015, pp. 1–34. DOI: 10.1002/9780470027318.a9438.

[46] E. S. Page. "Continuous Inspection Schemes". In: *Biometrika* 41.1/2 (1954), pp. 100–115. DOI: 10.1093/biomet/41.1-2.100.

[47] Gary Lorden. "Procedures for Reacting to a Change in Distribution". In: *The Annals of Mathematical Statistics* 42.6 (1971), pp. 1897–1908. DOI: 10.1214/aoms/1177693055.

[48] Daniel Barry and J. A. Hartigan. "A Bayesian Analysis for Change Point Problems". In: *Journal of the American Statistical Association* 88.421 (1993), pp. 309–319. DOI: 10.1080/01621459.1993.10594323.

[49] Paul Fearnhead and Zhen Liu. "On-Line Inference for Multiple Change-point Problems". In: *Journal of the Royal Statistical Society: Series B (Statistical Methodology)* 69.4 (2007), pp. 589–605. DOI: 10.1111/j.1467-9868.2007.00601.x.

[50] Jeremias Knoblauch, Jack E. Jewson, and Theodoros Damoulas. "Doubly Robust Bayesian Inference for Non-Stationary Streaming Data with Beta-Divergences". In: *Advances in Neural Information Processing Systems*. Vol. 31. 2018.

[51] Yi-Ching Yao. "Estimating the Number of Change-Points via Schwarz' Criterion". In: *Statistics and Probability Letters* 6.3 (1988), pp. 181–189. DOI: 10.1016/0167-7152(88)90118-6.

[52] Nancy R. Zhang and David O. Siegmund. "A Modified Bayes Information Criterion with Applications to the Analysis of Comparative Genomic Hybridization Data". In: *Biometrics* 63.1 (2007), pp. 22–32. DOI: 10.1111/j.1541-0420.2006.00662.x.

[53] Samaneh Aminikhanghahi and Diane J. Cook. "A Survey of Methods for Time Series Change Point Detection". In: *Knowledge and Information Systems* 51.2 (2017), pp. 339–367. DOI: 10.1007/s10115-016-0987-z.

[54] Nicholas I. Fisher. *Statistical Analysis of Circular Data*. Cambridge: Cambridge University Press, 1995. DOI: 10.1017/CBO9780511564345.

[55] S Rao Jammalamadaka and Ambar Sengupta. *Topics in circular statistics*. Vol. 5. world scientific, 2001.

[56] Frank J. Jr. Massey. "The Kolmogorov–Smirnov Test for Goodness of Fit". In: *Journal of the American Statistical Association* 46.253 (1951), pp. 68–78. DOI: 10.1080/01621459.1951.10500769.

[57] N. H. Kuiper. "Tests Concerning Random Points on a Circle". In: *Proceedings of the Koninklijke Nederlandse Akademie van Wetenschappen, Series A*. Vol. 63. 1960, pp. 38–47.

[58] G. S. Watson. "Goodness-of-Fit Tests on a Circle". In: *Biometrika* 48.1/2 (1961), pp. 109–114. DOI: 10.1093/biomet/48.1-2.109.

[59] J. S. Rao. "Some Tests Based on Arc-Lengths for the Circle". In: *Sankhyā: The Indian Journal of Statistics, Series B* 38 (1976), pp. 329–338.

[60] Edward D. Rothman. "Tests for Uniformity of a Circular Distribution". In: *Sankhyā: The Indian Journal of Statistics, Series A* 31.1 (1969), pp. 23–31.

[61] Kanti V. Mardia and Peter E. Jupp. *Directional Statistics*. John Wiley & Sons, 2009.

[62] G. K. Bhattacharyya and Richard A. Johnson. "On Hodges's Bivariate Sign Test and a Test for Uniformity of a Circular Distribution". In: *Biometrika* 56.2 (1969), pp. 446–449. DOI: 10.1093/biomet/56.2.446.

[63] C. Roesler et al. "Coherent GPS Reflections over Ocean Surface". In: *IGARSS 2020–2020 IEEE International Geoscience and Remote Sensing Symposium*. IEEE, 2020, pp. 6218–6221.

[64] J. Zhang et al. "Mapping Surface Water Extents Using High-Rate Coherent Spaceborne GNSS-R Measurements". In: *IEEE Transactions on Geoscience and Remote Sensing* 60 (2022), pp. 1–15. DOI: 10.1109/TGRS.2021.3130903.

[65] F. Zhao and J. J. Mallorquí. "A Temporal Phase Coherence Estimation Algorithm and Its Application on DInSAR Pixel Selection". In: *IEEE Transactions on Geoscience and Remote Sensing* 57.11 (2019), pp. 8350–8361. DOI: 10.1109/TGRS.2019.2914626.

[66] E. Loria, A. O'Brien, and I. J. Gupta. "Detection and Separation of Coherent Reflections in GNSS-R Measurements Using CYGNSS Data". In: *IGARSS 2018–2018 IEEE International Geoscience and Remote Sensing Symposium*. IEEE, 2018, pp. 3995–3998.

[67] W. Li et al. "Altimetry over Sea Ice Using Coherent GNSS Reflections". In: *IGARSS 2018–2018 IEEE International Geoscience and Remote Sensing Symposium*. IEEE, 2018, pp. 8296–8298.

[68] M. Moreno et al. "Airborne Coherent GNSS Reflectometry and Zenith Total Delay Estimation over Coastal Waters". In: *Remote Sensing* 14.18 (2022), p. 4628. DOI: 10.3390/rs14184628.

[69] M. J. Unwin et al. "An Introduction to the HydroGNSS GNSS Reflectometry Remote Sensing Mission". In: *IEEE Journal of Selected Topics in Applied Earth Observations and Remote Sensing* 14 (2021), pp. 6987–6999. DOI: 10.1109/JSTARS.2021.3089550.

[70] K. T. Mulder and Irene Klugkist. "Bayesian Tests for Circular Uniformity". In: *Journal of Statistical Planning and Inference* 211 (2021), pp. 315–325. DOI: 10.1016/j.jspi.2020.07.005.

[71] Hamza Issa et al. "Airborne GNSS Reflectometry for Water Body Detection". In: *Remote Sensing* 14.1 (2021), p. 163. DOI: 10.3390/rs14010163.

[72] W. Liu et al. "Coastal Sea-Level Measurements Based on GNSS-R Phase Altimetry: A Case Study at the Onsala Space Observatory, Sweden". In: *IEEE Transactions on Geoscience and Remote Sensing* 55.10 (2017), pp. 5625–5636. DOI: 10.1109/TGRS.2017.2712192.

[73] Rene Garcia and Pierre Perron. "An Analysis of the Real Interest Rate under Regime Shifts". In: *The Review of Economics and Statistics* 78.1 (1996), pp. 111–125. DOI: 10.2307/2109851.

[74] E. S. Page. "Continuous Inspection Schemes". In: *Biometrika* 41.1/2 (1954), pp. 100–115. DOI: 10.1093/biomet/41.1-2.100.

[75] Jie Chen and Arjun K. Gupta. *Parametric Statistical Change Point Analysis: With Applications to Genetics, Medicine, and Finance*. Boston: Birkhäuser, 2014. ISBN: 0817648003. DOI: 10.1007/978-0-8176-4801-5.

[76] Charles Truong, Laurent Oudre, and Nicolas Vayatis. "Selective Review of Offline Change Point Detection Methods". In: *Signal Processing* 167 (2020), p. 107299. DOI: 10.1016/j.sigpro.2019.107299.

[77] Marc Lavielle. "Using Penalized Contrasts for the Change-Point Problem". In: *Signal Processing* 85.8 (2005), pp. 1501–1510. DOI: 10.1016/j.sigpro.2005.01.012.

[78] Hamed Heydari and Sayyed Fatemi. "Remote Sensing Change Detection: A Comparative Study of Spectral Distances". In: *Geocarto International* 38 (2023), pp. 1–21. DOI: 10.1080/10106049.2023.2248059.

[79] Jun Geng et al. "Online Change-Point Detection of Linear Regression Models". In: *IEEE Transactions on Signal Processing* 67.12 (2019), pp. 3316–3329. DOI: 10.1109/TSP.2019.2914893.

[80] Donald Holbert. "A Bayesian Analysis of a Switching Linear Model". In: *Journal of Econometrics* 19.1 (1982), pp. 77–87. DOI: 10.1016/0304-4076(82)90051-3.

[81] Jushan Bai. "Estimation of a Change Point in Multiple Regression Models". In: *The Review of Economics and Statistics* 79.4 (1997), pp. 551–563. DOI: 10.1162/003465397557132.

[82] J. H. Chin Choy and L. D. Broemeling. "Some Bayesian Inferences for a Changing Linear Model". In: *Technometrics* 22.1 (1980), pp. 71–78. DOI: 10.1080/00401706.1980.10486106.

[83] Jushan Bai, Jiangtao Duan, and Xu Han. "The Likelihood Ratio Test for Structural Changes in Factor Models". In: *Journal of Econometrics* 238.2 (2024), p. 105631. DOI: 10.1016/j.jeconom.2023.105631.

[84] Liangjun Su and Halbert White. "Testing Structural Change in Partially Linear Models". In: *Econometric Theory* 26.6 (2010), pp. 1761–1806. DOI: 10.1017/S0266466609990788.

[85] S. Phanyaem, Yupaporn Areepong, and Saowanit Sukparungsee. "Numerical Integration of Average Run Length of CUSUM Control Chart for ARMA Process". In: *International Journal of Applied Physics and Mathematics* 4 (2014), pp. 232–235. DOI: 10.7763/IJAPM.2014.V4.289.

[86] Diethelm Würtz, Yohan Chalabi, and Ladislav Luksan. "Parameter Estimation of ARMA Models with GARCH/APARCH Errors: An R and S-Plus Software Implementation". In: *Journal of Statistical Software* (2006).

[87] Jun-ichi Takeuchi and Kenji Yamanishi. "A Unifying Framework for Detecting Outliers and Change Points from Time Series". In: *IEEE Transactions on Knowledge and Data Engineering* 18.4 (2006), pp. 482–492. DOI: 10.1109/TKDE.2006.1599387.

[88] Audrey Giremus and Anne-Christine Escher. "A GLR Algorithm to Detect and Exclude up to Two Simultaneous Failures in a GPS/Galileo/IRS Case". In: *Proceedings of ION GNSS 2007*. United States, 2007, E6. URL: https://hal.science/hal-00183424.

[89] Hamza Issa et al. "Airborne GNSS Reflectometry for Water Body Detection". In: *Remote Sensing* 14.1 (2021), p. 163. DOI: 10.3390/rs14010163.

[90] Kanti V. Mardia and Peter E. Jupp. *Directional Statistics*. Wiley Series in Probability and Statistics. Chichester, UK: John Wiley & Sons, 1999. ISBN: 9780470316979.

[91] A. Lawrence Gould. "A Regression Technique for Angular Variates". In: *Biometrics* 25.4 (1969), pp. 683–700. DOI: 10.2307/2528567.

[92] Richard A. Johnson and Thomas E. Wehrly. "Some Angular-Linear Distributions and Related Regression Models". In: *Journal of the American Statistical Association* 73.363 (1978), pp. 602–606. DOI: 10.1080/01621459.1978.10480062.

[93] Nicholas I. Fisher and Alan J. Lee. "Regression Models for an Angular Response". In: *Biometrics* 48.3 (1992), pp. 665–677. DOI: 10.2307/2532334.

[94] Brett Presnell, Scott P. Morrison, and Ramon C. Littell. "Projected Multivariate Linear Models for Directional Data". In: *Journal of the American Statistical Association* 93.443 (1998), pp. 1068–1077. DOI: 10.1080/01621459.1998.10473765.

[95] Fangpo Wang and Alan E. Gelfand. "Directional Data Analysis under the General Projected Normal Distribution". In: *Statistical Methodology* 10.1 (2013), pp. 113–127. DOI: 10.1016/j.stamet.2012.07.005.

[96] Gabriel Núñez-Antonio, Eduardo Gutiérrez-Peña, and Gabriel Escarela. "A Bayesian Regression Model for Circular Data Based on the Projected Normal Distribution". In: *Statistical Modelling* 11.3 (2011), pp. 185–201. DOI: 10.1177/1471082X1001100301.

[97] Ali Esmaieeli Sikaroudi and Chiwoo Park. "A mixture of linear-linear regression models for a linear-circular regression". In: *Statistical Modelling* 21.3 (2021), pp. 220–243.

[98] Juan José Fernández-Durán and María Mercedes Gregorio-Domínguez. "Regression models for circular data based on nonnegative trigonometric sums". In: *Journal of Statistical Planning and Inference* 230 (2024), p. 106114.

[99] Georges Stienne et al. "A Multi-Temporal Multi-Sensor Circular Fusion Filter". In: *Information Fusion* 18 (2014), pp. 86–100. DOI: 10.1016/j.inffus.2013.05.012.

[100] Serge Reboul and Mohammed Benjelloun. "Joint segmentation of the wind speed and direction". In: *Signal Processing* 86.4 (2006), pp. 744–759.

[101] Marc Lavielle. "Optimal Segmentation of Random Processes". In: *IEEE Transactions on Signal Processing* 46.5 (1998), pp. 1365–1373. DOI: 10.1109/78.668798.

Résumé Étendu de la Thèse

La réflectométrie par système mondial de navigation par satellite (GNSS-R) s'impose comme une technique prometteuse de télédétection passive, exploitant les signaux d'opportunité émis par les constellations GNSS et réfléchis par la surface terrestre. Si les approches classiques se sont majoritairement concentrées sur l'amplitude et le retard du signal, cette thèse explore le potentiel encore sous-exploité de la phase porteuse, plus sensible aux variations fines de surface et offrant une meilleure résolution spatio-temporelle. L'objectif principal est de développer des méthodes robustes pour analyser, modéliser et détecter les changements dans la phase du signal réfléchi, en tenant compte de la nature circulaire de ces données. Pour cela, des tests statistiques adaptés, tels que Rayleigh, Watson, Kuiper et Rao, ont été étudiés et améliorés, et une approche bayésienne hors-ligne de détection multiple de points de changement (BCPD) a été proposée, fondée sur la distribution de Von Mises et l'estimation de fonctions de contraste intégrant les paramètres spectraux pertinents. Ce cadre méthodologique, validé à la fois sur des données synthétiques et réelles, permet une segmentation précise des séries de phase en intervalles homogènes et améliore la capacité à différencier les types de surface, même dans des environnements complexes. Ainsi, cette recherche contribue à enrichir les outils analytiques pour l'interprétation des signaux GNSS-R et ouvre de nouvelles perspectives pour la surveillance environnementale et l'inférence géophysique à haute résolution.

1 Utilisation de la phase porteuse dans le traitement du signal GNSS-Reflectometry

1.1 Principes Fondamentaux de la GNSS-Reflectométrie (GNSS-R)

La GNSS-Reflectométrie (GNSS-R) fonctionne comme un système radar bistatique, où l'émetteur (satellite GNSS) et le récepteur sont spatialement séparés par une distance comparable à celle entre le récepteur et la surface cible

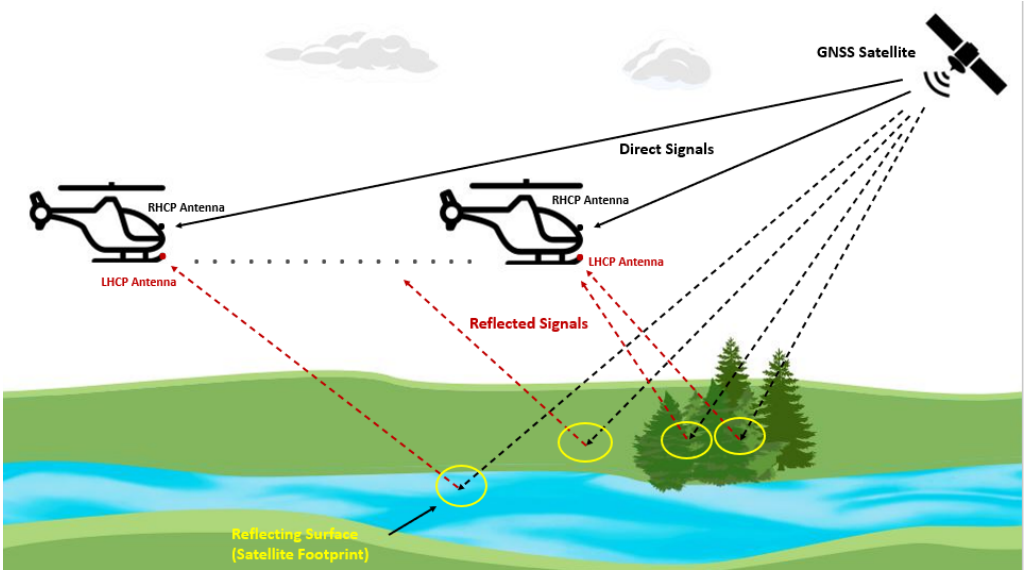

FIGURE R.1: Concept de cohérence de phase en GNSS-R.

[1]. Elle exploite les signaux des systèmes GNSS (GPS, GLONASS, Galileo, BeiDou) comme signaux d'opportunité, permettant une couverture globale et une flexibilité d'acquisition (embarqué, aérien ou station au sol). Initialement proposée par Martín-Neira en 1993 [2] pour l'altimétrie océanique, la GNSS-R a depuis été appliquée à de multiples domaines : estimation de l'état de la mer, mesure de la vitesse du vent, détection de l'humidité du sol, topographie des surfaces, observation de la cryosphère et détermination du contenu électronique ionosphérique.

Au niveau du récepteur, le champ électromagnétique est la superposition des signaux directs et réfléchis provenant de plusieurs satellites. Ces contributions peuvent être séparées grâce à deux antennes distinctes : l'une pointée vers les satellites pour capter les signaux directs, et l'autre orientée vers la surface terrestre pour collecter les signaux réfléchis.

1.2 Intérêt de la Phase Porteuse en GNSS-R

La GNSS-R exploite plusieurs observables : l'amplitude (SNR), le retard de code et la phase porteuse. La phase porteuse présente un avantage décisif grâce à sa courte longueur d'onde (environ 19 cm pour le signal L1 GPS), offrant une résolution spatio-temporelle centimétrique. Elle est particulièrement sensible aux variations fines de la hauteur, de la rugosité et des propriétés diélectriques de la surface [9, 10]. Cela la rend adaptée à la détection de changements subtils dans des environnements dynamiques.

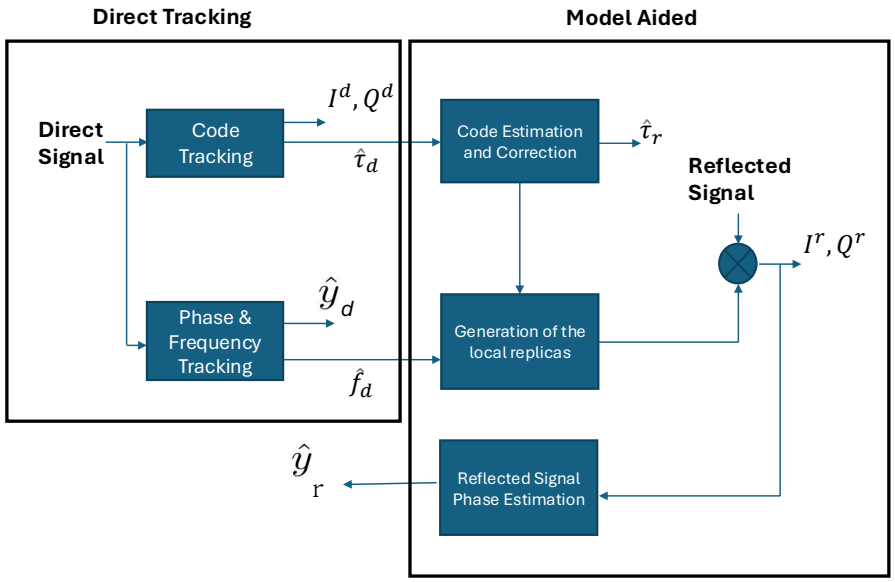

FIGURE R.2: Schéma de traitement de la phase réfléchie GNSS

1.2.1 Comparaison avec l'Amplitude et le SNR

L'amplitude ou le SNR fournit des informations sur la rugosité et l'humidité du sol, et reste robuste dans les environnements fortement diffusifs. Toutefois, ces mesures sont limitées par leur résolution (décimétrique) et leur sensibilité aux erreurs de traitement, notamment lorsqu'une décomposition en ondelettes est utilisée pour le lissage [15]. Le Tableau R.1 résume les compromis entre ces observables.

TABLE R.1: Comparaison des observables GNSS-R

Propriété	Phase porteuse	SNR / Amplitude
Résolution	Élevée (cm)	Moyenne (dm)
Sensibilité à l'humidité	Élevée	Moyenne
Détection de la rugosité	Élevée	Élevée
Ambiguïté de phase	Présente	Aucune
Sensibilité au bruit	Moyenne	Élevée
Complexité	Élevée	Faible
Sensibilité de l'antenne	Invariante au gain	Dépendante du gain

1.3 Mesure de la Phase Réfléchie et Modélisation

La phase porteuse réfléchie est estimée via une boucle ouverte (Open Loop) utilisant comme référence les paramètres estimés du signal direct ($\hat{f}_d$ et $\hat{\tau}_d$). Le schéma de traitement est illustré en Figure R.2.

Le modèle de la phase mesurée est donné par :

$$y_i = \arctan\left(\frac{Q_i}{I_i}\right) = \lfloor \bar{y}_i + \xi_i \rfloor \mod 2\pi$$

où ξ_i est un bruit distribué selon une loi de Von Mises.

1.4 Distribution du Bruit de Phase : Loi de Von Mises

La distribution de Von Mises est utilisée pour modéliser le bruit de phase circulaire. Sa fonction de densité est :

$$f(\theta; \mu, \kappa) = \frac{1}{2\pi I_0(\kappa)} \exp\left(\kappa \cos(\theta - \mu)\right),$$

où κ contrôle la concentration autour de la direction moyenne μ.

1.5 Campagne Aéroportée GNSS-R

Une campagne GNSS-R a été réalisée en octobre 2020 dans le nord de la France [71], avec une altitude moyenne de 315 m et une vitesse de 95 km/h, permettant une résolution spatiale d'environ 0,53 m par point de réflexion (Figure 3.6).

2 Détection de points de changement : Revue de la littérature

2.1 Introduction à la Détection de Points de Changement

La détection de points de changement (*Change Point Detection*, CPD) consiste à identifier les instants où les propriétés statistiques d'une série temporelle subissent une variation significative. Ces changements peuvent concerner la moyenne, la variance, la distribution ou encore des structures d'ordre supérieur des données. Cette tâche est cruciale dans de nombreux domaines tels que le traitement du signal, la climatologie, la finance, la production industrielle et la GNSS-réflectométrie, car elle permet de caractériser l'évolution et les dynamiques sous-jacentes des systèmes étudiés.

2.2 Taxonomie des Méthodes de CPD

Les approches de CPD peuvent être organisées en deux grandes catégories : la détection de **points de changement multiples** (*Multiple Change Point Detection*, MCPD) et la détection de **point de changement unique** (*Single Change Point Detection*, SCPD). Cette classification est illustrée dans la Figure R.3, qui met en évidence les principaux aspects méthodologiques de chaque catégorie.

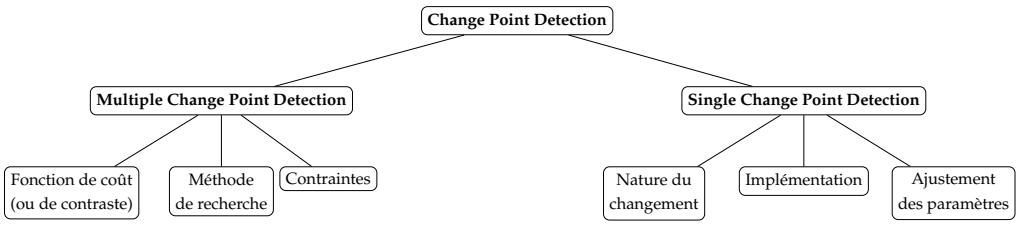

FIGURE R.3: Taxonomie structurée de la détection de points de changement selon les aspects méthodologiques

2.3 Composantes Méthodologiques des Deux Catégories

2.3.1 Détection de Points de Changement Multiples (MCPD)

Dans le cas des MCPD, trois éléments principaux structurent la méthode :

- **Fonction de coût ou de contraste** : elle mesure l'adéquation entre les segments détectés et les propriétés statistiques attendues.
- **Méthode de recherche** : elle définit la stratégie pour localiser plusieurs points de changement (ex. recherche séquentielle, dynamique, ou heuristique).
- **Contraintes** : elles imposent des conditions sur le nombre minimal de points, la taille des segments ou la régularité temporelle.

2.3.2 Détection de Point de Changement Unique (SCPD)

Pour les SCPD, l'accent est mis sur :

- **La nature du changement** : moyenne, variance, distribution, ou structure plus complexe.
- **L'implémentation** : choix des algorithmes et optimisation des performances computationnelles.
- **L'ajustement des paramètres** : réglages nécessaires pour adapter la méthode aux données spécifiques (seuils, pénalités, etc.).

2.4 Intérêt de la Taxonomie

Cette taxonomie fournit une vue d'ensemble des méthodes de CPD et facilite leur sélection selon la nature des données et les objectifs analytiques. Elle permet également d'identifier les composants clés sur lesquels reposent la sensibilité et la robustesse des approches existantes.

3 Test Statistique Circulaire pour la Détection de Points de Changement

Les données circulaires apparaissent dans de nombreuses applications scientifiques et techniques, notamment lorsqu'elles sont de nature directionnelle ou périodique, comme les mesures angulaires, les heures de la journée ou les phases dans le traitement du signal. Contrairement aux variables linéaires, les variables circulaires se referment sur un intervalle fixe, généralement 2π radians ou 360°, ce qui nécessite l'utilisation de techniques statistiques spécifiques respectant cette topologie. Les méthodes classiques, conçues pour des données linéaires, sont souvent inadaptées pour capturer les caractéristiques essentielles de ce type de données, d'où la nécessité de tests spécialisés.

3.1 Tests Statistiques dans le Domaine Circulaire

Un des problèmes fondamentaux en statistique circulaire consiste à tester l'uniformité, c'est-à-dire à déterminer si un ensemble de données angulaires est réparti uniformément ou présente une direction préférentielle. Le test de Rayleigh est l'un des plus utilisés : il évalue la magnitude du vecteur résultant moyen et la compare à celle attendue sous hypothèse d'uniformité. Une valeur élevée indique une déviation par rapport à une répartition uniforme. Ce type de test est essentiel pour identifier des structures directionnelles significatives dans divers contextes.

3.2 Application sur Données Réelles

Les données expérimentales utilisées ont été enregistrées lors d'une campagne aéroportée dans le nord de la France. Le système GNSS-R embarqué, composé d'une antenne orientée vers le haut (RHCP), d'une antenne orientée vers le bas (LHCP) et d'un système d'acquisition synchrone, a permis de collecter les signaux GPS L1 à une fréquence d'échantillonnage élevée. Trois satellites (PRN 5, 7 et 30) ont été sélectionnés pour leur élévation importante,

garantissant une bonne fiabilité des paramètres de réflexion. Les données ont été segmentées à l'aide de l'approche de détection de changement basée sur le test de Rayleigh, avec des paramètres adaptés à la cohérence de phase mesurée. La Figure R.4 illustre les traces de réflexion sur environ 2 km, où différents niveaux de cohérence de phase ont été détectés, en particulier pour les surfaces d'eau qui apparaissent comme des zones lisses et cohérentes. Les champs et forêts présentent des variations plus complexes et une sensibilité plus faible pour certains satellites.

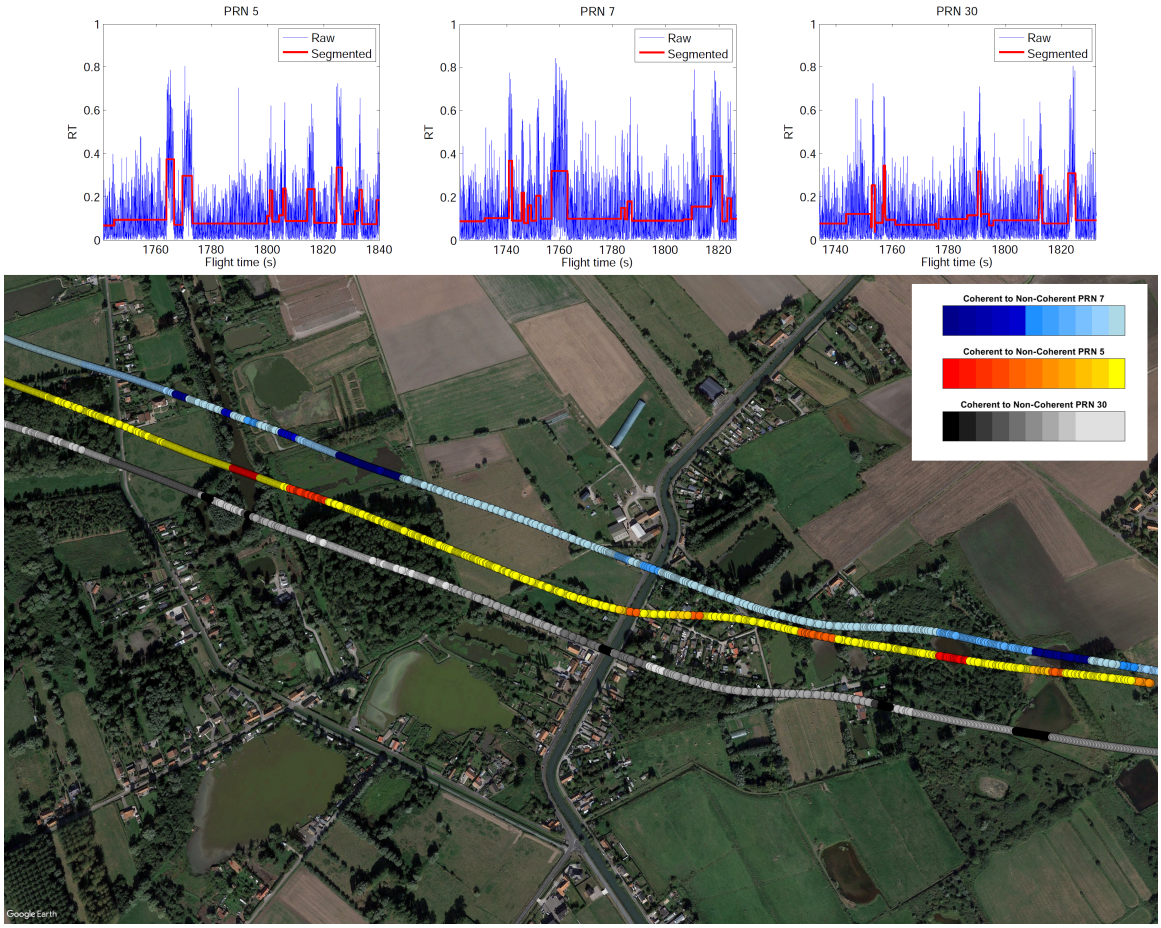

FIGURE R.4: Traces des satellites GPS PRN 5, 7 et 30 le long de la trajectoire de vol et niveaux de cohérence de phase segmentés par l'approche Rayleigh (50.8763°, 1.9548°).

3.3 Conclusion et Perspectives

Cette étude met en évidence l'efficacité des tests d'uniformité circulaire, et notamment du test de Rayleigh, pour la détection de la cohérence de phase dans des données de télédétection GNSS-R. Cette détection permet non seulement de sélectionner des données fiables pour diverses applications, mais

également de fournir des informations directes sur les caractéristiques des surfaces observées. L'approche développée, fondée sur la segmentation des sorties du test de Rayleigh et sensible aux variations de moyenne et de variance, a démontré sa capacité à localiser précisément les changements de cohérence de phase, en particulier pour les petites étendues d'eau. Des perspectives incluent l'intégration d'autres fréquences GNSS et l'exploitation des informations de réflectivité pour améliorer la discrimination des types de surfaces, notamment en zones forestières et agricoles.

4 Détection Bayésienne Hors-Ligne des Changements

Ce chapitre présente une méthode bayésienne de détection de points de changement (BCPD) appliquée à la phase des signaux GNSS réfléchis. L'objectif est de détecter les variations de cohérence liées aux changements de surface en exploitant la composante de phase du signal réfléchi.

4.1 Modélisation de la Phase

La phase du signal réfléchi est modélisée comme une combinaison pondérée de plusieurs réflexions caractérisées par leurs amplitudes, déphasages et décalages Doppler. Les composantes en phase (I_i) et en quadrature (Q_i) sont utilisées pour calculer la phase observée :

$$y_i = \arctan\left(\frac{Q_i}{I_i}\right) \mod 2\pi$$

Les réflexions multiples sont prises en compte via une distribution de Von Mises, dont le paramètre de concentration κ traduit le niveau de cohérence.

4.2 Principe de la Méthode BCPD

La détection s'appuie sur une approche bayésienne hors-ligne, où la série de phases $\underline{y}$ est supposée stationnaire par segments. Les points de changement $\underline{r}$ et les paramètres associés $\underline{\theta}$ sont estimés par maximisation a posteriori :

$$(\hat{\underline{r}}, \hat{\underline{\theta}}) = \arg\max_{(\underline{r},\underline{\theta})} h(\underline{y} \mid \underline{r}, \underline{\theta})\, f(\underline{\theta})\, p(\underline{r})$$

Une fonction de contraste pénalisée est ensuite minimisée pour localiser les changements.

4.3 Estimation des Paramètres

Les paramètres $\{\hat{\alpha}_{u,k}, \hat{\phi}_{u,k}, \hat{A}_{u,k}\}$ et $\hat{\kappa}_k$ sont estimés pour chaque segment. Le spectre Doppler excédentaire permet d'identifier les pics de réflexion et d'en déduire les amplitudes et phases correspondantes.

4.4 Résultats sur Données Synthétiques

La méthode a été testée sur un signal GNSS synthétique de 6 secondes comportant trois segments : deux cohérents et un non-cohérent. Les résultats montrent que la BCPD détecte précisément les changements aux instants $t = 2$ et $t = 4$ secondes, avec de meilleures performances que la distance euclidienne classique.

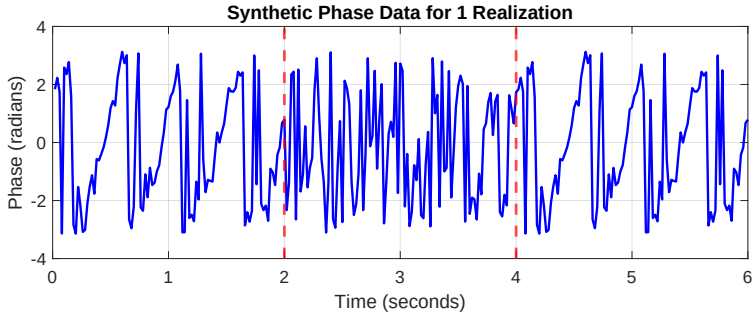

FIGURE R.5: Résultat de détection des changements sur des données synthétiques.

4.5 Résultats sur Données Réelles GNSS-R

Des données réelles acquises en vol en France ont été analysées. La méthode a permis de détecter des transitions nettes entre des surfaces lisses (lac) et rugueuses (terre), comme illustré sur la Figure R.6. Les paramètres estimés montrent une concentration $\hat{\kappa}$ plus élevée pour les surfaces cohérentes et plus faible pour les surfaces rugueuses.

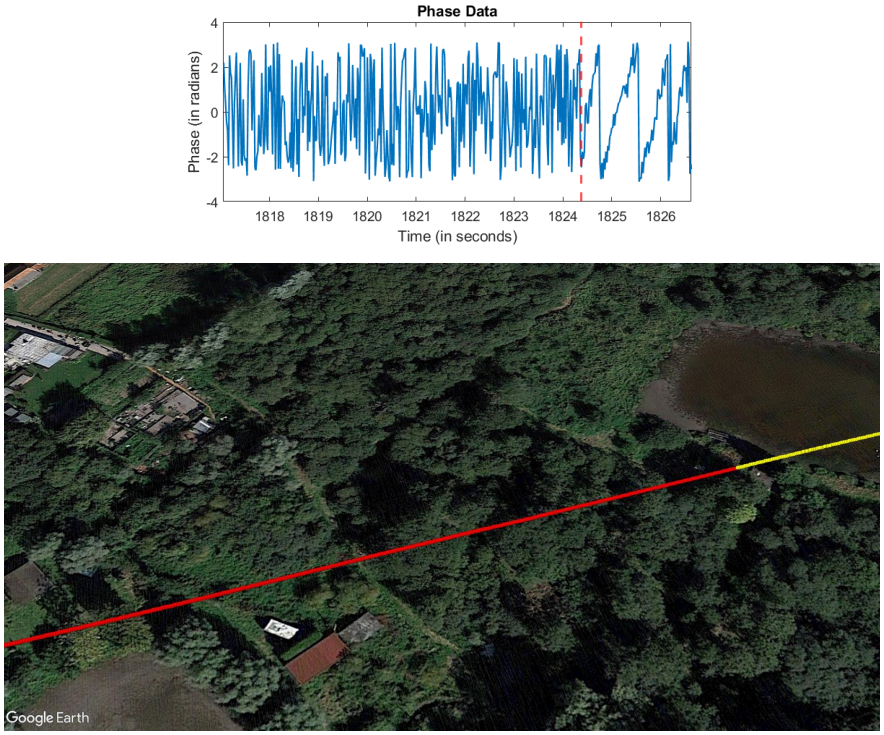

FIGURE R.6: Données réelles GNSS-R : détection d'un changement entre une surface lisse (lac) et une surface rugueuse (terre).

4.6 Conclusion

La méthode BCPD proposée permet une détection robuste et précise des points de changement dans la phase des signaux GNSS réfléchis. Elle surpasse les approches classiques, notamment en environnement bruité, et présente un fort potentiel pour des applications de télédétection environnementale et de suivi géophysique.

Abstract

Global Navigation Satellite System Reflectometry (GNSS-R) has emerged as a promising passive remote sensing technique, capable of providing high-resolution information on Earth's surfaces. While most GNSS-R applications have focused on amplitude and delay observables, the carrier phase of reflected signals remains largely underexploited due to its circular nature and processing challenges. This thesis investigates the potential of carrier-phase measurements for detecting surface changes, emphasizing phase coherence variations as a sensitive indicator of environmental and geophysical dynamics. For this purpose, classical and modern change point detection (CPD) methods are reviewed and a rigorous analytical framework is developed to address the unique statistical characteristics of phase data. Circular uniformity tests are explored as indicators of coherence levels in such data. In particular, CPD based on the Rayleigh Test is applied for the detection and localization of changes in phase noise moments. A novel offline Bayesian Change-Point Detection (BCPD) methodology is also adapted to circular data by modeling phase noise with the Von Mises distribution and incorporating spectral features related to excess Doppler shifts. The BCPD framework enables principled segmentation of the data into statistically homogeneous intervals, balancing sensitivity and robustness. The proposed approaches are first validated on synthetic datasets, demonstrating, under controlled conditions, their ability to accurately detect subtle changes. Subsequently, real GNSS-R measurements are analyzed, showing that the proposed methods can successfully identify phase transitions corresponding to changes in reflecting surface types. These results illustrate the practical applicability of carrier-phase-based detection and its superiority in capturing fine-grained surface changes. This work bridges the methodological gap between GNSS-R signal processing, directional statistics, and Bayesian inference, establishing a unified framework for high-resolution, phase-based remote sensing. The findings provide both theoretical and practical contributions, paving the way for advanced environmental monitoring and geophysical applications using GNSS-R.

Keywords: GNSS Signal Processing; Phase Coherence, Remote Sensing, Change Detection, GNSS-Reflectometry, Airborne Observation

Résumé

La Réflectométrie par Système Global de Navigation par Satellite (GNSS-R) est une technique prometteuse de télédétection passive, capable de fournir des informations à haute résolution sur la surface de la Terre. Alors que la plupart des applications GNSS-R se sont concentrées sur les observables d'amplitude et de délai, la phase de la porteuse des signaux réfléchis reste largement sous-exploitée en raison de sa nature circulaire et des défis liés à son traitement. Cette thèse étudie le potentiel des mesures de phase GNSS-R pour la différenciation de types de surface de réflexion, en mettant l'accent sur les variations de cohérence de phase comme indicateur des dynamiques environnementales et géophysiques. Pour cela, les méthodes classiques et modernes de détection de ruptures sont passées en revue et un cadre analytique rigoureux est développé pour traiter les caractéristiques statistiques uniques des données de phase. Les tests d'uniformité circulaires sont examinés comme indicateurs de cohérence dans ces données. En particulier, un détecteur de ruptures basé sur le test de Rayleigh est appliqué pour détecter et localiser les ruptures dans les moments statistiques du bruit de phase. Une nouvelle méthodologie de détection bayésienne de ruptures (BCPD) hors ligne est proposée en modélisant le bruit de phase par la distribution de Von Mises et en utilisant des caractéristiques spectrales liées au signal d'excès Doppler. Le cadre BCPD permet une segmentation rigoureuse des données en intervalles statistiquement homogènes, équilibrant sensibilité et robustesse. Les approches proposées sont d'abord validées sur données synthétiques, démontrant dans des conditions contrôlées leur capacité à détecter avec précision des ruptures subtiles. Par la suite, les méthodes proposées sont confrontées à des mesures GNSS-R réelles, démontrant leur capacité à identifier avec succès les transitions de phase correspondant à l'observation de différentes surfaces réfléchissantes. Ces résultats illustrent l'applicabilité pratique de la détection basée sur la phase des signaux GNSS-R et sa supériorité pour différencier finement les surfaces de réflexion. Ce travail comble le fossé méthodologique entre le traitement du signal GNSS-R, les statistiques circulaires et l'inférence bayésienne, établissant un cadre unifié pour une télédétection à haute résolution basée sur la phase. Les résultats apportent des contributions théoriques et pratiques, ouvrant la voie à des applications avancées de surveillance environnementale et géophysique utilisant le GNSS-R.

Mots-clés : traitement du signal GNSS ; cohérence de phase ; télédétection ; détection de ruptures ; réflectométrie GNSS ; observation aéroportée